

**ADVANCES IN NON-PLATINUM CATALYSIS FOR THE HYDROGEN OXIDATION
AND HYDROGEN EVOLUTION REACTIONS**

by

LAURA KATIE ALLERSTON

**A thesis submitted to the University of Birmingham for the degree of DOCTOR
OF PHILOSOPHY**

Centre for Fuel Cells and Their Fuels

School of Chemical Engineering

University of Birmingham

September 2019

UNIVERSITY OF
BIRMINGHAM

University of Birmingham Research Archive

e-theses repository

This unpublished thesis/dissertation is copyright of the author and/or third parties. The intellectual property rights of the author or third parties in respect of this work are as defined by The Copyright Designs and Patents Act 1988 or as modified by any successor legislation.

Any use made of information contained in this thesis/dissertation must be in accordance with that legislation and must be properly acknowledged. Further distribution or reproduction in any format is prohibited without the permission of the copyright holder.

Abstract

The development of non-Pt hydrogen oxidation reaction catalysts for hydrogen-fuelled polymer electrolyte fuel cells allows for an overall reduction in electrode Pt content and can reduce the industry reliance on this catalyst. Herein, a novel ternary alloy catalyst supported on carbon, PdIrAu/C, has been synthesised, characterised, and compared to the binary PdIr/C catalyst to show how the addition of Au improves the stability of the catalyst. Transmission electron microscopy was utilised to analyse electrode structure as a function of the synthesis method, showing the optimum annealing temperature, of those tested, to be 400 °C, while inductively-coupled plasma mass spectrometry and *in-situ* testing provided analysis of the degradation of the two catalysts, confirming the PdIrAu/C catalyst is more stable when assessed by accelerated stress tests at potentials similar to those at a fuel cell anode than PdIr/C. Comparison of the catalysts after 1000 ASTs showed PdIrAu provided an overall better polarisation curve and a significant 36% higher current density at 0.6 V compared with PdIr.

Non-Pt hydrogen evolution catalysts for electrolyzers are discussed and method development for a new synthesis method utilising a lower temperature and therefore a safer reaction than the common production techniques is presented. The resulting Ni₂P catalyst imaging is presented showing the synthesis method was successful. Robust test methods were created and assessed throughout this body of work and a thorough example of one method is presented, showing the production of MEAs for experimental purposes and concluding, through use of X-ray CT and *ex-situ* testing, the addition of ionomer to commercial MEAs reduces the surface area and performance and therefore is not required.

Acknowledgements

Thanks, must begin with my supervisor Dr. Neil Rees who has been there from interview to the end, always willing for a helpful chat and providing guidance all the way. Thanks also to my secondary supervisor Prof. Dan Brett for your advice and allowing me to perform so many experiments in your labs and making me feel like one of your group, I will be forever indebted to you for introducing me to James.

Thank you to Dr. David Hodgson, Chris Gibbs and Dr. Simon Jones at Amalyst Ltd. And PV3 for their funding, guidance and support throughout.

At the Nanoscale and microscale research centre (NMRC), University of Nottingham I would like to thank Dr. Karen Alvey, Dr. Michael Fay, Dr. Emily Smith and particularly Dr. Craig Stoppiello for going above and beyond with imaging guidance. At the University of Birmingham, I would like to thank Prof. Liam Grover, and Dr. Richard Williams and Dr. Erik Hughes for their assistance with the XRF technique. Great thanks also to Jackie Deans for being so lovely with her training in XRF and XRD techniques.

To everyone in the Fuel Cells CDT, thanks for being there through the many, many highs and lows. At the start with Aimee, James, Lois, Geoff, Scott, Ahmad and Hal; there were an unbelievable amount of laughs that first year. With the fantastic additions of Pete, Alan, Ollie, Abby and Liam; you all got me through so much. And then to Amrit, who took me under his wing from the start and still won't let go, thanks for everything.

Thanks to my family and home friends who have heard many a complaint. Most importantly to my parents, to whom this entire thing is dedicated. June and Jeff, I firmly believe you are the best people in the world, thank you for the world you have given me, I will never be able to tell you enough how much you mean to me.

James, thanks for the proofreads, the little comments and your unwavering support. Needless to say, I would not have stuck this out without you. Thanks for pulling me out of the rabbit hole and bringing me to happiness.

As Lewis Carroll said: "Begin at the beginning, and go on until you come to the end; then stop." Thank god it is finally the end!

Abbreviations and Symbols

AAEMFC	Alkaline anion exchange membrane fuel cell
A_c ($\text{cm}^2 \text{mg}^{-1}$)	Catalyst specific area
AEC	Alkaline electrolyser cell
AFC	Alkaline fuel cell
AFM	Atomic Force Microscopy
α_{Ox}	Oxidation transfer coefficient
α_{Rd}	Reduction transfer coefficient
AST	Accelerated stress test
BET	Brunauer-Emmet-Teller
BPP	Bipolar plate
C_B (mol cm^{-3})	Bulk concentration
CL	Catalyst layer
CNT	Carbon nanotubes
C_{Ox} (mol cm^{-2})	Surface concentration of oxidised species
C_{Rd} (mol cm^{-2})	Surface concentration of reduced species
CT	Computed tomography
CV	Cyclic voltammogram

D (cm ² s ⁻¹)	Diffusion coefficient
DAFC	Direct alcohol fuel cell
DEFC	Direct ethanol fuel cell
δ (cm)	Diffusion distance
ΔG_H	Hydrogen bond strength
DFAFC	Direct formic acid fuel cell
DFT	Density functional theory
DMFC	Direct methanol fuel cell
DoE	Department of energy
D ₀ (kJ mol ⁻¹)	Bond strength
E (V)	Thermodynamic voltage
EC	Electrolyser cell
E _c (kJ mol ⁻¹)	Activation energy
E _c (V)	Cathodic potential
ECSA	Electrochemical surface area
EDX	Energy dispersive X-Ray spectroscopy
EIS	Electrochemical impedance spectroscopy
EOR	Ethanol oxidation reaction

E_r (V)	Equilibrium potential
$E_{r.c}$ (V)	Cathodic potential at equilibrium
$E_{reference}$ (V)	Reference electrode potential
$E_{working}$ (V)	Working electrode potential
E_0 (V)	Thermodynamic voltage at standard conditions
F (C/mol)	Faraday constant
FAOR	Formic acid reduction reaction
FC	Fuel cell
fcc	Face centred cubic lattice
FCEV	Fuel cell electric vehicle
FE	Field emission
G (kJ mol ⁻¹)	Gibbs free energy
Γ ($\mu\text{C cm}^{-2}$)	Electrical charge associated with monolayer of adsorbed hydrogen on catalyst surface
γ	Pressure dependency coefficient
GC	Glassy carbon
G_{ch} (kJ mol ⁻¹)	Chemical component of Gibbs free energy
GDE	Gas diffusion electrode

GDL	Gas diffusion layer
H (kJ mol ⁻¹)	Enthalpy
h (J s)	Planks constant
HAADF	High angle annular dark field detector
HDPE	High density polyethylene
HER	Hydrogen evolution reaction
ΔH_{HHV} (J)	Enthalpy calculated using higher heating value of hydrogen
ΔH_{LHV} (J)	Enthalpy calculated using lower heating value of hydrogen
HOR	Hydrogen oxidation reaction
HT-PEM	High temperature polymer electrolyte membrane
HWFET	Highway fuel economy test
i (A cm ⁻²)	Current density
ICE	Internal combustion engine
ICP-AES	Inductively coupled plasma atomic emission spectrometry
ICP-MS	Inductively coupled plasma mass spectrometry
I _L (A)	Limiting current
IPA	Isopropyl alcohol
ISO	International organisation for Standardisation

IUPAC	International Union of Pure and Applied Chemistry
i_0 (A cm ⁻²)	Exchange current density
$i_{0,c}$ (A cm ⁻²)	Exchange current density at the cathode
i_0^{ref} (A cm ⁻²)	Reference exchange current density
j (mol s ⁻¹ cm ⁻²)	Flux of reactant per unit area
k (s ⁻¹)	Rate constant
k_B (J K ⁻¹)	Boltzmann's constant
k_b (s ⁻¹)	Rate constant of backward reaction
k_f (s ⁻¹)	Rate constant of forward reaction
$k_{0,b}$	Backward rate constant at equilibrium
$k_{0,f}$	Forward rate constant at equilibrium
L (mg)	Mass of catalyst
L_c (mg cm ⁻²)	Catalyst loading
LSV	Linear sweep voltammetry
MCFC	Molten carbonate fuel cell
MEA	Membrane electrode assembly
MEM	Membrane
MPL	Mesoporous layer

MWNTs	Multiwalled carbon nanotubes
n	Number of electrons
NEDC	New European driving cycle
nF (C mol ⁻¹)	Charge transferred
NP	Nanoparticle
NW	Nanowires
OCV (V)	Open circuit voltage
ORR	Oxygen reduction reaction
P (kPa)	Pressure
PAFC	Phosphoric acid fuel cell
PEMEC	Polymer electrolyte membrane electrolyser cell
PEMFC	Polymer electrolyte membrane fuel cell
PGM	Platinum group metals
ppb	Parts per billion
$P_{P^{ref}}$ (kPa)	Reference partial pressure
ppt	Parts per trillion
P_r (kPa)	Reactant partial pressure
PTFE	Polytetrafluoroethylene

PTL	Porous transport layer
PVA	Polyvinyl alcohol
Q_H (C m ⁻³)	Charge density
R (J mol ⁻¹ K ⁻¹)	Gas constant
R (Ω)	Resistance
RDE	Rotating disk electrode
RDS	Rate determining step
RGO	Reduced graphene oxide
RHE	Reference hydrogen electrode
RH %	Relative humidity
S (J K ⁻¹)	Entropy
SA	Surface area
SEM	Scanning electron microscopy
SHE	Standard hydrogen electrode
SOEC	Solid oxide electrolyser cell
SOFC	Solid oxide fuel cell
SOP	Standard operating procedure
STEM	Scanning transmission electron microscopy

STP	Standard temperature and pressure
SXRPD	Synchrotron X-Ray powder diffraction
T (K)	Temperature
TEM	Transmission electron microscopy
TGA	Thermogravimetric analysis
TOP	Tri-n-octylphosphine
TPB	Triple phase boundary
T_r (K)	Reference temperature
UoB	University of Birmingham
ν	Times rate determining steps must occur for one overall reaction
V_{conc} (V)	Voltage loss due to concentration
XPS	X-ray photoelectron spectroscopy
XRD	X-Ray diffraction
XRF	X-Ray fluorescence

Table of Contents

List of Figures	xvii
List of Tables	xxiv
1. INTRODUCTION	1
1.1. Fuel Cells	1
1.2. Types and background.....	2
1.2.1. Phosphoric Acid Fuel Cells (PAFCs)	3
1.2.2. Alkaline Fuel Cells (AFCs) and Alkaline Anion Exchange Membrane Fuel Cells (AAEMFCs).....	4
1.2.3. Molten Carbonate Fuel Cells (MCFCs)	6
1.2.4. Solid Oxide Fuel Cells (SOFCs).....	6
1.3. Polymer Electrolyte Membrane Fuel Cells	8
1.3.1. Types of PEM	8
1.3.2. PEM Components	11
1.3.3. Catalyst Layer	18
1.3.4. Oxygen Reduction Reaction (ORR)	23
1.3.5. Hydrogen Oxidation Reaction (HOR).....	25
1.3.6. Thermodynamics	26
1.3.7. Kinetics	27
1.3.8. Exchange Current Density	30
1.3.9. Activation Overpotential	32

1.3.10. Polarisation Curve.....	32
1.3.11. Potential Loses	33
1.3.12. Pressure, Fuel and Temperature Effects	36
1.4. Commercialisation barriers.....	37
2. LITERATURE REVIEW ON HOR CATALYST	40
2.1. Motivation.....	40
2.2. Palladium catalysts	42
2.2.1. Palladium alloy catalysts	43
2.2.2. Summary of Review	52
2.2.3. Palladium Iridium Catalyst.....	52
2.3. Palladium Iridium Gold Catalyst	53
2.4. Synthesis method of PdIrAu/C	54
3. METHODOLOGY	55
3.1. Materials.....	55
3.2. Electrochemical Techniques	55
3.2.1. <i>Ex-situ</i> set up	56
3.2.2. Cyclic Voltammetry	63
3.2.3. Electrochemical Surface Area.....	64
3.2.4. Degradation	66
3.3. Imaging	67
3.3.1. Scanning Electron Microscopy	68

3.3.2. Transmission Electron Microscopy	68
3.3.3. Energy Dispersive X-ray spectroscopy	70
3.3.4. X-Ray Fluorescence	71
3.3.5. X-Ray Computational Tomography	71
3.3.6. Atomic Force Microscopy	72
3.4. Characterisation	73
3.4.1. X-ray Diffraction	73
3.4.2. Inductively Coupled Plasma-Mass Spectrometry	73
3.4.3. Thermogravimetric Analysis	74
3.5. <i>In-situ</i> Testing	75
3.5.1. Properties of MEA components	75
3.5.2. Hot Pressing	78
3.5.3. Single Cell Testing	80
4. TEST METHOD VALIDATION OF NAFION IONOMER ADDITION TO MEA	89
4.1. Motivation	89
4.1.1. Preparation	91
4.1.2. SEM and Line EDX	91
4.1.3. X-ray CT	93
4.1.4. <i>In-situ</i> testing	99
4.2. Conclusions	100

5. SYNTHESIS, CHARACTERISATION AND TESTING OF PALLADIUM ALLOY CATALYST	102
5.1. Synthesis of PdIrAu/C catalyst	102
5.2. TGA	103
5.3. TEM	104
5.4. EDX including mapping	108
5.5. XRF	109
5.6. XRD	114
5.7. <i>Ex-situ</i> degradation	115
5.8. ICP-MS.....	121
5.9. <i>In-situ</i> degradation	124
5.10. Discussion.....	129
5.11. Conclusions and Future Work	129
6. ELECTROLYSER INTRODUCTION WITH SYNTHESIS OF Ni ₂ P CATALYST	131
6.1. Introduction	131
6.1.1. Alkaline electrolysis cells (AECs)	133
6.1.2. Solid Oxide Electrolysis Cells (SOECs)	134
6.2. Polymer electrolyte membrane electrolysis cells (PEMECs)	135
6.2.1. Components.....	136
6.2.2. OER	138
6.2.3. HER	138

6.3. Common Catalysts.....	139
6.4. Alternative catalysts	140
6.5. Nickel Phosphide Catalyst.....	141
6.6. Motivation.....	143
6.7. Standard method.....	143
6.8. Method development of Ni ₂ P Synthesis	144
6.9. TEM and HAADF	146
6.10. EDX mapping	150
6.11. ICP-MS.....	151
6.12. XRD.....	152
6.13. AFM.....	153
6.14. Conclusions and future work	156
7. CONCLUSIONS AND FUTURE WORK	157
8. References	168

List of Figures

Figure 1 - Diagram showing the reactions and flows within a PEMFC	2
Figure 2 - Illustration of the component parts which make up the fuel cell	12
Figure 3 - Different flow patterns for fuel dispersion through the bipolar plate. The pattern is machined directly onto the plate (a) straight, (b) interdigitated, (c) serpentine and (d) spiral	13
Figure 4 - Nafion structure showing a fluorinated carbon backbone with HSO_3 attached allowing ionic transfer	15
Figure 5 - Different structures of bimetallic catalysts a) mixed alloy b) random alloy c) subcluster with two interfaces d) subcluster with three interfaces e) subcluster with small amount of A-B bonding f) core-shell nanoparticle g) multishell core-shell nanoparticle h) multiple small core materials coated in single shell material i) movable core in hollow shell material	20
Figure 6 - Trends in oxygen reduction activity plotted as a function of the oxygen binding energy	25
Figure 7 - Resulting polarisation curve due to losses from theoretical polarisation curve	34
Figure 8 - Transport applications which FCs could be utilised for broken down by energy usage globally in 2015. Total consumption was 110 TJ	39
Figure 9 - Monthly values of platinum, palladium and iridium over the last ten years	41
Figure 10 - Percentage breakdown of the demand markets for Pt in 2019	41
Figure 11 - Illustration of how the Pd-O interaction alters with varying d band centre where as ϵ_d is shifted up toward the Fermi level ($\epsilon_F=0$) the width of the d bands is	

decreased to allow the number of electrons in the bands to stay constant. Above ϵ_F the antibonding states are emptied, and the bond becomes stronger	44
Figure 12 - Illustration of <i>ex-situ</i> three-electrode cell set up.	57
Figure 13 - CV indicating the different reactions occurring at a polycrystalline Pt electrode with cycling potential between 0.05 V and 1.6 V at a scan rate of 0.1 V s ⁻¹	64
Figure 14 - Recorded potentials at the cathode (a) and anode (b) of the fuel cell at start up where RHE1 is the reference electrode closest to the fuel inlet	67
Figure 15 - Figure showing the limitations of ImageJ thresholding software, A) is the original TEM image of silver nanoparticles with clearly defined aggregated nanoparticles, B) is the same image, optimised in ImageJ software to distinguish background from particles and C) image produced after optimal thresholding, which does not show all nanoparticles present nor distinguish the individual particles	70
Figure 16 - Image of MEA with anode GDE and Nafion membrane visible, some delamination and pin pricks can be seen in GDE due to poor MEA hot press technique.	79
Figure 17 - Single cell test set up in forefront of image, with Scribner test stand in the background.....	81
Figure 18 - Pattern in which bolts are tightened on the Scribner single cell test rig in order to ensure even pressure across the MEA held inside.	82
Figure 19 - Consecutive current density steps from the EU protocol for single cell testing of an MEA	86
Figure 20 - SEM image of cross section of MEA containing the extra Nafion layer, with Nafion membrane visible running from top to bottom of image (M) surrounded by	

microporous CL (Mi) then the more porous mesoporous GDL (Me) on the outside of the image.....	92
Figure 21 - SEM image cross section of MEA without the extra Nafion layer, including yellow line indication the area where the EDX line scan was taken with the F (blue) and C (red) EDX measurements imposed on the image.	92
Figure 22 - EDX of fluorine levels in the two samples shown in the SEM images above, one with and one without extra Nafion applied.	93
Figure 23 - Without Nafion before single cell testing	95
Figure 24 - With extra Nafion before single cell testing	95
Figure 25 - Without extra Nafion after single cell testing	95
Figure 26 - With extra Nafion after single cell testing	96
Figure 27 - 3D renderings of the segmented ortho-slice of the top catalyst layer without extra Nafion	96
Figure 28 - 3D renderings of the segmented ortho-slice of the bottom catalyst layer without extra Nafion.....	97
Figure 29 - 3D renderings of the segmented ortho-slice of the top catalyst layer with extra Nafion layer	97
Figure 30 - 3D renderings of the segmented ortho-slice of the bottom catalyst layer with extra Nafion layer	98
Figure 31 - Comparison of <i>in-situ</i> testing of MEA with extra Nafion added in production and without extra Nafion added in production.	100
Figure 32 - Thermogravimetric measurement showing the loss of carbon leaving the metal content as the residual mass	103

Figure 33 - TEM image of PdIrAu catalyst (dark black agglomerated particles) supported on carbon black (larger onion like particles) annealed at 120 °C under nitrogen.	105
Figure 34 - TEM image of PdIrAu catalyst (large dark black coarsened particles) supported on carbon black (onion like particles) annealed at 600 °C under nitrogen.	105
Figure 35 - TEM image of PdIrAu catalyst (dark black agglomerated particles) supported on carbon black (larger onion like particles) annealed at 400 °C under nitrogen.	106
Figure 36 - HAADF image of PdIrAu catalyst (dark black agglomerated particles) supported on carbon black (larger onion like particles) annealed at 400 °C under nitrogen.	106
Figure 37 - TEM image of the 400 °C annealed PdIrAu sample.....	107
Figure 38 - Magnified top right section on Figure 37 showing PdIrAu/C particles where the lattice spacing is clearly evident.	107
Figure 39 - a) Initial HAADF image, b) EDX map of Ir content, c) EDX map of Pd content, d) EDX map of Au content.	109
Figure 40 - XRF spectra of PdIr/C in low energy region with Pd and Ir peaks highlighted.	110
Figure 41 - XRF spectra of PdIr/C in high energy region with Pd and Ir peaks highlighted.....	111
Figure 42 - XRF spectra of PdIrAu/C in low energy region with Pd, Ir and Au peaks highlighted.....	111

Figure 43 -XRF spectra of PdIrAu/C in high energy region with Pd, Ir and Au peaks highlighted.....	111
Figure 44 - XRF images of a coated circular RDE tip with elemental analysis of a) Au before AST cycles b) Au after AST cycles c) Pd before AST cycles d) Pd after AST cycles e) Ir before AST cycles and e) Ir after AST cycles.....	113
Figure 45 - X-ray diffraction pattern of PdIrAu/C catalyst.	114
Figure 46 - Pourbaix diagrams of iridium, palladium and gold.....	117
Figure 47 - Reducing CO stripping curve with increased Au content in PdAu catalyst.	118
Figure 48 - Graph depicting the remaining ECSA after AST cycling of the PdIr/C and PdIrAu/C catalysts.....	119
Figure 49 - Cyclic voltammograms of PdIrAu/C catalysts after 1000 AST cycles....	120
Figure 50 - Cyclic voltammograms of PdIr/C catalysts after 1000 AST cycles	120
Figure 51 - Comparison of cyclic voltammograms of the PdIr/C and PdIrAu/C catalysts. The onset potential of the PdIrAu/C catalyst is at a higher potential than that of PdIr/C.	121
Figure 52 - Graph indicating the percentage of Ir remaining in the catalyst particles after AST cycling.	123
Figure 53 - Graph indicating the percentage of Pd remaining in the catalyst particles after AST cycling.	123
Figure 54 - Initial polarisation curves for PdIr/C and PdIrAu/C taken after cell break in conditions	125
Figure 55 - Polarisation curves after AST cycling of PdIr/C.....	126
Figure 56 - Polarisation curves after AST cycling of PdIrAu/C	126

Figure 57 - Polarisation curves after 1000 ASTs for PdIr/C and PdIrAu/C taken after cell break in conditions	128
Figure 58 - The cross section of a PEM electrolyser cell, showing the components where the porous transport layers (PTL) are the electrodes	137
Figure 59 - Crystal structure of Ni ₂ P A) four stacked unit cells, B) top down view of (001) surface and C) side view showing the (001) surface.....	142
Figure 60 - Set up of synthesis apparatus after step 4 in Table 13 above.....	146
Figure 61 - HAADF images of Ni ₂ P particles at a) 50 nm zoom and b) 10 nm zoom showing consistent particle sizes throughout the sample.....	147
Figure 62 - TEM image of commercial bulk Ni ₂ P particles were imaged for reference against the synthesised Ni ₂ P nanoparticles.....	147
Figure 63 - TEM image at 50 nm zoom showing well dispersed Ni ₂ P nanoparticles. On the left side of the image the particles are well defined, and their spherical shape is clear.	148
Figure 64 - TEM image at a) 20 nm zoom, b) 10 nm zoom and c) 5 nm zoom showing well dispersed Ni ₂ P nanoparticles.	149
Figure 65 – Sample area with areas without NPs present a) HAADF image of nanoparticles b) EDX map showing red dots for Ni c) EDX map showing red dots for P.....	151
Figure 66 - Concentrated sample area of NPs a) HAADF image of nanoparticles b) EDX map showing red dots for Ni c) EDX map showing red dots for P.....	151
Figure 67 - AFM image of Ni ₂ P nanoparticles in 2D before further manipulation of the image in Gwyddion software.	154

Figure 68 - AFM image showing the amplitude of particles in 3D, agglomeration of particles occurred in the sample production process for the AFM technique.	155
Figure 69 - Pourbaix diagram for nickel at 25 and 100 °C	165

List of Tables

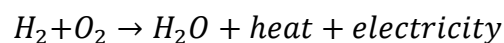
Table 1 - Main fuel cell types.....	3
Table 2 - Factors and results which determine the structure of a bimetallic particle..	21
Table 3 - Factors in Pt dissolution in PEMFCs	23
Table 4 - Equations of the four and two electron pathways of the oxygen reduction reaction.	24
Table 5 - Painting steps used in the application of the CL onto the GDL in MEA preparation.	78
Table 6 - Summary of previous and improved hot press method used for MEA production.....	79
Table 7 - Test conditions at the anode and cathode of a fuel cell.....	83
Table 8 - Short description of standard EU procedure for MEA testing	84
Table 9 - Load test points	88
Table 10 - Surface and Volume measurements calculated from the surface area and volume module in Avizo.	99
Table 11 - Summary of <i>in-situ</i> tests comparing the initial polarisation curves with those measured after 1000 ASTs.....	128
Table 12 - Electrolysis cell types and their common attributes	132
Table 13 - Steps taken during synthesis method development	144
Table 14 - ICP-MS calibration measurements of Ni and P	152
Table 15 - Price fluctuation of key elements studied in HOR catalyst for this work .	159
Table 16 - Suggested step by step work plan to further characterise and assess catalytic ability.	161
Table 17 - Benefits of individual components within suggested catalyst	166

1. INTRODUCTION

1.1. Fuel Cells

Fuel cells are electrochemical devices which produce electricity directly through an electrochemical reaction. Originally invented by Sir William Grove in 1839, they require a continuous flow of fuel to the cell with the overall electrochemical reaction occurring between two electrodes and an electrolyte separating them. The fuel, type of catalyst (on the electrodes) and electrolyte vary depending on the type of fuel cell but, generally, the fuel at the anode is oxidised producing positively charged ions and negatively charged electrons. These electrons flow through an external circuit while the ions move through the membrane to the cathode. Here, they react with the fuel, completing the electrochemical circuit. A comprehensive illustration of the reactions and flows of the fuel cell are shown in Figure 1. This reaction when conducted at low temperatures using hydrogen as a fuel, as in the polymer electrolyte membrane fuel cell (PEMFC), produces only water, heat and electricity.

1-1



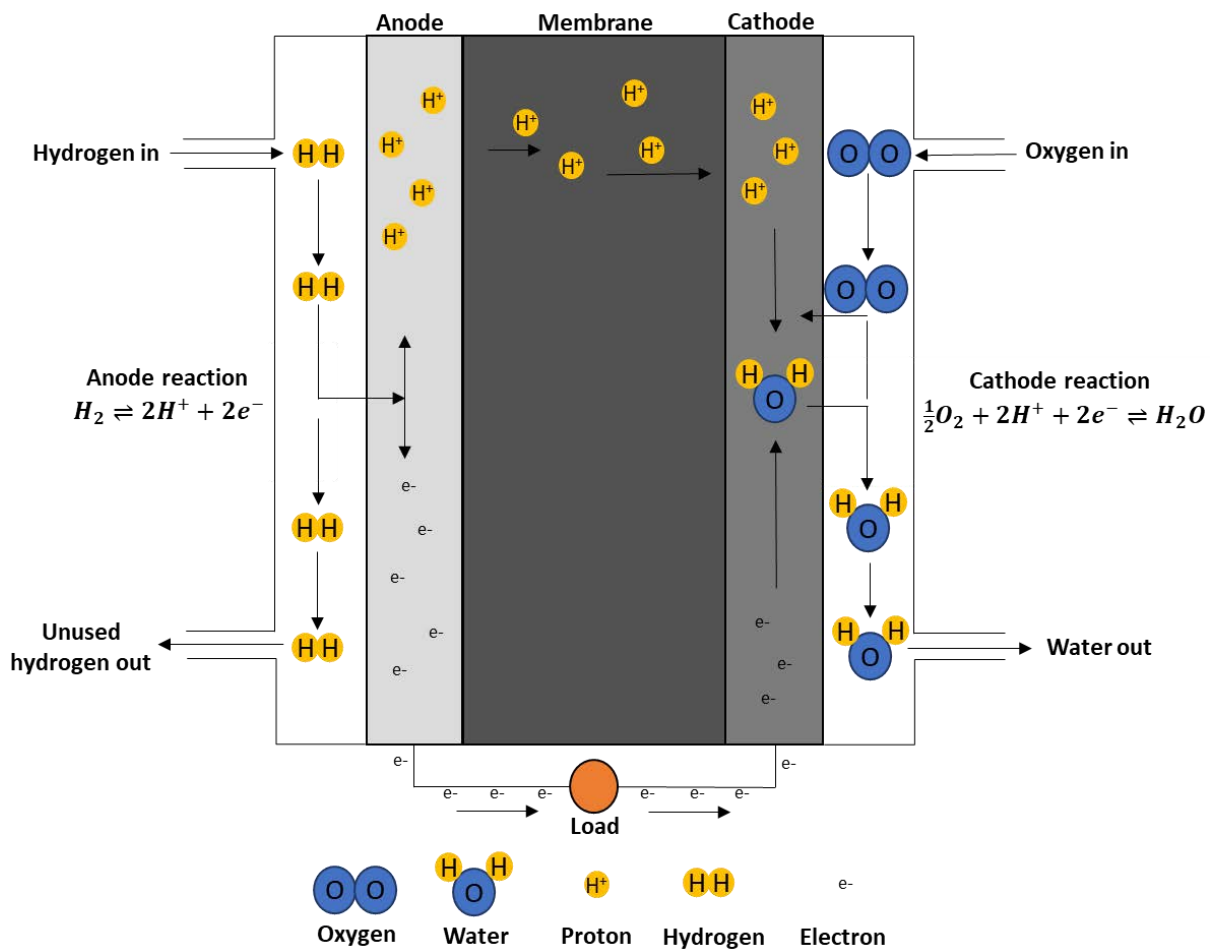


Figure 1 - Diagram showing the reactions and flows within a PEMFC

1.2. Types and background

Largely fuel cells fall into two categories, high and low temperature fuel cells. Higher temperature fuel cells allow for the use of fuels which have impurities as the high temperatures reduce the likelihood of catalyst poisoning. Each type of fuel cell has specific characteristics, which are summarised in Table 1. A brief overview of several fuel cells types is also included below, though this work focuses on PEMFCs.

Table 1 - Main fuel cell types

Fuel Cell Type	Acronym	Fuel	Operating Temperature	Electrolyte	Charge Carrier
Phosphoric Acid	PAFC	H ₂ , CH ₄	200°C	H ₃ PO ₄	H ⁺
Alkaline	AFC	H ₂	>220°C	KOH	OH ⁻
Molten Carbonate	MCFC	H ₂ , CH ₄	660°C	Molten Carbonate	CO ₃ ²⁻
Solid Oxide	SOFC	H ₂ , CH ₄ , CO	500-1000°C	Ceramic	O ²⁻
Polymer Electrolyte Membrane	PEMFC	H ₂	~80°C	Nafion	H ⁺

Reported efficiencies vary widely and therefore were not included in the Table above; however, recent reports of PEMFC and SOFC indicate efficiencies in the region of 60%, though SOFC typically will have higher efficiencies due to their higher temperatures.^{1,2}

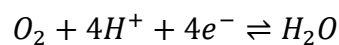
1.2.1. Phosphoric Acid Fuel Cells (PAFCs)

Phosphoric acid fuel cells are most prolific in stationary applications. Two electrodes with platinum (Pt) catalysts are employed alongside the phosphoric acid electrolyte which gives the devices their name. The hydrogen reactant enters at the anode and air at the cathode to achieve the reactions:

1-2



1-3



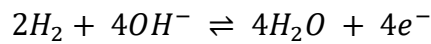
The typical operating temperature of PAFCs is around 200°C, the phosphoric acid electrolyte allows higher temperatures vs. PEMFC due to its higher boiling point, the electrolyte also provides good conductivity and stability compared to other fuel cell (FC) types. The stability of PAFC's has improved with demonstrated lifetimes of over 40,000 hours, in part thanks to investment from the Climate Change Fuel Cell Rebate Program whose aim was to boost the PAFC growth.³ Pt is used as the catalyst in PAFCs due to the acidic liquid electrolyte causing degradation of non-noble metals, though Pt is also susceptible to degradation eventually. The operating temperature also allows the use of natural gas as a fuel, which gives the FC the ability to run at around 40% efficiency, though higher efficiencies can be achieved by using hydrogen. Additionally when using PAFCs for cogeneration of heat and electricity, the efficiencies can be up to 80%.⁴ Start-up times are long due to the operating temperature of the fuel cells and so the devices are often run continuously in large-scale applications. Despite many installed units the cost is still high, which is one of the primary barriers for the widespread exploitation of these cells.

1.2.2. Alkaline Fuel Cells (AFCs) and Alkaline Anion Exchange Membrane Fuel Cells (AAEMFCs)

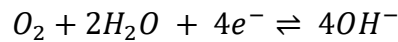
One strategy to reducing the cost of fuel cells is to use alkaline media instead of acidic electrolytes in low temperature fuel cells. Alkaline fuel cells (AFC) have much faster kinetics for the oxygen reduction reaction (ORR) than acidic PEM fuel cells, which provides the opportunity to reduce catalyst loading or use non-platinum metals as the cathode catalyst, though the most common materials used remain Pt and Ni.⁵ These fuel cells were used extensively in spacecraft and indeed gave the Apollo command module its primary source of electric power and the first hydrogen fuel cell vehicle was

an AFC. However, the hydrogen oxidation reaction (HOR) is an order of magnitude slower than in acidic medium and therefore more research is needed to improve the activity on the anode.⁶ The alkaline liquid electrolyte used as the membrane can also be poisoned by the CO₂ in air and so either pure oxygen must be used as a reactant or the air must first be purged of CO₂.⁷ Additionally alkaline fuel cells are bulky due to the use of circulating electrolyte which would rule them out of many applications, such as electric vehicles.⁸ Alkaline Anion Exchange Membranes (AAEMFCs) are another alternative to AFCs which use the same principle but with a solid membrane instead of the liquid used in in AFCs. These operate in a similar manner to PEMFCs but, as the Nafion electrolyte from PEM cannot be used in an alkaline environment, they instead use a OH⁻ conducting membrane. Because of the alkaline electrolyte and OH⁻ conducting membrane the half equations are the same as AFCs.⁹

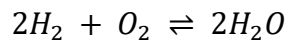
1-4



1-5



1-6

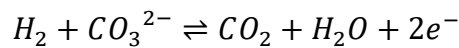


AAEMFCs provide the benefits of liquid AFCs including the fast reaction kinetics while omitting the shortcomings of the liquid electrolyte. For example, in AFCs the liquid electrolyte, KOH, is corrosive to the rest of the fuel cell and is easily poisoned by CO₂.⁹

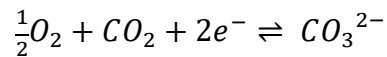
1.2.3. Molten Carbonate Fuel Cells (MCFCs)

MCFCs are also employed in stationary applications and have high efficiencies, in part due to the operating temperature of 650 °C. This fuel cell uses carbonate ions to transfer through the solid matrix electrolyte to the electrodes where the reactions take place:

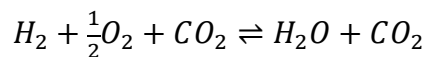
1-7



1-8



1-9



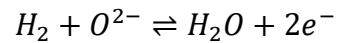
CO₂ is employed as a fuel here rather than being a poison and is recycled from the anode back into the cathode or the anode inlet stream. The electrolyte is Li-K or Li-Na supported by a porous aluminate matrix, which must be strong enough to support the molten alkaline carbonate. Strengthening is also required in the electrodes and this is provided through Cr or Al additives to Ni in the anode and Mg or Fe additives to NiO in the cathode. Problems with this fuel cell type include degradation through cracking of the matrix, however power plant scale demonstrations have been achieved with high efficiencies (60%).¹⁰

1.2.4. Solid Oxide Fuel Cells (SOFCs)

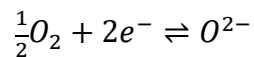
Alongside PEMFCs, SOFCs are the most commonly researched FC, with applications ranging from electric vehicles to stationary storage. Zirconia or ceria compounds are

typically used for the solid electrolyte layer where oxygen ions are conducted across, unusually for fuel cells the mobile ion is O^{2-} which moves from the cathode to the anode as outlined in the reactions below.

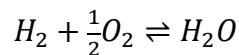
1-10



1-11



1-12

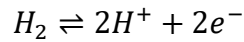


These cells can maintain operating temperatures between 600–1000 °C, though at the lower end of this range there is a larger selection of materials which can be used due to their stability at these temperatures, however improved efficiencies are found at the higher end of the temperatures. Due to the high temperatures, SOFCs employ different materials to other FC types, for example typical catalysts used are perovskite oxides of the rare earth metals (or metals close by them in the periodic table). Nickel yttrium-stabilised zirconia (YSZ) is often used for the negative electrode in high temperature SOFCs as it can provide long term stability under temperatures which may fluctuate.⁸

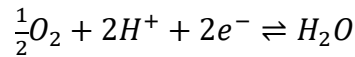
1.3. Polymer Electrolyte Membrane Fuel Cells

The polymer electrolyte membrane fuel cell is currently where the most development lies for commercial applications of fuel cells, especially electric vehicles. The most prominent is the low temperature PEMFC which uses purified hydrogen gas as a reactant and consists of a solid membrane sandwiched between two electrodes both of which contain a layer of catalyst where the electrochemical reactions take place.

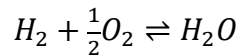
1-13



1-14



1-15



1.3.1. Types of PEM

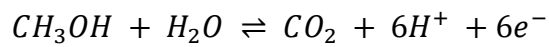
High temperature PEM (HT-PEM) fuel cells operate between 100–120 °C and have some benefits over lower temperature PEMFCs including, better CO tolerance and improved cooling strategies and waste heat management. However, the increase in temperature means different materials are required, for example the maximum operating temperature for the traditional Nafion electrolyte is 90 °C and so new chemistries such as polybenzimidazoles membranes are being considered.¹¹

1.3.1.1. Direct Methanol Fuel Cells

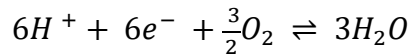
DMFCs operate in the same manner as PEMFCs including having a solid polymer electrolyte and oxygen as the cathode reactant. However, instead of hydrogen as the

anode fuel, methanol liquid is used. Methanol is an attractive fuel due to its high volumetric energy density (when compared to compressed hydrogen gas), which also has the advantage of being easy to store and transport. DMFCs operate at ambient temperature and have reaction equations outlined below. In direct contrast to PEMFCs direct methanol fuel cells produce CO₂ as a by-product limiting their efficacy in reducing carbon emissions.¹²

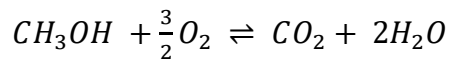
1-16



1-17



1-18



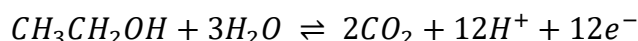
DMFCs also suffer greatly from fuel crossover from the anode to the cathode which causes significant performance loss. This is mainly due to the Pt catalysts, which are used on the cathode for ORR and, are highly reactive to methanol oxidation. This therefore causes a reduction in the cathode ability to perform ORR and reduces the efficiency of the cell.¹³ Additionally if the water to methanol ratio in the FC is not sustained then methanol may be partially oxidize to formic acid, methylformate and formaldehyde which can poison the catalyst. The CO intermediate of the overall DMFC (and DEFC) reaction is also a poison to the Pt catalyst and one prevention method is to alloy the Pt with a oxophilic material such as nickel.¹⁴

1.3.1.2. Direct Ethanol Fuel Cells (DEFCs)

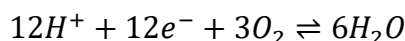
Ethanol is attractive as a fuel as not only does it have a high energy density but it can also be produced from the fermentation of biomass and is less toxic than methanol.¹⁵

The reaction proceeds similarly to the methanol fuel cell above:

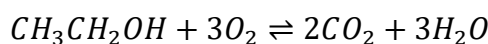
1-19



1-20



1-21

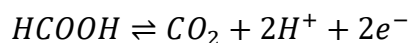


As alcohols are much easier to produce than hydrogen, they provide an interesting fuel alternative as they do not require a sizeable addition to the fuel cell system. Again, Pt is the main catalyst used however this prevents scale up because of its high costs and high activity towards alcohol oxidation, reducing its effectiveness at ORR catalysis. The generation of waste CO₂ also makes alcohol-fuelled fuel cells less attractive in the current drive for zero carbon energy.

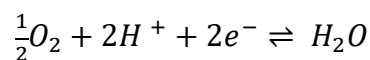
1.3.1.3. Direct Formic Acid Fuel Cells (DFAFCs)

DFAFCs have been investigated for use in portable power applications due to their attractive ability to operate at low temperatures (50–80 °C) and their low toxicity (formic acid is on the US FDA list of safe food additives).¹⁶ DFAFCs run similarly to PEMFCs and DAFCs, but instead relying on the mechanism of the reduction of formic acid.¹⁷ Recent research has proven DFAFCs to have significantly improved oxidation activity compared to DMFCs, thanks in part to the lack of fuel crossover in DFAFCs.¹⁷

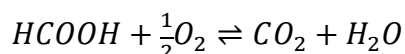
1-22



1-23



1-24



1.3.2. PEM Components

The efficiency of a fuel cell can be calculated by considering the enthalpy of the incoming hydrogen and the out coming electrical energy. By considering all available Gibbs free energy can be converted to electrical energy and using the higher heating value of hydrogen for the enthalpy ($\Delta H_{HHV} = 286 \text{ kJ/mol}$) a fuel cell can be operated at a maximum efficiency of 83 %.¹⁸ Some efficiencies are calculated with the lower heating value of hydrogen ($\Delta H_{LHV} = 241 \text{ kJ/mol}$) which does not take into account the heat of the product water condensation, which can also affect the fuel cell.¹⁹

1-25

$$\eta = \frac{\Delta G}{\Delta H} = \frac{237}{286} = 83\%$$

The efficiency is affected by temperature, pressure and contaminants, each fuel cell component will affect these and so must be designed with optimum efficiency in mind. Figure 2 below shows the individual components of the fuel cell.

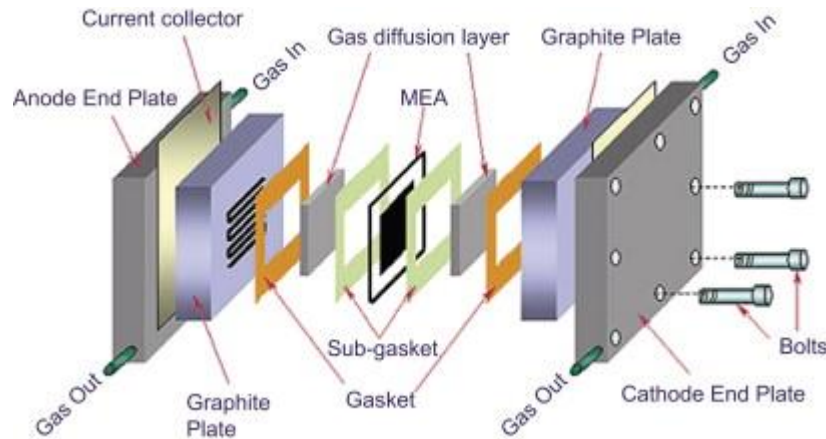


Figure 2 - Illustration of the component parts which make up the fuel cell. Reprinted from PEM Fuel Cell Testing and Diagnosis, Jianlu Zhang *et al.*, Chapter 1 - PEM Fuel Cell Fundamentals, 1-42, 2013, with permission from Elsevier.²⁰

1.3.2.1. Current Collector and Bipolar Plates

Current collectors and bipolar plates are sometimes combined in a fuel cell stack, though in single cells the current collector plate sits behind the bipolar plates (as with the Scribner test stand used in this work). The current collectors provide the electrical connection to the external circuit in which the electrons produced at the anode move. In a fuel cell stack, they also provide the connection between the individual cells. Typically, they are made from copper, stainless steel, titanium or aluminium, the material chosen is a balance of its characteristics as current collectors must be good electronic conductors, highly stable, low cost and lightweight.²¹

Bipolar plate materials range from non-porous graphite to coated metallic sheets to polymer composites. These plates are responsible for fuel and air distribution, conducting electrical current, heat transfer and leakage prevention. A flow pattern is machined directly onto the bipolar plate surface which is in intimate contact with the MEA. Much research has gone into the design of this pattern to achieve the optimum

fuel flow across the MEA, options for these can be seen in Figure 3 below with the most popular being a serpentine pattern (c). The bipolar plates contribute a significant amount to the overall weight of the stack and so the material here is very important to optimise the fuel cell conditions whilst still considering the weight.

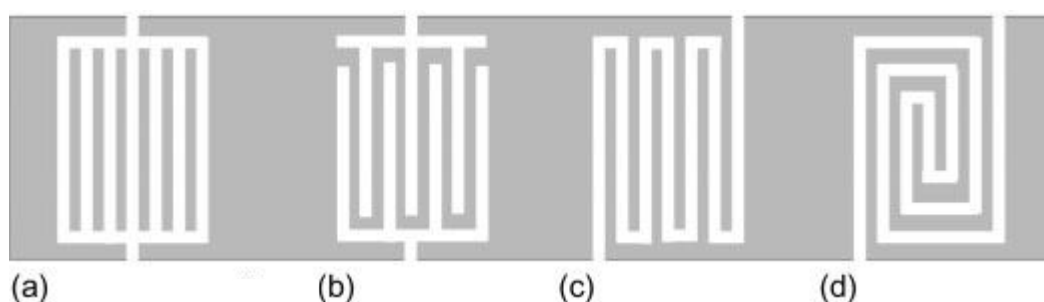


Figure 3 - Different flow patterns for fuel dispersion through the bipolar plate. The pattern is machined directly onto the plate (a) straight, (b) interdigitated, (c) serpentine and (d) spiral. Reprinted from Hydrogen and Fuel Cells (Third Edition), Bent Sørensen, Chapter 3 - Fuel Cells, 107-220, 2018, with permission from Elsevier.⁸

1.3.2.2. Gas Diffusion Layer

The gas diffusion layer (GDL) is at the outer edges of the membrane electrode assembly (MEA). Its key parameters are porosity (and the structure of the pores), surface morphology, hydrophobicity and gas permeability. These are all vital as the GDL is required to provide uniform distribution of the fuel as well as maintaining optimum water levels. The material is usually carbon based such as a woven carbon cloth, paper or foam which meet the requirements above. The pores within the material allow for transport of gases and liquids while the solid parts act as a bridge for electron and heat transfer, therefore, the pore sizes are highly important. Recently it has become common to use a mesoporous GDL with a microporous layer on top where the catalyst layer is in contact, which has shown improved cell performance.²² Water

behaviour within the FC is also dependant on pressure and it is a fine balance to achieve good performance though if the cell stops performing due to this imbalance, it has been shown that PEMFCs can recover from water flooding.²³

1.3.2.3. Polymer Electrolyte Membrane

At the heart of the PEMFC lies the polymer electrolyte membrane, the requirements of which include high ionic conductivity with lowest possible electron transport and reactant crossover. Other requirements include mechanical, chemical and thermal stability.²⁴ In PEMFCs the most common membrane is Nafion a perfluorinated ionomer, created by DuPont in the late 1960's for the chlor-alkali industry and taken up by PEMFC industry in the 1990s. Nafion is sold in different thicknesses and this is denoted by the final number in its name e.g. Nafion 212 has a thickness of 0.002 inches (50.8 μm). Thicker membranes provide longer operating times whereas thinner Nafion is used for higher efficiencies. As can be seen in Figure 4 the backbone of Nafion is polytetrafluoroethylene (PTFE) with a sulfonic acid side chain, it is this side chain which facilitates ionic conductivity once the membrane is hydrated and proton conducting channels form. The ability of the acidic groups to retain water which is essential for the proton transport, and three types of water are present in the membrane: weakly bound, strongly bound and free. Only the weakly bound water participates in the ion transport and this occurs via hopping and vehicular mechanisms.²⁵ The ionic conductivity of Nafion increases with increased water levels until flooding occurs.²⁶

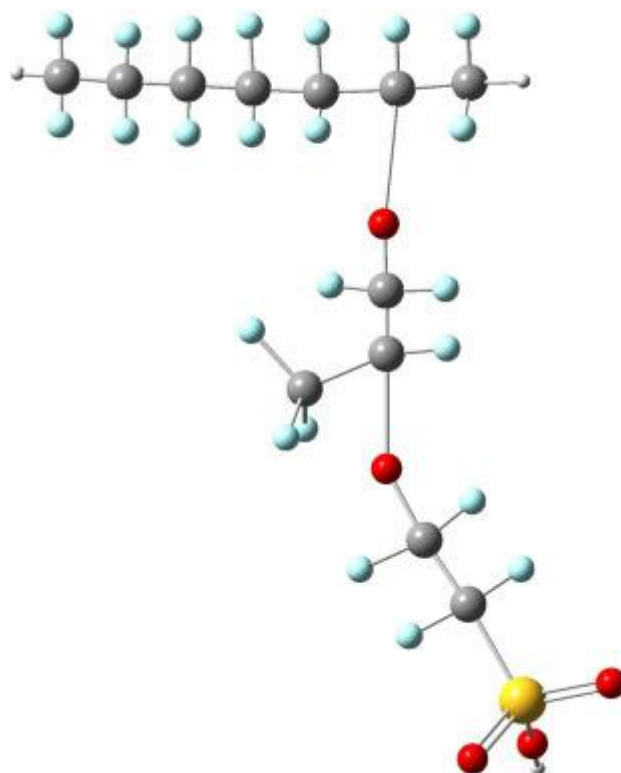


Figure 4 - Nafion structure showing a fluorinated carbon backbone with HSO₃ attached allowing ionic transfer. Reprinted from Hydrogen and Fuel Cells (Third Edition), Bent Sørensen, Chapter 3 - Fuel Cells, 107-220, 2018, with permission from Elsevier.⁸

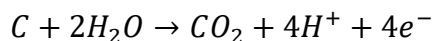
Alternatives to Nafion are being researched to reduce cost as well as for use in HT-PEM.²⁷ There are examples of similar membranes thinner than Nafion which still achieves small hydrogen crossover, including Gore-select, though Nafion is still the market leader by a substantial margin.²⁸

1.3.2.4. Carbon Support

Optimum supports should provide a high specific surface area (SA) to provide the maximum dispersion of the catalyst while providing optimum electron transfer. Most commonly this is a carbon support which provides an enhanced electronic conductivity

and allows the catalyst to be well dispersed throughout the layer. Carbon supports however do suffer from corrosion which is a major degradation mechanism in PEMFCs.

1-26



The Equation above is the oxidation of carbon which occurs at $E_0=0.207 \text{ V}_{\text{RHE}}$. This most commonly occurs at the cathode where the carbon can be exposed to oxidising conditions, especially during start up and shut down but also during normal operating conditions, when the potential is driven up by an air fuel boundary caused by hydrogen flowing into the anode. The results of this degradation are loss of catalyst contacts, disarray of the electrode pore structure and increasing catalyst particle size all of which reduce the PEMFC performance.²⁹

1.3.2.5. Alternative Supports

The degradation of carbon supports mentioned above has led to extensive research into alternatives, both carbon-based and otherwise. The challenges associated with the production of a support include the need for a high surface area, stability, electrical conductivity and porosity.³⁰ Graphene, a material which has been researched in many fields is the most prolifically researched material among FC catalyst supports. The 2D material is a flat sheet of sp^2 carbon atoms, which when stacked together becomes 3D graphite. Its properties, high surface area, electrical conductivity, good thermal properties and its ability to be modified to improve its functionality make it a great option for fuel cell applications. Its synthesis method can be difficult but it may be combined with the addition of the FC catalyst to produce graphene supported Pt, which works well as a FC catalyst layer.³¹ Further combination of this with carbon black has shown

improved mass transport and Pt availability.³² CNTs, diamond and graphite are other carbon based supports studied but perhaps the most interesting are doped carbon supports, which give the ability to either drastically reduce the use of Pt or remove the use of it at all by replacing with heteroatoms.^{33,34} Non-carbon supports such as SiC and TiO₂ have been researched thoroughly, though both have the constraint of lower electrical conductivity, limiting their ability to perform as a good support.³⁵

1.3.2.6. Ionomer

In PEMFCs this ionomer is usually a Nafion solution of around 10 wt%. The ionomer is used to both bind the catalyst to the electrode layer and to allow proton conduction to the catalyst reaction site. This method was devised in the Los Alamos National Laboratory in 1986 when difficulties with the surface area measurements showed as 0.35 mg_{Pt} cm⁻² when in contact with Nafion but 200 mg_{Pt} cm⁻² in H₂SO₄.³⁶ There is a necessary balance required when including the ionomer otherwise either the reaction zone may be too small, or the electronic conductivity may be compromised. Studies from the University of Birmingham laboratory have also shown that by including Nafion ionomer within the catalyst synthesis method itself can further improve the interactions between fuel and catalyst.³⁷

1.3.2.7. Fuel

As mentioned above there are variations of PEMFCs which use different fuels, though hydrogen is the most common. Issues can arise from this as, currently, the largest production method of hydrogen comes from methane. Hydrogen produced in this manner contains impurities such as H₂S and CO, both of which poison the catalyst within a fuel cell. The goal for hydrogen production is to be sustainably produced using

renewable energy to provide 'green hydrogen'; however, there are cost reduction requirements with these technologies as well as an improvement to the current infrastructure. As such, in the interim the CO₂ emitting 'brown hydrogen' can be used as a stopgap. Brown hydrogen often requires purification before it can be used in fuel cells with the ISO standard 14687-2:2012 covering the maximum impurity levels (hydrogen minimum mole fraction 99.97%) which should be used in hydrogen vehicles and stationary applications to ensure optimum performance of the fuel cell.³⁸

1.3.3. Catalyst Layer

The catalyst layer which comprises the catalyst and catalyst support, sandwiched between the GDL and the membrane, is where the electrochemical reactions occur. This layer provides interfaces between the electronic, ionic and gas phases. As always there must be a balance so that the protons can access the reaction site through the ionomer, the electrons can travel through the conductive electrode and the gas can reach the site through pores without the presence of too much water to prevent this. This area is known as the triple phase boundary (TPB) and provides opportunity to improve fuel cell performance by understanding and optimisation. The TPB can be optimised by roughening the surface area of the catalyst increasing utilisation and by adding in an ionomer layer (as described in 1.3.2.6).

1.3.3.1. Platinum Catalyst

Platinum is the main catalyst used in low temperature fuel cells because of its high catalytic ability on both the anode and cathode and although Pt loadings have been greatly reduced in recent years whilst still providing increasing power densities, Pt replacement is considered to be a high priority for research.³⁹ One of the main barriers

against fuel cells is their high price and Pt plays a major role in the makeup of the cost of the fuel cell. Early fuel cells contained up to 28 mg cm^{-2} of Pt, but this has continued to be reduced with the recommended levels for cost utilisation around $0.125 \text{ mg}_{\text{Pt}}\text{cm}^{-2}$ for both electrodes.⁴⁰ In the years since these early fuel cells the Pt loading has been reduced and it has been shown that higher Pt loadings provide a higher voltage throughout the polarisation curve. However, it has also been shown that when the current density is calculated per Pt surface area there is a negligible difference between high and low Pt loading; with the area of primary concern being the overall Pt utilisation.⁴¹ Innovations include Pt binary and ternary alloys, alternative supports, and alternative formats, such as cubes and octahedrons.^{42,43,44} Both Pt-Co and Pt-Ni alloys are favoured in the industrial sector with very small performance differences between the two though at smaller particle sizes PtCo/C has been shown to have improved activity.⁴⁵ The PtCo alloy is also the catalyst used in the fuel cell for the Toyota Mirai and has shown reduction of the activation overpotential compared to Pt alone.⁴⁶ Research publications from Toyota have also shown that in the alloy synthesis lowering the acid treatment voltage allows better removal of free cobalt improving Co dissolution and increasing the mass activity of the catalyst.⁴⁷ One of the key driving factors behind these innovations is the current cost of PEMFCs, around $\$40 \text{ kW}^{-1}$ of which around 40% is the Pt catalyst cost, which must be reduced further to $\$30 \text{ kW}^{-1}$ to reach the DoE targets for 2020.^{40,48}

1.3.3.2. Catalyst compositions

Research has branched out from monometallic catalysts towards bimetallic catalysts for their enhanced performances. Providing novel properties from their monometallic base, the ability of bimetallic particles to combine the benefits of their bulk metal

parents is desirable. Typically, in nanoparticle (NP) form these bimetallic catalysts can provide optimised electronic, catalytic and optical properties. The materials are either alloys, core-shell structure, and variations of these can be seen in Figure 5. The alloying or segregation process of bimetallic and trimetallic NPs is dependent on the NP size.⁴⁹ Core-shell catalysts use @ in the catalyst name to describe which metal is in the shell, for example a Pt@Pd/C catalyst would have a Pt shell on a Pd core, and this structure is then supported on carbon.

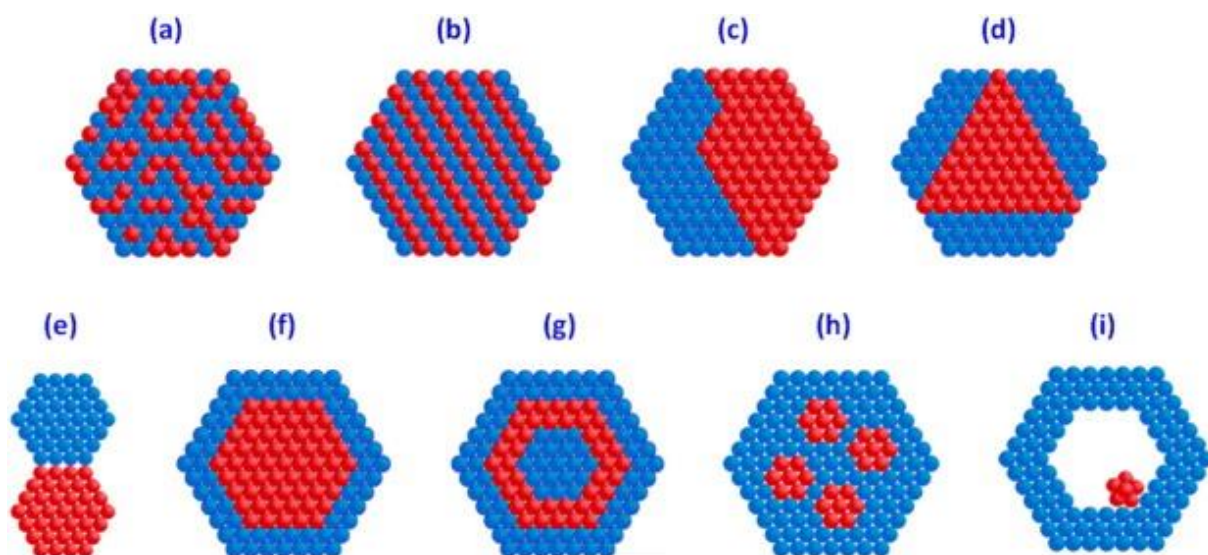


Figure 5 - Different structures of bimetallic catalysts a) mixed alloy b) random alloy c) subcluster with two interfaces d) subcluster with three interfaces e) subcluster with small amount of A-B bonding f) core-shell nanoparticle g) multishell core-shell nanoparticle h) multiple small core materials coated in single shell material i) movable core in hollow shell material. Reprinted from Noble metal-based bimetallic nanoparticles: the effect of the structure on the optical, catalytic and photocatalytic properties, Adriana Zaleska-Medynska *et al.*, Adv. Interface Colloid Sci., 229, 80-107, 2016, with permission from Elsevier.⁵⁰

Typically, if the atomic size of the two metals are similar a random alloy will be produced.⁵⁰ Ferrando *et al.* found that the structure of the bimetallic NPs depends on six factors, where A and B are the elements combined in the bimetallic NP.⁵¹

Table 2 - Factors and results which determine the structure of a bimetallic particle. Information for this Table was taken from Nanoalloys: From Theory to Applications of Alloy Clusters and Nanoparticles, Riccardo Ferrando *et al.*, Chem. Rev., 2008, 108, 3, 845-910.⁵¹

Factor	Result
Strengths of bonds (A-A, B-B and A-B)	If A-B are strongest then a mixed alloy is favoured. If not, then segregation is favoured, and the strongest bonds will lie in the centre of the NP.
Surface energies of A and B	Lower surface energies will move to the surface causing segregation.
Atomic sizes	The smaller atom will segregate to the centre due to sterical forces, particularly in particle shapes which have higher internal compression.
Charge transfer	A combination of two elements which have different electronegativities will favour a mixed alloy.
Binding strength to surface ligands (either from the support or synthesis method)	A strong bond with an external element will segregate to the surface.
Electronic/magnetic effects	In certain cases, electron spin interactions or electronic shell structure may stabilise a composition.

With the atomic size being the dominating factor and the surface energies and bond strengths also being important factors.⁵⁰ Au for example has the lowest surface energies and so typically will segregate to the surface, however it also has an Au-Au bond strength of D^0 218 kJ mol⁻¹ at 298 K which is higher than for example Au-Pd (D^0 143 kJ mol⁻¹) and so this would favour a Au core.⁵⁰ However a prepared Au-Pd bimetallic NP has also shown it will 'breathe' with the Au moving from the core to the surface depending on the potential it is exhibited to.⁵² Showing that the prediction of the structure of a bimetallic particle is very difficult and when a third element is brought in to create a trimetallic, it becomes even more difficult.

1.3.3.3. Enhancement Effects

The enhancement of the catalytic activity of a metal when combined with another element to give a binary or ternary metallic is thought to be due to the following effects.

The ensemble effect where the secondary material changes the distribution of the catalytically active sites.⁵³ This can be considered a dilution of the main component but can open different reaction pathways and an example of this is reducing the poisoning of Pt catalysts by CO by decorating the NPs with Pd.¹⁶ The bifunctional effect is the introduced component providing a reactive intermediate which is needed for the reaction. The ligand effect is the electronic effect where the added metal alters the electronic property of the surface, which can help with improving the stability if the potential range of a reaction can change. Often these effects will work in tandem and it is difficult to ascribe exact catalyst improvements to a particular effect.⁵³

1.3.3.4. Degradation of electrocatalyst

In addition to the degradation from the carbon support mentioned above, the metal particles too suffer from degradation. Due primarily to the harsh conditions in a fuel cell; high humidity, temperature, dynamic loads and acidic as well as oxidising and reducing environments. Theoretically the current catalysts are capable of meeting the targets needed for FCs to become commercial, though their stability must be improved. The metal electrocatalyst NPs degrade through carbon corrosion, dissolution of particles which are then lost to the fuel stream or electrolyte (the subsequent precipitation of Pt in the membrane decreases its stability and conductivity) and poisoning from contaminants in the fuel as well as sintering, also known as coarsening of the NPs.⁵⁴ This coarsening is thought to be due to several factors outlined in Table 3 which uses Pt as example.

Table 3 - Factors in Pt dissolution in PEMFCs. Information taken from A review of PEM fuel cell durability: Degradation mechanisms and mitigation strategies, Jinfeng Wu *et al.*, Journal of Power Sources, 2008, 184, 1, 104-119, to produce this Table.⁵⁵

Factor	Result
Ostwald ripening	Small dissolving Pt particles dissolve and redeposit onto larger particles, increasing their size and therefore reducing the surface area of the catalyst.
Metal oxide formation	The formation of M-O also increases particle sizes, decreasing the surface area.
Cluster-cluster collisions	These random collisions have a 'liquid like' coalescence of particles. ⁵⁶ This mainly affects small particles.

There are mitigating setups used to try to reduce the degradation, such as running at lower temperatures and humidities to reduce the reduction of ECSA, though it has also recently been shown that running at lower humidities increases the carbon corrosion in the catalyst layer.^{57,58}

The dissolution of metals is also highly dependent on potential and pH, as described by the relevant Pourbaix diagram for each metal.⁵⁹ These have been expanded upon and techniques such as inline ICP-MS have been utilised to measure the degradation of metals at different potentials and different pH.⁶⁰ The dissolution mechanism of is now generally agreed that during anodic scanning a surface and subsurface of oxides is formed and a 'place exchange mechanism' takes place, causing the dissolution of the metal. Cathodic scanning produces roughening and surface restructuring due to the reduction of these oxides. In short, the metal oxides are key to dissolution of noble metals.⁶¹

1.3.4. Oxygen Reduction Reaction (ORR)

The oxygen reduction reaction (ORR) is much slower than the hydrogen oxidation reaction (HOR) and so is where much research is focused. Currently the cathode has

a much higher loading of Pt than the anode (the actual amounts vary drastically from FC to FC) to try to improve the slow kinetics of the ORR. As PEM fuel cells use acidic media there are two pathways through which the ORR can occur. These are the dissociative and associative pathways, with dissociative being preferred. The dissociative ‘four electron’ pathway occurs by O₂ adsorbing onto the metal where the O-O bond breaks. As hydrogen gas flows through the fuel cell the oxygen atoms are protonated, and then reduced by the flow of electrons in the electronically conductive carbon layers, leaving adsorbed hydroxyl. These are then reduced and protonated giving water which then leaves the metal surface. The Equations for this process are below (the * shows the sites on the catalyst surface).

Table 4 - Equations of the four and two electron pathways of the oxygen reduction reaction.

Four step oxygen reduction four electron pathway	Initial steps of the oxygen reduction two electron pathway
$O_2 + * \rightarrow O_2^*$ $\frac{1}{2}O_2^* \rightarrow O^*$ $O^* + H^+ + e^- \rightarrow OH^*$ $OH^* + H^+ + e^- \rightarrow H_2O^*$	$O_2^* + H^+ + e^- \rightarrow HOO^*$ $HOO^* + H^+ + e^- \rightarrow H_2O_2^*$

The associative ‘two electron’ pathway also involves oxygen adsorbing onto the metal surface but here the O = O bond does not break. This first part is understood but the next stage, in which H₂O₂ is produced is not clear. The Equations for the initial part of the process are in the Table above.

The amount of H₂O₂ produced by an ORR catalyst is often studied; with little to no H₂O₂ being a sign of an effective ORR catalyst. Another important factor in the

performance of an ORR catalyst is its activity; the catalyst should absorb the substrate strongly enough to break its bonds but weakly enough to release the product. The volcano plot in Figure 6 shows Pt is in the 'sweet spot' for oxygen binding, with the highest activity against other bulk metals for ORR.^{62,63}

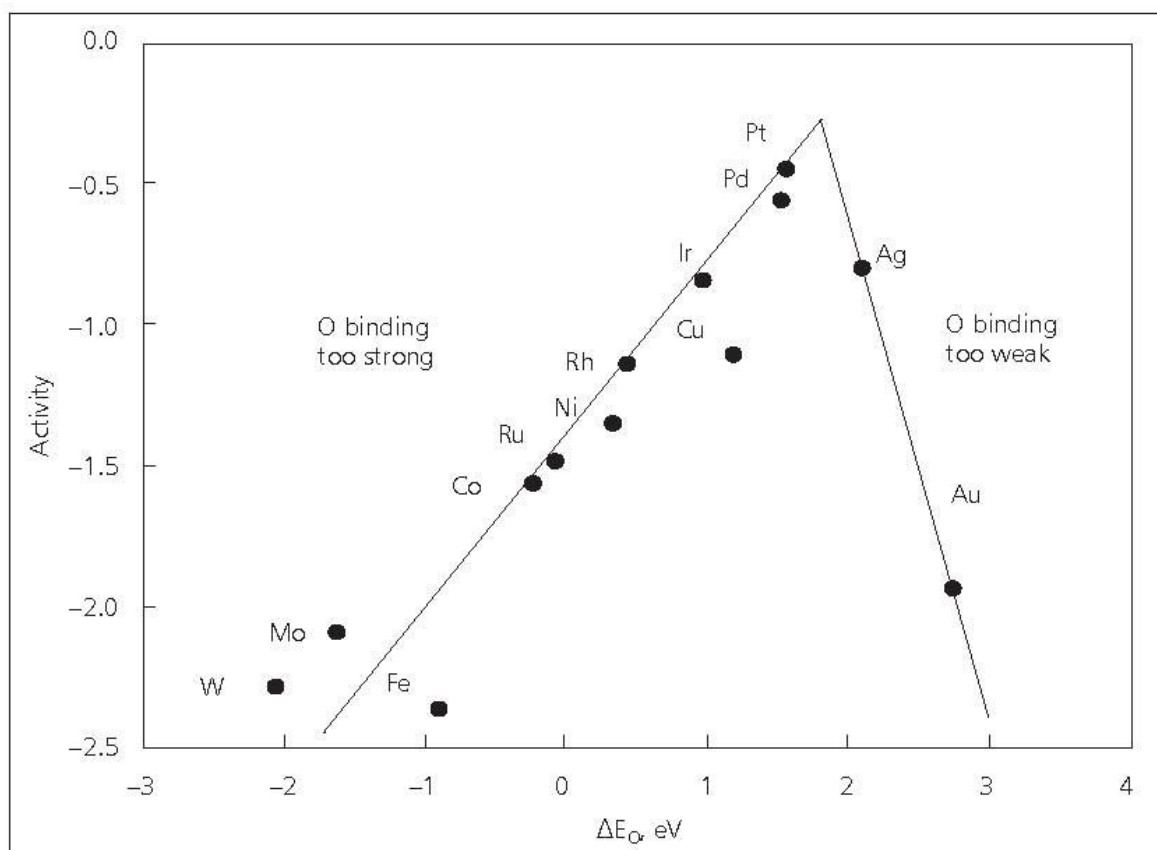


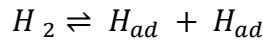
Figure 6 - Trends in oxygen reduction activity plotted as a function of the oxygen binding energy. Reprinted with permission from Origin of the Overpotential for Oxygen Reduction at a Fuel-Cell Cathode, Nørskov J.K. *et al*, J. Phys. Chem. B, 2004, 108, 46, 17886-17892 Copyright 2004 American Chemical Society.⁶⁴

1.3.5. Hydrogen Oxidation Reaction (HOR)

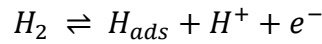
The kinetics of the reaction of hydrogen with the commonly used Pt catalyst at the fuel cell anode are very fast (with overpotentials less than 5 mV) and so cell voltage losses are small even with ultralow Pt loadings (0.05 mg cm^{-2}).⁶⁵ However, there are issues

with using Pt as a catalyst in the anode, including CO intolerance and the high material cost, which have led researchers to utilise other metals and alloys to improve this catalyst. The mechanism for HOR on Pt has been widely researched and is assumed to be the Tafel-Heyrovsky-Volmer mechanism, which has three reaction steps for the adsorption:⁶⁶

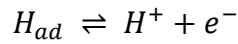
1-27



1-28



1-29



Were the overall reaction occurs either by Tafel-Volmer, Heyrovsky-Volmer or a combination of these two, though this is still debated.⁶⁷ These three steps are now widely accepted though there are still areas of discussion; including the exchange current density, which is often measured far dissimilar than its actual value due to the kinetic and mass transport of reactant effects being difficult to separate.⁶⁸ Additionally the coverage of the adsorbed hydrogen (and the nature of its interactions with different metal catalysts, which will be discussed later) and the interactions within this adsorbed hydrogen layer remains unknown; with some suggesting weakly repulsive interactions between adsorbed H and others an attractive interaction.^{69,70}

1.3.6. Thermodynamics

As previously highlighted the thermodynamics of a fuel cell play a significant role in the performance of the device. At all times the maximum amount of chemical energy a

device, which may be converted into electrical energy is known as the Gibbs Free Energy (G) which can be calculated by:

1-30

$$\Delta G = \Delta H - T\Delta S$$

Where ΔH , the enthalpic change is determined by the maximum amount of thermal energy possible from the reaction, while also considering the irreversible losses from the change of entropy (ΔS).

The thermodynamic cell voltage can also be calculated from the Gibbs free energy of the system using the Nernst equation:

1-31

$$E = E^0 - \frac{RT}{nF} \ln \frac{[H_2O]}{[H_2][O_2]^{1/2}}$$

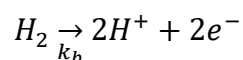
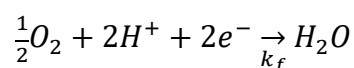
where E is the thermodynamic voltage under current conditions, E^0 the standard conditions, R the gas constant, T the temperature, n the number of electrons, F the Faraday constant and the square brackets represent the thermodynamic activity of the reactants and products, for gases this is equal to their partial pressures.

1.3.7. Kinetics

The rate of the reactions at the electrodes involves electrical charge transfer and a change in Gibbs free energy. The rate of these reactions is determined by the energy barrier which must be overcome when moving from electrolyte to electrode and from electrode to electrolyte. The speed of this reaction can be measured by the electrical current as this is the rate of the electrons being released.

$$i = nFj$$

where i is the current density (the current of electrons per unit area), which can be measured using a potentiostat, nF is the charge transferred and j the flux of reactant per unit area. At equilibrium, when zero net current is generated, the reactions on each electrode proceed at equal rates. Where the forward reaction is the reduction of oxygen at the cathode and the backward reaction is the oxidation of hydrogen at the anode.



Where the k_f is the rate constant of the forward reaction and k_b is the rate constant of the backward reaction. As the consumption of the species is proportional to the species surface concentration the flux j , can be calculated by the rate constant k of the reaction (forward or backward) multiplied by the surface concentration C of the reactant species. Therefore, the net current can be calculated as:

$$i = nF(k_f C_{Ox} - k_b C_{Rd})$$

where C_O is the surface concentration of the oxidised species and C_R is the surface concentration of the reduced species. This will be zero at equilibrium as both reactions proceed in opposite directions equally (this is the exchange current density and is

explored further in Section 1.3.8). The rate coefficients here are a function on the Gibbs free energy:

1-36

$$k = \frac{k_B T}{h} e^{\left(\frac{-\Delta G}{RT}\right)}$$

where k_B is the Boltzmann's constant and h is Planck's constant and Gibbs free energy is calculated using both chemical electrical components:

1-37

$$\Delta G = \Delta G_{ch} - \alpha_{ox} FE$$

where ΔG_{ch} is the chemical component of ΔG . This is for the oxidation reaction, for the reduction reaction α_{ox} would be replaced with α_{rd} . As both the fuel cell reactions are not single step reactions with a single electron involved a transfer coefficient, α , is used. The total of the transfer coefficients for the oxidation and reduction reactions does not have to equal one and it has been shown that Equation 1-38 is true for fuel cells where n is the number of electrons and v is the number of times the rate determining step must occur for the overall reaction to occur once.

1-38

$$\alpha_{rd} + \alpha_{ox} = n/v$$

Therefore, the reaction constant can be calculated as:

1-39

$$k_f = k_{0,f} \exp \left[\frac{-\alpha_{rd} F (E - E_{0,f})}{RT} \right]$$

1-40

$$k_b = k_{0,b} \exp \left[\frac{+\alpha_{ox} F (E - E_{0,b})}{RT} \right]$$

where $k_{0,b} = k_{0,f}$ and these are the rate constants at equilibrium.

1.3.8. Exchange Current Density

The exchange current density is proportional to the standard electrochemical rate constant, though it is not dependent on concentration and can be calculated from the above net current Equation (1-35) above by considering the net current is zero at equilibrium as the forwards and backwards reactions are equal.

1-41

$$i_0 = nFk_{0,f}C_{Ox} \exp \left[\frac{-\alpha_{Rd} FE}{RT} \right] = nFk_{0,b}C_{Rd} \exp \left[\frac{+\alpha_{ox} FE}{RT} \right]$$

Fundamentally, the aim of fuel cell operation is to gain current and so the equilibrium must be deviated from by changing the voltage. This change in voltage alters the reaction rate and also the reactant and product surface concentration. The relationship between the potential and the current and is known as the Butler-Volmer equation and is shown below:

1-42

$$i = i_0 \left\{ \exp \left[\frac{-\alpha_{Rd} F (E - E_r)}{RT} \right] - \exp \left[\frac{+\alpha_{ox} F (E - E_r)}{RT} \right] \right\}$$

where E_r is the equilibrium potential. The i_0 is several orders larger at the cathode than the anode, the i_0 is often quoted as the i_0 at the cathode for the entire fuel cell. The negative overpotential at the cathode makes the reduction term much larger than the

second and predominant therefore, Equation 1-42 can be simplified to just the forward reaction:

1-43

$$i_c = i_{0,c} \exp \left[\frac{-\alpha_{Rd} F (E_c - E_{r,c})}{RT} \right]$$

where E_c is the cathodic potential, $E_{r,c}$ is the cathodic potential at equilibrium, i_c is the current at the cathode and $i_{0,c}$ the equilibrium cathode current.

The exchange current density can also be calculated using Equation 1-44, below, to show the different dependencies of the i_0 . Where i_0 is the exchange current density at any temperature and pressure per actual catalyst surface area, i_0^{ref} is the reference exchange current density at reference temperature and pressure per unit catalyst surface area, A_c is the catalyst specific area, L_c is the catalyst loading, P_r the reactant partial pressure, P_p^{ref} is the reference pressure, γ is the pressure dependency coefficient, E_c is the activation energy, R is the gas constant, T is the temperature and T_{ref} is the reference temperature.¹⁹ The relationship shown in Equation 1-45 is affected by concentration and the ratio of partial pressures may be replaced by a ratio of the concentrations at the catalyst surface. Overall it describes an electrodes ability to undergo the electrochemical reaction and a lower energy barrier has faster kinetics and so a higher i_0 . This is shown by the higher i_0 at the anode, which has more rapid kinetics, than the cathode.

1-44

$$i_0 = i_0^{ref} A_c L_c \left(\frac{P_r}{P_p^{ref}} \right)^\gamma \exp \left[-\frac{E_c}{RT} \left(1 - \frac{T}{T_{ref}} \right) \right]$$

Solving this for the overpotential provides the Tafel equation which is used for analysing catalyst performance in *ex-situ* experiments. The resulting graph can provide the exchange current density and the transfer coefficient from the intercept and slope respectively.

1-45

$$E_c - E_{r.c} = \frac{RT}{\alpha_c F} \ln \left(\frac{i_c}{i_{0.c}} \right)$$

At low overpotentials the Tafel equation can produce artificially high currents as it neglects the back reaction at equilibrium back reaction which is why the technique is not used often for the assessment of anode catalysts.⁷¹

1.3.9. Activation Overpotential

The standard reduction potential E_r in Equation 1-42 is 0 V for the anode and 1.229 V for the cathode at STP and gases and ionic species are ideal.⁷² The difference between this and the electrode potential is the activation overpotential, which is required to generate current.

1.3.10. Polarisation Curve

The most commonly used method of testing the performance of both single cell and complete stack fuel cells is by obtaining the polarisation curve of the cell. It is the most telling test of the makeup and performance of a fuel cell in terms of the cell voltage and power density vs. current density in specific set conditions. The test is performed by changing the current density by small amounts and measuring the voltage response. There are standard procedures for the testing parameters of these tests from both the U.S. DoE and the EU which are discussed later in Chapter 3.^{73,74}

1.3.11. Potential Losses

For a fuel cell at open circuit (OCV) with gas flowing at standard temperature and pressure (STP), the potential could be expected to be close to its theoretical value (1.23 V). This can be calculated as below because the maximum amount of electrical energy (W_{elec}) corresponds to the Gibbs free energy of the system (Equation 1-30).

1-46

$$E = \frac{-\Delta G}{nF} = \frac{237,340 \text{ J mol}^{-1}}{2 \times 96485 \text{ C mol}^{-1}} = 1.23 \text{ V}$$

However, this is not the case in practice and the measured value is typically around 1 V, this shows losses are prominent even when the fuel cell is not running as shown in Figure 7. Losses throughout the polarisation curve are caused by different factors and it is important to understand these effects when running a test MEA. Studying these losses can also indicate where potential problems in the MEA arise and which areas can therefore be improved.

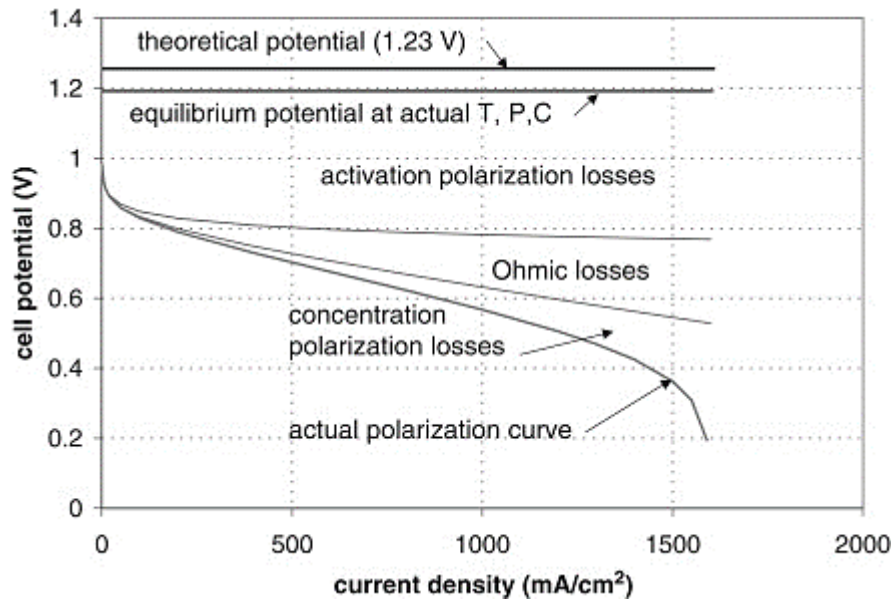


Figure 7 - Resulting polarisation curve due to losses from theoretical polarisation curve. Reprinted from PEM Fuel Cells (Second Edition), Frano Barbir, Chapter 3 - Fuel Cell Electrochemistry, 33-72, 2013, with permission from Elsevier¹⁹

Initial losses stem from the concentration of the reactants and temperature and pressure not being ideal, as they are when calculating the theoretical potential. Activation losses can be explained by sluggish kinetics at the catalyst layer, though these are much higher at the cathode. Again, this is due to the ORR being a much slower reaction than the HOR, and is therefore responsible for the majority of these losses. A small number of the losses can be attributed to internal currents and crossover. Even though the membrane is impermeable, small amounts of hydrogen gas rather than protons will pass through, as will some rogue electrons.⁷⁵ These losses are typically seen at OCV or low current densities where the hydrogen consumption rate is less of a factor.⁷⁶ These internal currents affect both anode and cathode as they occur after the electrochemical reaction has taken place. However, hydrogen crossover occurs before the reaction and therefore does not affect the anode. The hydrogen, which crosses through the membrane, can react with the oxygen (as in Equation 1-15) on the cathode and reduce the cathode potential. Similarly, oxygen

can also permeate the membrane causing the same reaction, though in this case the potential at the anode is reduced. Often a potential lower than 0.9 V indicates a hydrogen leak through the membrane or an internal or external electrical short.

Ohmic losses stem from resistance to the flow of ions and electrons and are expressed through Ohm's law:

1-47

$$V = iR$$

where i is the current density and R the total electronic, ionic and contact resistance within the cell. Electronic losses are very small, and ionic and contact resistances are almost equal. Although R increases with increasing i , typically R is between 0.1–0.2 Ω cm².

Finally, concentration losses are due to the rapid consumption of the reactants at the electrodes. The Nernst equation and Fick's laws of diffusion tell us that the reactant concentration at the electrodes depends on the applied current. Higher currents lower the surface concentration, which reaches zero when hydrogen is consumed at the same rate it reaches the surface. This is the limiting current density at which point the cell cannot provide increased current as no more reactants are available. The limiting current (i_L) and voltage loss due to the concentration (ΔV_{conc}) can be obtained by:

1-48

$$i_L = \frac{nFD C_B}{\delta}$$

1-49

$$\Delta V_{conc} = \frac{RT}{nF} \ln \left(\frac{i_L}{i_L - i} \right)$$

The above Equations combine the Nernst equation with Fick's law of diffusion; at steady state the consumption rate of the reactant is equal to the diffusion flux of the gas phase. Where nF is the charge transferred (C mol^{-1}), D is the diffusion coefficient of the reacting species ($\text{cm}^2 \text{s}^{-1}$), C_B the bulk concentration of the reactant (mol cm^{-3}), δ the diffusion distance (cm), R the gas constant ($\text{J mol}^{-1} \text{K}^{-1}$), T the temperature (K) and i the current density (A cm^{-2}). Though in practice this limiting current is very unlikely to occur in a real fuel cell due to the large differences in area on the catalyst surface, though it may happen at either the anode or cathode.¹⁹

Understanding where the voltage losses originate from a fuel cell can help identify any issues in an MEA when testing such as thickness of the membrane or small holes which may not be obvious to the eye but cause major crossover effects.

1.3.12. Pressure, Fuel and Temperature Effects

Optimum pressure, fuel and temperature should be employed when performing MEA testing and should be consistent from test to test to ensure the results are measuring the desired area of the MEA under study. Small changes to any of these parameters can cause drastic changes within a polarisation curve, rendering tests useless for comparison.

In an operating fuel cell typically the oxygen supply to the cathode will come from air, vehicles like the Toyota Mirai have large inlet fans designed in the vehicle to allow for the flow and capture of this air. Although using oxygen instead of air reduces the likelihood of concentration losses and so at high i a polarisation curve would show less of a drop-in voltage. This is because air contains 21% oxygen, as the Equations above show, concentration of the reactants affect the polarisation curve in all areas and so

an overall improved polarisation curve should be expected when using oxygen, theoretically 56 mV better.¹⁹

It can be shown that the pressure of the reactants and products effects the overall cell potential:

1-50

$$E = E_0 + \frac{RT}{nF} \ln \left(\frac{P_{H_2} P_{O_2}^{0.5}}{P_{H_2O}} \right)$$

Furthermore, the exchange current density, which is connected to the surface concentration, is directly proportional to pressure. For both reasons, an increased pressure provides an increased cell potential. This is the case for both single cell and stacked fuel cells and it has been shown that even the efficiency of the compressor can impact the cell potential.⁷⁷ Increased pressure however comes with an energy demand, as a result, there is an optimum pressure in which the cell potential is increased without imposing an excessive external energy demand.⁷⁸

As entropy, enthalpy and the specific heat of gas all depend on temperature, a change can affect how the fuel cell works, although at low temperatures (below 100 °C) the changes to these would be very small.¹⁸

1.4. Commercialisation barriers

Alongside batteries, fuel cells are hailed as one of the devices which should play a major role in the future energy system to help in the battle against climate change. Despite this, there are still major doubts about the likelihood of fuel cells' commercialisation, with many quoting that the technology is still 10 years from a major breakthrough into the market, as it has been for the last 50 years. The barriers for

commercialisation include the high cost and scarcity of materials which are particular concerns for fuel cell electric vehicles (FCEVs). Saloon cars such as the Mirai still require 10 times more Pt than a diesel fuelled car and so the reduction of the metal for the catalyst is a primary focus, from both companies producing the cars and governments suggested research paths. With current loadings if all worldwide annual Pt production was used in the production of FCEVs this would still only allow for the production of 10% of annual car production.⁷⁹ Not only is this a small amount of the automotive market but fuel cells are applicable to many more vehicles see

Figure 8. Another major barrier to the transport sector is infrastructure, an area in which battery powered EVs are already years ahead, though once installed FCEV stations can serve many more customers due to faster refuelling times and a larger area because of their higher range.⁸⁰ The cost of installing hydrogen fuelling stations is still high though this is expected to drop to as little as \$500,000 for small stations (around 200 kg day⁻¹).⁸¹ The cost of the fuel is also still an issue with 'green hydrogen' from wind or solar costing between \$6–25.4 kg⁻¹H₂ (depending on the system) though 'brown hydrogen' from coal gasification can be as little as \$2.3–5.8 kg⁻¹H₂, though of course 'brown hydrogen' is undesirable, though these costs are reducing and becoming competitive with ICE fuels.⁸⁰

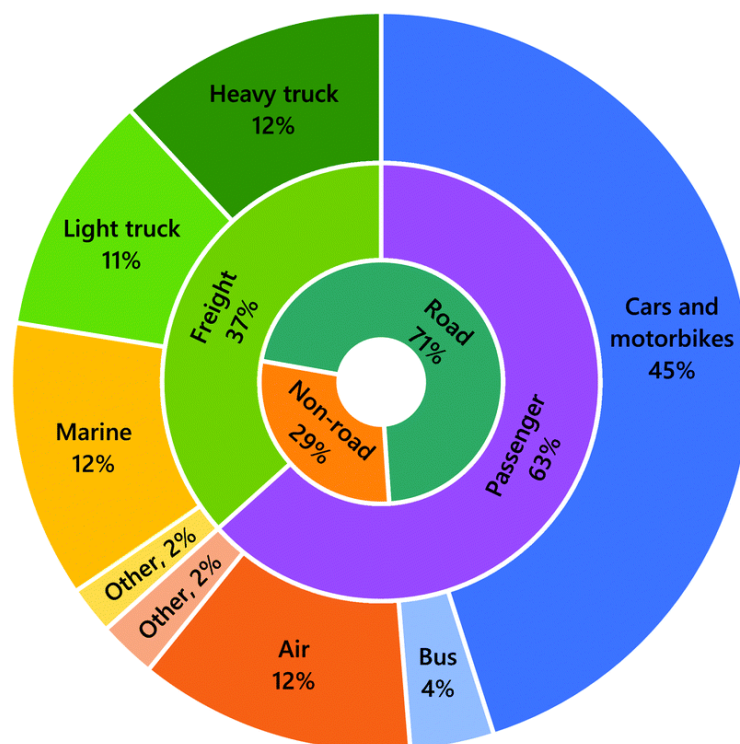


Figure 8 - Transport applications which FCs could be utilised for broken down by energy usage globally in 2015. Total consumption was 110 TJ. Reprinted from: the role of hydrogen and fuel cells in the global energy system, Iain Staffell *et al*, Energy Environ. Sci., 463-491, 2019, with permission from Royal Society of Chemistry.⁸²

Both heat and electricity production markets for homes, commercial and industrial applications could provide significant markets for fuel cells, indeed many devices have been installed in these applications, with hundreds of thousands of homes already powered and heated by fuel cells.⁸³ The use of Pt must be initially reduced and then tuned so that it is used absolutely optimally to allow for sustainable levels of Pt used in the FCs. Overall, FCs are a viable option for the desperately needed clean energy system and with more commercialisation, the current barriers can be conquered.

2. LITERATURE REVIEW ON HOR CATALYST

2.1. Motivation

The focus of fuel cell research has long been centred on the cathode for new catalysts due to sluggish kinetics of the oxygen reduction reaction (ORR), hence the need for high Pt loadings. Consequently, the anode catalyst for the hydrogen oxidation reaction (HOR) is often overlooked because the kinetics of the HOR with the commonly used Pt catalyst are very fast and result in low overpotentials (typically less than 5 mV), even with Pt loadings (0.05 mg cm^{-2}).⁶⁵ However, there are issues with using Pt as a catalyst in the anode, such as CO intolerance and high cost, which have led researchers to develop new Pt free HOR catalysts. The use of Pt as a catalyst is also restrictive due to its supply, 73% of the global annual mined supply came from South Africa in 2018 and almost 25% of the annual demand was supplied from recycling of Pt.⁸⁴ As can be seen in Figure 9 the cost of Pt varies not just yearly but monthly and depends greatly on the current state of the different markets. The demand markets for Pt are highlighted in Figure 10, and the recent drop in price is partly due to diesel car sales decline in Europe and the current trend in gold jewellery which are two of the largest Pt markets.⁸⁴ It is predicted that the increase in the fuel cell market, will increase the Pt consumption, though this is expected to slow slightly due to the changes in subsidiaries in the Chinese market, which is now aiming for a movement for increased infrastructure, rather than for FCEVs alone.⁸⁴

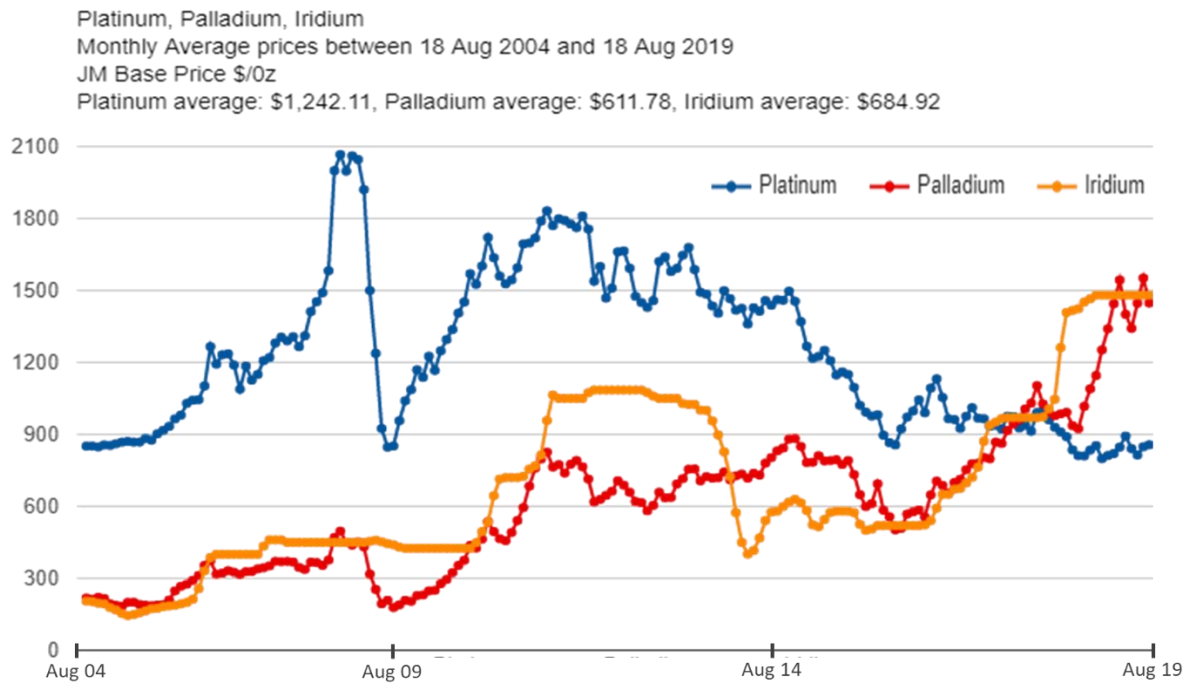


Figure 9 - Monthly values of platinum, palladium and iridium over the last ten years, data and graph from Johnson Matthey

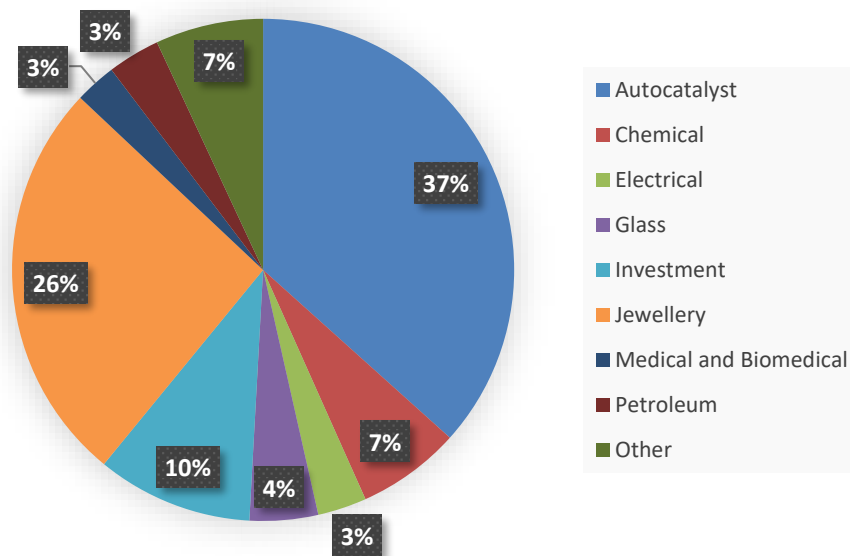


Figure 10 - Percentage breakdown of the demand markets for Pt in 2019. Data obtained from Pgm market report by Johnson Matthey.⁸⁴

Prior to this current period of high Pd and Ir prices (Sept 2017 to present), Pd had also been more expensive than Pt from 2000-2002 due to insufficient supply in the market.⁶⁶ Similarly the current state of the Pd market is due to insufficient supply caused by the expansion in autocatalyst the demand for Pd.⁸⁴ The increase in the recent Ir prices are due to the demand exceeding the current mine output. It is difficult to predict the market price fluctuations for PGM metals and therefore it is important to find alternative non-Pt catalysts and non-PGM group catalysts to improve the fuel cell cost sensitivity. This work not only produces a non-Pt catalyst but also adapts current test methods to improve their use and therefore assessment for catalysts other than Pt.

2.2. Palladium catalysts

Along with other precious metals palladium is an interesting alternative, as Pt and Pd have similar atomic radii size, 139 and 137 pm respectively, and both have a face centred cubic lattice structure.⁸⁵ Although still expensive and reliant on the precious metals market as shown above, Pd is around 50 times more abundant than Pt.⁸⁶ The combination of these factors make Pd an attractive alternative to Pt as a PEM fuel cell catalyst.

The mechanism of HOR on Pd is as yet unclear due to the absorption of hydrogen by Pd which makes HOR measurement studies difficult, though it is expected to be similar to the Equations 1-27, 1-28 and 1-29 due to the similarities between Pt and Pd. Pronkin *et al.* published results from electrochemical impedance and rotating disk electrode voltammetry, which suggested that Pd shows two orders of magnitude lower catalytic activity for the HOR than Pt.⁶⁷ Expanding on the EIS and RDE results using computer modelling they also showed that the Heyrovsky-Volmer (Equations 1-28 and 1-29)

pathway fits the reaction kinetics for the HOR on Pd. The rate of oxidation of hydrogen adsorbed onto Pd is slower than it would be on Pt, due to its free energy of hydrogen adsorption value, ΔG_H , which is close to zero for Pt, meaning it binds hydrogen not too strongly or weakly.⁶⁶ It has been previously shown that by combining Pd with other metals, its ΔG_H value (-0.14 eV) could be shifted to more positive values and so result in a faster rate of hydrogen oxidation.^{87,88} The tuneable activity and stability that catalytic alloys provide has stimulated a wealth of research in the area in recent years.

2.2.1. Palladium alloy catalysts

By considering how the Pd catalyst is behaving at a fundamental level can give insight into combinations of metals for alloys which have potential as a catalyst. A large amount of computational modelling work has been completed on alloy catalysts; one such model by Hammer and Nørskov is particularly useful when considering the properties of alloy catalysts.⁸⁹

The d-band model discusses how the surface chemistry of a parent metal can be significantly changed by alloying it with another metal. This can affect the catalyst properties, as how the particle surface adsorbs is reliant on the electronic structure of that particle surface. The d-band centre of the metal is the average energy of electronic d states on a surface metal atom. A metal surface with a higher d-band centre will more strongly adsorb due to less filling of the antibonding orbital (the fuller the antibonding orbital, the weaker the metal-adsorbate interaction). The model shows that by alloying or changing the surface structure the d band centre can shift causing a change in the metals adsorption properties.⁹⁰ Figure 11 shows this model and how the d-band centre

effects the adsorption of O onto Pd and how as the d-band centre increases the bonds become stronger.

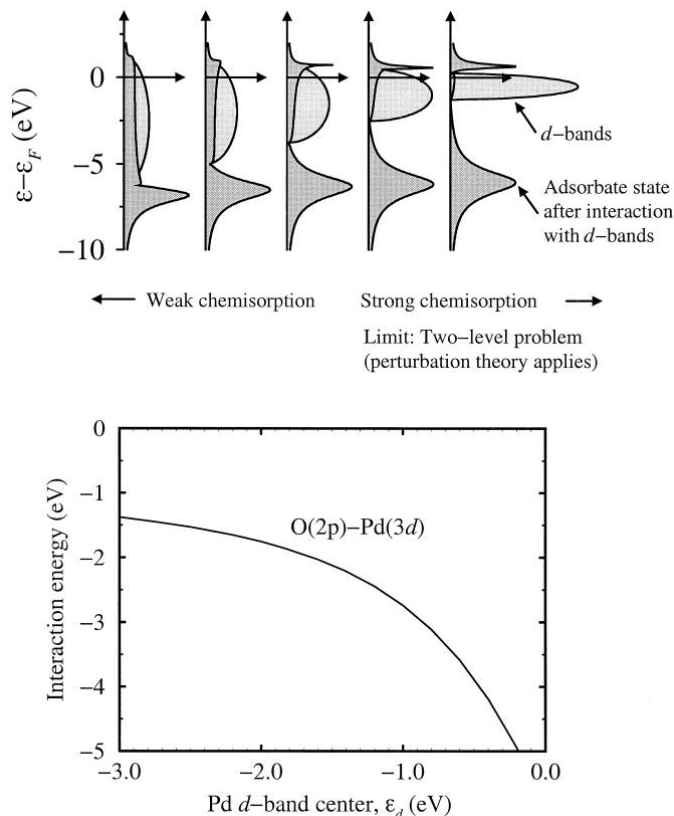


Figure 11 - Illustration of how the Pd-O interaction alters with varying d band centre where as ϵ_d is shifted up toward the Fermi level ($\epsilon_F=0$) the width of the d bands is decreased to allow the number of electrons in the bands to stay constant. Above ϵ_F the antibonding states are emptied, and the bond becomes stronger. Reprinted from Theoretical surface science and catalysis – calculations and concepts, Bjørk Hammer and Jens Nørskov, Adv Catal, 2000, 45, 71-129 with permission from Elsevier.⁸⁹

In the case of catalytic activity towards a specific reaction, the d-band model is important as there is a ‘sweet spot’ where the metal-adsorbate interaction is strong enough allow a fast reaction but weak enough to allow a break in the interaction once the reaction has occurred.

2.2.1.1. Palladium for HOR

By alloying Pd with Pt Cho *et al.* created an electrocatalyst with high HOR activity but with reduced costs.⁹¹ The catalysts contained different atomic ratios of Pd to Pt and

their Pd₇₅Pt₂₅/C had Pt loadings as low as 0.09 mg cm⁻² whilst still providing current densities comparable to those of commercial Pt/C, concluding that the produced catalysts may be promising for commercial HOR.

Core-shell catalysts have also been created for use as a HOR catalyst. Pd@PdIr/C catalysts were initially designed using DFT calculations guided by analysis of Pt catalysis.⁹² The catalysts showed higher activity than commercial Pt/C and were less susceptible to CO poisoning. This higher tolerance to CO (hydrogen gas used in the anode can contain CO gas as it is produced by processing fossil fuels) could potentially overcome the issue of carbon corrosion on start-up and shutdown of a fuel cell as it is thought that Pt poisoned by CO is the cause of this.⁸⁶

2.2.1.2. Palladium for ORR

As noted in Chapter 1 and shown in the ORR volcano plot in Figure 6 Pd metal does not have as high activity towards the ORR as Pt, however when Pd and Pt are combined in a core-shell material an increased ORR activity has been shown.⁹³ DFT calculations have shown that Pd has the highest activity for the ORR after Pt and the (often referenced) volcano plot shows Pd just below Pt for ORR activity.^{62,94} Core-shells are attractive as, by only using Pt on the surface of the particle, the active surface area stays the same while reducing the amount of Pt used. Additionally, the ORR on Pt is restricted due to the rate of removal of adsorbed oxygen species, as the binding energy of the O to the Pt surface is too high. However, this restriction has been reported to be reduced by alloying with other metals, allowing the O binding to be weakened.⁹⁵ Core-shell Pd@Pt/C catalysts have also shown improved stability over Pt/C as the core prevents the cathode reaching potentials where Pt dissolution would

take place.⁹⁶ Zhang *et al.* synthesised core-shell catalysts that have a Pd_{core}/Pt_{shell} structure with different molecular ratios of Pd to Pt. Both Pd₂@Pt₁/C and Pd₄@Pt₁/C showed higher ORR activity than commercial Pt/C, the catalysts were also tested for durability against potential cycling and here Pd₂@Pt₁/C proved significantly better than the commercial Pt. Their Pd@Pt catalysts were produced in a simple one-step reaction, achieving their aim of creating the core-shell particles in a simpler method than had been used in previous work. Their Pd₂@Pt₁/C and Pd₄@Pt₁/C particles were uniformly dispersed over carbon black however, agglomeration occurred with Pd₁@Pt₁/C. This work concluded that during the half-cell reaction the particles altered to a Pt/Pd alloy with a Pt rich surface, this transformation increased the ORR activity, which proves the core-shell concept. Further core-shell work has focused on tertiary alloys, for example a Pd@Pt core-shell decorated with iridium has shown better ORR activity and PEMFC performance than Pt alone.⁹⁷

2.2.1.3. Palladium for AAEMFCs

The faster HOR and ORR kinetics in alkaline pH mean fewer active catalysts are a possibility and therefore cheaper options can be utilised. PdIr is one such combination which has been prepared for the HOR in an alkaline environment. Jervis *et al.* have shown that PdIr/C can have activities comparable to Pt/C for the HOR.⁹⁸ Their PdIr/C catalysts were created using the simultaneous reduction method, metal salts of Pd and Ir were mixed and sodium hypophosphite was used to reduce the metals to obtain the PdIr alloy. This produced nanoparticles with an average size of 10 nm, which could replace Pt/C as the catalyst for HOR and therefore reduce the cost of the FC as both Pd and Ir are cheaper than Pt (at the time of publication).⁹⁹

Sekol *et al.* have researched the combination of silver with Pd as an alternative catalyst for the ORR in AAEM.¹⁰⁰ Choosing Ag because of its similarities to Pt for the ORR and utilising core-shell concept for its possibilities of modifying the d band centre to alter the adsorption and activation energies. They created core-shell nanoparticles supported on multiwalled carbon nanotubes (Ag@Pd/MWNTs), with the aim that the MWNTs would increase the surface area and stability of the support. As the Ag also makes the catalyst more selective to oxygen over ethanol and methanol, PdAg catalysts could also lend themselves to the cathode reaction for DAFCs as will be discussed later.

2.2.1.4. Palladium for DMFCs

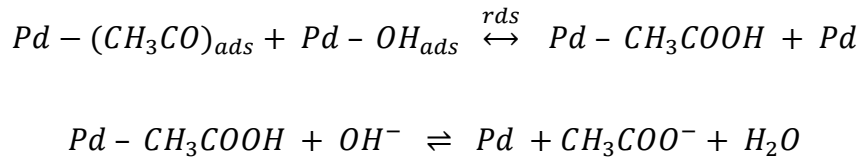
The tolerance to methanol of Pd has led to novel cathode catalysts for DMFCs, including Pd alloys. It is important for the cathode to be tolerant to methanol, as this prevents reaction of any reactant crossover and thus not adversely affecting efficiency of the fuel cell. Palladium selenides have recently been investigated for their catalytic ability in a DMFC, due to their tolerance of methanol.¹⁰¹ PdSe, PdSe₂ and Pd₃Se were synthesised via the hydrothermal method and tested in acidic medium for their ORR activity in DMFCs. PdSe provided higher ORR activity than Pd alone though both PdSe₂ and Pd₃Se gave lower activities. Pt was not used as a comparison in these tests, making it difficult to compare with what is currently on the market.

2.2.1.5. Palladium for DEFCs

The largest portion of papers involving Pd as a catalyst were researching its use in DEFCs, specifically in alkaline media. Pd has been researched to such a high extent in this area due to both its tolerance at the cathode and its superior activity at the anode

in alkaline electrolyte. Pd is almost inert for ethanol oxidation in acidic medium and so, not an option for this type of catalyst.¹⁰² The commonly accepted mechanism is ethanol is oxidation to acetic acid via adsorption on to Pd, the rate determining step (rds) is due to removal of the adsorbed ethoxy in Equation 2-1 which is affected by the OH_{ads}.¹⁰³

2-1



Cui *et al.* reported that this inertness in acidic and neutral media could be due to the lack of OH species which can provide quick removal of hydrogen, whereas this is not an issue in alkaline media.¹⁰⁴ Alkaline DAFCs have been receiving more attention recently due to their faster kinetics than acidic media at both the anode and cathode.¹⁰⁵

A number of papers in recent years have focused on PdAu as the combination of Pd with Au, with the aim of improving the stability and activity of Pd. There are many theories around the improvement of the Pd catalytic ability, one being that the addition of Au has the potential to improve the stability by reducing the amount of metal dissolution during the running of the FC.¹⁰⁵ Another is that as the PdAu/C onset potential is more negative than Pd/C alone, which could aid the removal of the intermediate species (CH₃CO_{ads}) therefore improving the RDS Equation 2-1.¹⁰⁶ Feng *et al.* produced PdAu/C particles with different atomic ratios, all of which provided higher EOR activity and better stability than Pd/C alone. Pd₁Au/C showed the highest performance, with over 11 times higher activity than Pd/C.¹⁰⁶ Xu *et al.* also created a range of PdAu/C electrocatalysts, and they found the optimum ratio to be Pd₃Au/C, as

it had the highest stability of the range and in single cell testing it performed similarly to Pd/C.¹⁰⁵

Much DAFC bimetallic catalyst work has focused on the combination of palladium and silver, with the aim that this addition will alter the d-band centre and provide a more efficient and cheaper electrocatalyst. Li *et al.* created PdAg/C catalysts with different atomic ratios. These were heat treated at different temperatures which provided different particle sizes.¹⁰⁷ This paper showed that the prepared PdAg/C catalysts had enhanced EOR activity over the Pd/C catalyst with an Ag content of 25–33% giving the best results. Additionally, Li *et al.* concluded that the degree of alloying of the PdAg/C catalysts was independent of the reducing temperature. Prior to 2010, several researchers focused on PdAg alloys for the catalytic ability in DAFC, which was established. The following papers include recent work, which implements innovative methods to increase this activity of PdAg electrocatalysts. Peng *et al.* created ‘hollow porous raspberry like PdAg nanosphere catalysts’, which provided higher activity towards EOR than Pd/C.¹⁰⁸ It was thought that this high activity could be due to the porous hollow particle allowing the internal surface of the catalyst to be utilised and therefore increasing the electrochemically active surface area needed for the EOR. Research groups have also studied PdAg on different supports, particularly graphene oxide due to its high surface area and its mechanical, electrical and thermal properties.^{109,110} Lui *et al.* made reduced graphene oxide (RGO) supported PdAg catalysts, by reduction of metal salts and GO with urea assisted ethylene glycol.¹¹¹ When compared to the PdAg/MWNTs the group also made by the same method, the PdAg/GO proved superior, giving higher EOR activity, stability and tolerance to CO. Kakaei and Dorraji followed this research with a simpler one pot synthesis method due

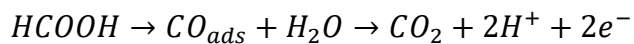
to the difficulty in scale up the previous GO method used by Lui *et al.*¹¹² MWNTs would also be an interesting support for PdAg, MWNTs were mentioned earlier as a support for the ORR reaction in alkaline fuel cells and the PdAg/RGO MWNTs have also recently been synthesised and used for H₂O₂ sensors.^{100,113}

PdIr has also been researched as a DAFC catalyst with a carbon support.¹¹⁴ Iridium has previously been used in binary and ternary Pt alloys for the EOR, as it is considered to improve both stability and activity.⁹⁷ Different atomic ratios were prepared via borohydride reduction method. Using chronoamperometry to analyse the EOR they found the Pd:Ir (90:10) gave the best electrocatalytic activity, these catalysts had an average size of around 5 nm.

Pb is also considered to have a promoting effect on the EOR reaction and when combined with Pt has shown enhanced activity.¹¹⁵ Wang *et al.* produced PdPb/C catalysts with different amounts of Pb, they found that Pd:Pb 4:1 gave the best activity. They also completed CO stripping experiments which showed, the addition of Pb aids the removal of CO (a catalyst poison), this may explain the higher activity.¹¹⁶

2.2.1.6. Palladium for DFAFCs

Pd has been widely studied for use in DFAFCs because of its activities for the anodic formic acid reduction reaction, which has proven superior catalytic activity to Pt even at low temperatures.¹¹⁷ The Pd breaks only the O-H bonds within the potential window and therefore works differently to the Pt catalyst and instead proceeds via the dehydration mechanism. However, it is vulnerable to acid dissolution, which causes durability issues, though it is not poisoned by CO as Pt is.



Chen *et al.* created Pd@Ir core-shell particles with an optimised ratio of Pd to Ir, this work expanded upon a previous paper by Wang *et al.* who showed Ir can improve the Formic Acid Oxidation Reaction (FAOR) by reducing the adsorption strength of CO on Pd, however optimisation of the ratio of Pd to Ir is important as Ir cannot oxidise formic acid.^{118,119} Chen *et al.* worked to improve upon their findings and the core-shell Ir/C@Pd catalysts were produced by decorating Ir nanoparticles with a Pd shell using a two-stage route of borohydride reduction, PdIr/C and Pd/C were also produced to be used as a benchmark. The core-shell particles showed higher activity than the benchmark particles, even when considering the mass of metal loading. They then published a separate paper which detailed their results of using CNTs as a support for PdIr catalysts.¹²⁰ The CNTs underwent a sonochemical pre-treatment to import oxygen containing functional groups onto their surface before the PdIr particles were deposited. This pre-treatment was completed to improve the dispersion of the PdIr on the CNTs. Again, these particles showed better catalytic activity than PdIr/C and Pd/C.

Palladium silver nanowires (NW) are also an option for DFAFC, and offer a relatively simple synthesis option as Lu and Chen have shown, they may be synthesised in one step.¹²¹ These nanowires have proven to be alloys and are supported on carbon black. The NWs had smaller charge transfer resistance to FAOR than Pd/C, indicating that the kinetics would also be faster, which would make the NWs a useful catalyst. Feng *et al.* researched the ability of Au to promote Pd for FAOR, the results showed the Pd on Au nanostructures produced a higher activity toward the FAOR with Pd being highly dispersed.¹²²

2.2.2. Summary of Review

As highlighted above Pd has the potential to improve catalytic ability and stability in many types of fuel cells all whilst providing an alternative to Pt. Further work is required in all areas, to improve understanding of the mechanisms involved and to achieve the optimum catalyst. For example, particle size, support, synthesis method and annealing can all have large effects on the catalysts ability and therefore further research will achieve better results.

2.2.3. Palladium Iridium Catalyst

Durst *et al.* have previously shown the reactivity at the anode within a fuel cell follows the order $\text{Pt} > \text{Ir} > \text{Pd}$ for the HOR.¹²³ By alloying Pd with Ir there is a possibility of a ΔG_{H} value closer to zero as Ir has a positive ΔG_{H} , while also taking advantage of Ir HOR catalytic reactivity. Pd and Ir have previously been alloyed together for their use as an ORR catalyst, as well as for HOR in alkaline media: Jervis *et al.* presented improved activities over commercial Pt/C and showed alloying of the catalyst.¹²⁴ As stated above, Ir has also shown high catalytic activity for the HOR, second only to Pt, and because of its high redox potential ($\text{Ir}/\text{Ir}^{3+} = 1.16 \text{ V}$) a PdIr alloy can potentially provide Pd with improved stability.^{97,125} Pd and Ir have found use in a wide range of catalytic applications, Ir has also been used to decorate PdCu surfaces to improve the ORR activity.¹²⁶ Recently Pd and Ir were used in a four metal ORR catalyst, Pt shell PdIr/Ni core, the synthesis step was a simple two step synthesis method and each combination tested (different amounts of Pd, Ir and Ni) had improved activities over the commercial Pt, thought to be due to a decrease in the Pt d-band centre upon alloying.¹²⁷

2.3. Palladium Iridium Gold Catalyst

Gold is a useful metal to alloy with Pd to alter its reactivity and has been extensively studied, not just for HOR but also for alcohol oxidation and hydrodehalogenation.^{106,128} Previous PdAu papers for HOR have focused on supported thin film nanoparticles for example Al-Odail *et al.* showed the highest specific activity of PdAu with Au at 60% atomic ratio.¹²⁹ Simonov *et al.* expanded on previous PdAu research by pre-treating with ethylene to in an effort to further reduce the CO poisoning.¹³⁰ Their previous work had shown that by incorporating C into the crystalline lattice of Pd, the electrochemical properties of the resulting metal nanoparticles.¹³¹ The particles were synthesised by reducing the prepared PdAu₂ nanoparticles in H₂ at 90 °C, this was then followed by C₂H₂ treatment at 300 °C. It is this ethylene pretreatment which provides the incorporation of C into the lattice. The produced PdAu₂-C_x particles provided improved catalytic activity and CO tolerance, which was confirmed by RDE measurements. Both Pd and Ir metals have shown improvements in their ORR activity when a third alloying element was introduced, such as iron or gold.^{126,132,133} Many papers have explored PdAu alloys for their HOR/HER activity and CO tolerance.^{129,134} As Au is the noblest metal, it is the least likely to dissolve under potential cycling.¹³⁵ The addition of Pd into an Au catalyst for acetoxylation of ethylene to vinyl acetate was probed to identify why this match can improve the catalytic ability. It is thought to be due to the 'ensemble effect', in that the Pd monomers inhibit the formation of undesirable products, such as CO and CO₂.¹³⁶

As described above, the three metals, Pd, Ir and Au have previously shown promising results as a catalyst when they are alloyed together. The following Chapter describes the synthesis of PdIrAu/C and compares the results to PdIr/C catalyst. The PdIr/C

catalyst is a product produced by Amalyst Ltd. for the HOR reaction in a PEM fuel cell, the aim of adding Au to create a ternary catalyst is to improve the catalyst stability via the ligand effect by increasing the potential range at which the catalyst degrades. This increase in potential range at which the majority of the catalyst degradation occurs will remove the likelihood of the catalyst degrading in the anode potential range (0–1.0 V).¹³⁷ This work was sponsored by Amalyst Ltd. and their aim was to assess the viability of adding another element into their commercial PdIr binary catalyst to produce a ternary catalyst and assess if this could improve the overall stability. Their PdIr catalyst was already sold commercially and had proved comparable results to the industry standard Pt, at a lower cost.

2.4. Synthesis method of PdIrAu/C

The synthesis method utilised in Chapter 5 was chosen with nanoparticle size in mind. Hutchings has published prolifically in the Au catalyst area and has shown that the synthesis method of Au catalysts should be utilised to obtain the composition and size of the particles needed for their application.¹³⁸

3. METHODOLOGY

This Chapter will outline the methods and materials used throughout this piece of work and highlight the theory of techniques utilised throughout the different Chapters whilst researching fuel cell and electrolyser catalysts and analysing the Nafion content used in the production of a test MEA.

3.1. Materials

Nafion dispersion D1021 water based (Ion Power, 1100 EW at 10 wt%), 2-propanol HPLC grade (Sigma Aldrich, 99.5%), ultrapure water with the resistivity measured as $\geq 18.2 \text{ M}\Omega\cdot\text{cm}$ (Millipore), sulfuric acid (Sigma Aldrich, 85% diluted to 0.1 M). GDE ELE0165 (Johnson Matthey), GDL with a Pt catalyst layer of $0.4 \text{ mg}_{\text{Pt}}/\text{cm}^2$ (Johnson Matthey), Nafion 212 (Dupont), Sigracet GDL 35 BC (SGL Carbon). PdCl_2 (Sigma Aldrich, 99%), IrCl_3 (Heraeus Chemicals, 54% metal content) and $\text{HAuCl}_4\cdot 3\text{H}_2\text{O}$ (Sigma Aldrich, 49 % metal content), PVA (Sigma Aldrich, M_w 80,000), NaBH_4 (Sigma Aldrich, 98 %), carbon Vulcan XC-72R (Sigma Aldrich), Nickel (II) acetylacetonate (acac) (Sigma Aldrich, 95%), 1-octadecene (Sigma Aldrich, 90%), oleylamine (Sigma Aldrich, 70%) and tri-n-octylphosphine (Alfa Aesar, 85%). All chemicals are reagents were used as received without further purification.

3.2. Electrochemical Techniques

Ex-situ electrochemical techniques have several benefits over *in-situ* testing namely: quicker analysis of catalytic activity, reduced interference from complications in the test method, a reduced quantity of catalyst required and faster degradation testing. These all allow for faster screening of a synthesised catalyst, providing specific results of the catalyst behaviour rather than a compound result of the catalyst within a system. A

three-electrode cell is comprised of a working, reference and counter electrode, all of which are vital in voltammetry and play a unique role in analysis.

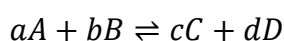
It is useful to think of the overall system with thermodynamics in mind; and, how this may predict the direction of the chemical reaction. The change Gibbs free energy, ΔG , of a system predicts whether a reaction will be spontaneous or not and is smallest when the system is at equilibrium. In relation to an electrochemical cell, the ΔG can be related to the cell potential under standard conditions via the Nernst equation, which accounts for both the chemical and electrochemical energies.

3-1

$$\Delta E = \Delta E^o - \frac{RT}{nF} \ln \left(\frac{C^c D^d}{A^a B^b} \right)$$

Where E is the cell potential, E^o the standard cell potential, F the faraday constant, and n the number of moles of electrons; $\ln \left(\frac{C^c D^d}{A^a B^b} \right)$, the natural log where the uppercase letters are the concentrations of the species and superscript letters the stoichiometric coefficients:

3-2



The Nernst equation highlights that the cell potential is dependent on the reactant concentration and allows the total voltage of an electrochemical cell to be determined.

3.2.1. *Ex-situ* set up

A typical *ex-situ* set up is illustrated in Figure 12 below. It consists of a three-electrode cell where the measurements are performed containing a working, reference and

counter electrode, in addition to electrolyte. This system is connected to a potentiostat, which both controls, and measures the polarisation of the working electrode where the catalyst has been deposited.

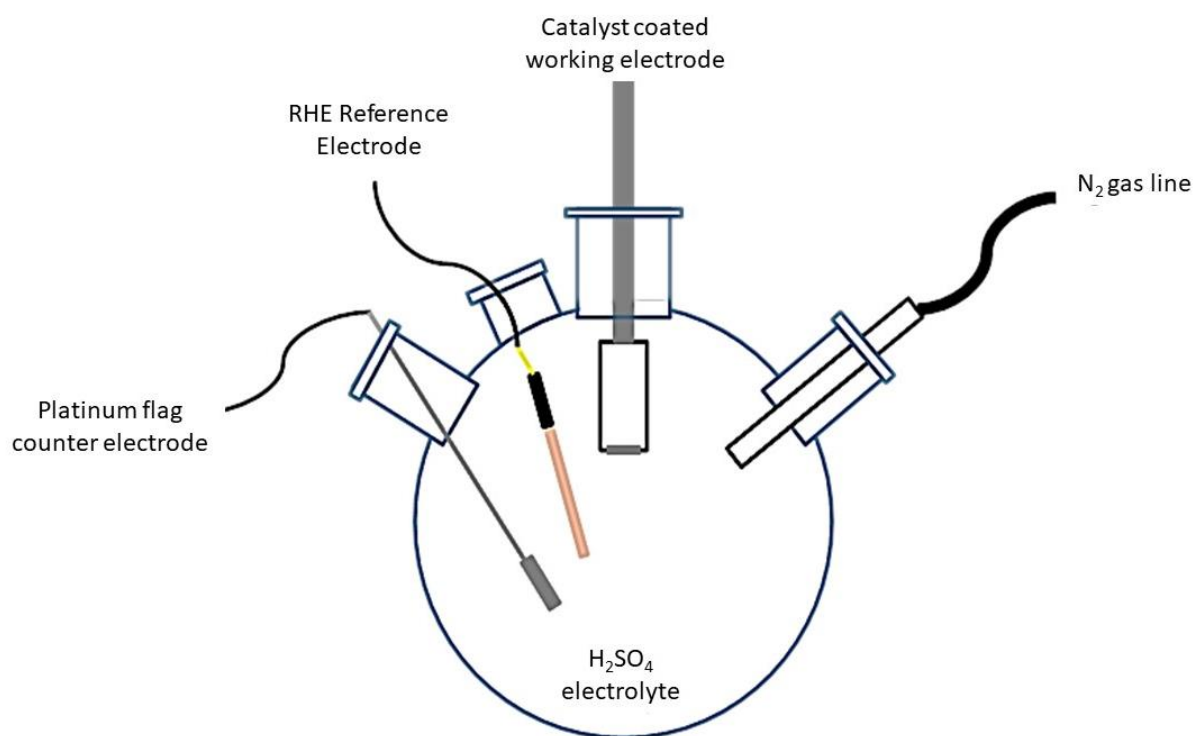


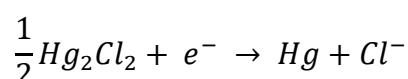
Figure 12 - Illustration of *ex-situ* three-electrode cell set up.

3.2.1.1. Reference Electrode

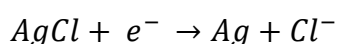
The reference electrode provides the potential difference needed to allow the potential change at the working electrode during testing to be measured. The reference electrode can be produced from many different materials, all of which will have a different half reaction and so a different potential difference. Potential values in literature will always be quoted against the reference electrode used. In this work, the reference electrode used was initially a leakless Ag/AgCl electrode, a relatively

common electrode. The electrode comes in non leakless form though the leakless version was chosen to prevent unaccounted for reactions with chloride ions which can leak from the electrode. The electrode was not suitable for long term degradation testing as it was found that the potential drifted over time and this could not be accounted for. As a result of this, all affected experiments were repeated with a reversible hydrogen electrode (RHE) and all values quoted in this work are vs. RHE ($E^\circ = 0.0 \text{ V}$). It is important to check the potential of the reference electrode against a known value before each experiment to ensure potential drift has not occurred. In the RHE's case, before use the electrode was entirely purged (until all electrolyte in contact with Pt was replaced by gas) first with oxygen to clear away any impurities followed by filling with hydrogen and measuring the potential against a saturated calomel electrode, this process helps ensure consistent potential measurements. The hydrogen reference electrode used in this work was not shiny Pt but Pt black coated to provide sites for catalysis as platinum black has a larger surface area, enabling fast reaction kinetics to rapidly establish equilibrium for the potential to be determined. If this was not the case, then the potential could not be guaranteed. As IUPAC require that all potentials are reported against SHE, the move to using this electrode simplified the analysis of measurements. The standard electrode potentials of the other common reference electrodes, calomel and silver/silver chloride electrodes (as with all other reference electrodes) come from their redox couple reactions, shown below:

3-3

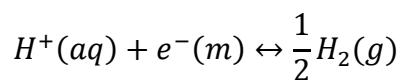


3-4



The standard electrode potential for the couple is denoted as E^0 and is equal to +0.77 V and +0.79 V respectively. The Nernst equation can be related to the reference electrode by considering the electrochemical equilibria:

3-5



Combining this with the Nernst equation gives:

3-6

$$E = E^0 - \frac{RT}{nF} \ln \left(\frac{[H^+]}{P_{H_2}^{\frac{1}{2}}} \right)$$

3.2.1.2. Counter Electrode

To ensure the potential of the reference electrode stays constant, a counter electrode is used to pass the current and allow no current flow between the working and reference electrodes. Typically, Pt mesh is employed as the counter electrode because of its inert and noble nature. The counter electrode must also be large enough to support the current generated at the working electrode. By using Pt mesh in this work rather than a coil, a sufficiently large surface area was ensured to guarantee the current produced was accounted for.

3.2.1.3. Electrolyte

The supporting electrolyte must be of high enough concentrations to allow a distance between the solution species and the electrode of 10–20 Å. This is to provide a small enough potential drop for typical electrochemical rate constants to be used.¹³⁹ The

working electrolyte used in this work is 0.1 M H₂SO₄. Although there has typically been a move to HClO₄ of late, due to the adsorption of sulfonic groups onto Pt; however, palladium, the primary focus of this study, does not suffer from this issue, and according to Pourbaix it dissolves more rapidly in the presence of chlorine.⁵⁹ The temperature of the electrolyte was kept at 25°C, by using a water bath for consistency of measurements.

3.2.1.4. Working Electrode

The experimental outcome is the result of the potential changes at the working electrode and during the experiment, the potentiostat constantly either controls or measures the polarisation (the potential difference between the reference electrode and the working electrode) of it.

For consistency, all experiments in this work were completed on the same working electrode, a rotating disc electrode as can be seen in Figure 12 above. This is made from PTFE holder, a material used due to its high resistance to solvents, acids and bases, which allows its use in most electrolytes, it is also non-conductive and so protects against contact with live components, and, finally, is thermally stable at 25°C. The disk material is glassy carbon (GC) with a diameter of 5 mm. The surface characteristics of this material may change over time and so the electrode must be well prepared before each experiment to ensure consistency between results. Glassy carbon is used as a working electrode material as it is impermeable to gas, resistant to chemical attack and electrically conductive.¹⁴⁰ It also works well in the potential window utilised in this work. The RDE tip had an internal thread, which matched the thread on the shaft attached to the rotator to ensure maximum contact. For consistency

of measurements, the tip was always placed approximately 10 mm below the surface of the electrolyte.

3.2.1.4.1. Working electrode preparation

Many different methods for GC electrode preparation exist and indeed seem to vary between research groups. The polishing method used in this work was kept consistent throughout and a mirror finish was achieved each time before use. The GC tip was washed with ultrapure water before polishing. Microcloths were used for successively polishing by hand 100 times in a figure of eight pattern, with 1 μm , 0.3 μm and 0.05 μm alumina slurries. The tip was then rinsed and placed in an ultrasonic bath for 2 minutes to ensure the removal of residual alumina particles.

3.2.1.4.2. *Ex-situ* catalyst inks

To prepare a catalyst powder for study it must be prepared into solution to allow application onto the electrode to form a homogeneous layer. To achieve this the catalyst is weighed out to less than 10 μg , next ultrapure water is added followed by IPA. The initial addition of water wets the catalyst and prevents the catalyst oxidising the IPA to acetone. Finally, Nafion is added as a binder and the solution is placed in a ultrasonic bath for one hour, ensuring the temperature stays constant. The amounts of ultrapure water, IPA and Nafion are added in the correct amounts to achieve a solution of 80% water, 19.8% IPA and 0.2% Nafion. The catalyst ink is then drop cast onto the electrode before testing in the electrochemical cell. Drop casting involves using a precise pipette to apply a droplet of ink to the electrode surface and leaving to dry, due to the difference in surface features between the electrode and surrounding PTFE, the droplet only adheres to the electrode and does not encroach onto the PTFE. To

produce a homogeneous film on the electrode many different methods are quoted in literature, for this work the same method was used throughout for consistency. Depending on the test procedure, either one or three 10 μL drops were applied to the prepared disk, in between the droplet applications the electrode was placed in the oven at 80 °C and dried thoroughly. This method was also used as a standard operating procedure at Amalyst, which allowed comparison between results taken there. The loading of the catalyst on the electrode may be calculated by:

3-7

$$\text{Metal Loading}(\mu\text{g cm}^{-2}) = \frac{\text{Volume}_{\text{deposited}}(\mu\text{l}) \times \text{Density}_{\text{ink}}\left(\frac{\mu\text{g}}{\mu\text{l}}\right)}{\text{Area of electrode (cm}^2\text{)}}$$

3.2.1.5. Potentiostat

The potentiostat used throughout this work to design and perform experiments was a 320N Autolab with Nova software. The potentiostat induces a fixed potential between the working and reference electrode. Though negligible current is drawn through the reference electrode so that the Equation below holds:

3-8

$$E = E_{\text{working}} - E_{\text{reference}}$$

In doing this, when E alters by 1 V, E_{working} also does. The potentiostat measures current flow when a potential drop is imposed at the working electrode. The counter electrode passes the current induced from the working electrode and so the potentiostat sets the voltage for the counter electrode to allow this. The counter electrode must be used for this, as if a two-electrode cell were to be used, both the resistance of the solution between the working and reference electrodes and the

potential chemical change from high currents of the reference electrode would alter the results. As the current will change the chemistry of the electrode, this can result in contamination of the electrolyte. In voltammetry, this potential issue is reduced due to the very small amount of material being studied, though in larger systems the counter electrode may be moved into a separate compartment of the cell to prevent this contamination. When designing experiments, the maximum voltage deliverable by the potentiostat must be considered as if exceeded the results produced will not be reliable. The potentiostat in this work was housed in a Faraday cage, consisting of a metal frame and wire mesh to reduce electrical noise in the experimental results.

3.2.2. Cyclic Voltammetry

Cyclic voltammetry is the base electrochemical method in which other tests are based such as surface 'cleaning' and degradation testing. The technique can highlight the electrochemical reactions a catalyst is capable of facilitating. Within the electrochemical cell, the potentiostat applies a potential to the working electrode and the current response is measured. A cyclic voltammogram (CV) is produced when the potential is cycled between two points, for example from 0.05 V to 1.6 V and back from 1.6 V to 0.05 V and the data points are plotted as current vs. potential as in Figure 13. The initial CV begins at a potential which is featureless e.g. the catalyst is not likely to react electrochemically at that potential, in this work all CVs were initiated at 0.5 V.

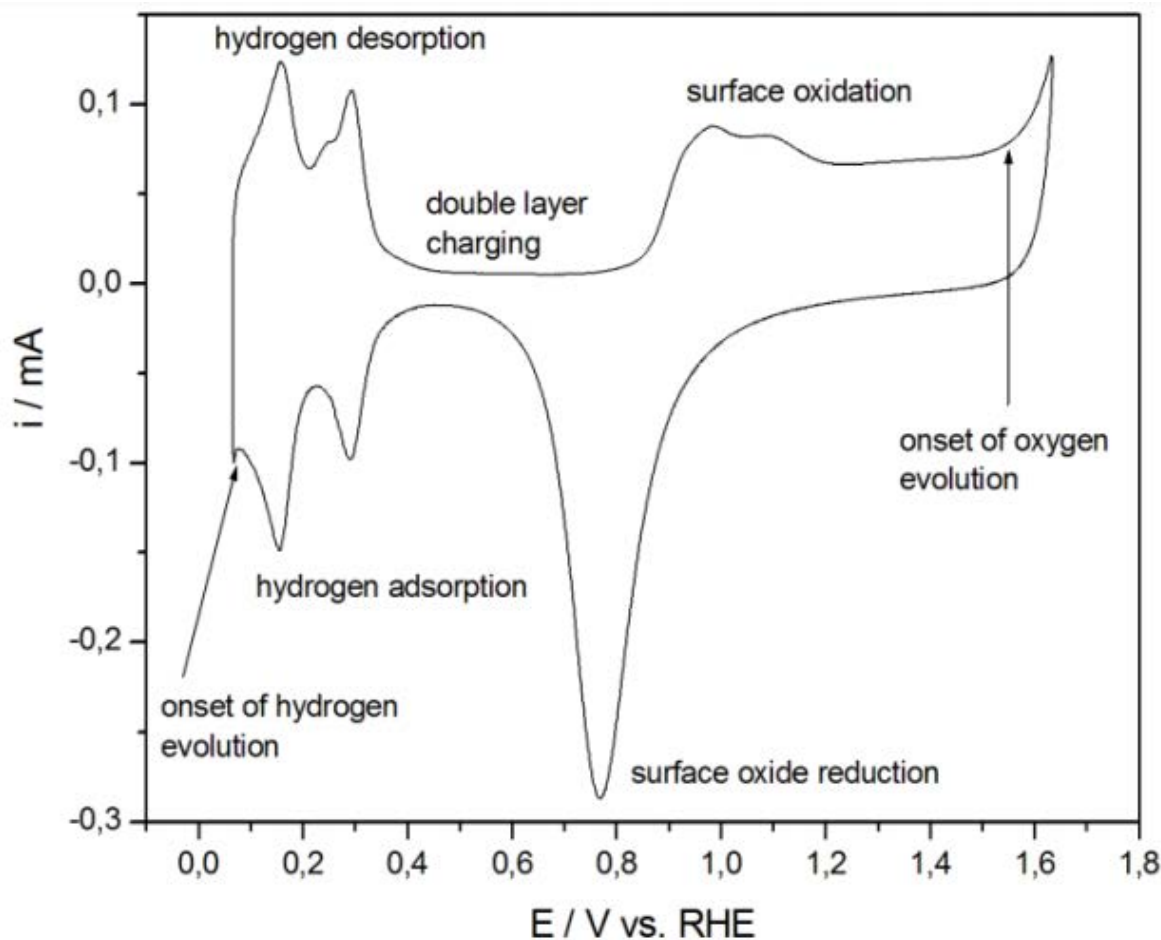


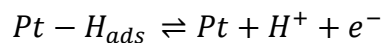
Figure 13 - CV indicating the different reactions occurring at a polycrystalline Pt electrode with cycling potential between 0.05 V and 1.6 V at a scan rate of 0.1 V s⁻¹. Reprinted with permission from Reprinted from *Electrochemical Methods of Real Surface Area Determination of Nobel Metal Electrodes*, Łukaszewski M. *et al.*, 11, 2016, 4442-4469.¹⁴¹

3.2.3. Electrochemical Surface Area

Catalyst utilisation and the electrochemical surface area (ECSA) are the two most commonly measured metrics to determine a catalysts ability. The ECSA measurement provides a quantification of the triple phase boundary area. The most common method of measuring ECSA is analysing the hydrogen adsorption and desorption regions. This method is highly applicable for the most common PEMFC catalyst, Pt, as it has a ΔG_H value of around 0 kJ mol⁻¹, meaning the hydrogen in the electrolyte will adsorb and

desorb readily. Additionally, Pt does not undergo any other reactions within this potential range and so this experiment can provide a fairly accurate result.

3-9



By running a CV between two set potentials, the ECSA can be found as can be seen in Figure 13. The forward reaction (between 0.05 V and 0.4 V) shows the desorption of hydrogen from the Pt catalyst layer. Where the reverse (between 0.4 V and 0.05 V) is the hydrogen adsorbing onto the Pt surface, the charge density measured here can be used to calculate the total area using the Equation:

3-10

$$ECSA = \frac{100 \cdot Q_H}{\Gamma \cdot L}$$

Where Q_H is the charge density, L is the mass of Pt and Γ the electrical charge associated with a monolayer of adsorbed hydrogen on the catalyst surface (mg). This Γ value is typically chosen to be $210 \mu C \text{ cm}^{-2}$, as this is correct for a Pt 111 crystallographic surface. Though for a Pt catalyst this is the most common, it still varies widely for different orientations. This number is often quoted across many Pt catalysts including Pt alloys and even for catalysts which do not contain Pt at all and so although the ECSA is a helpful tool to compare catalysts, it can provide results with high error due to this assumption. The area under the hydrogen desorption peak, which provides the charge density (Q_H) can also lead to miscalculations as there are a number of ways in which this area may be measured. The most common is to measure from the potential in which the hydrogen peak increases above zero to the potential at which this peak finishes, though this finishing point can often be difficult to distinguish. The

ECSA calculation method in this work was the same for both catalysts, to provide some measure of catalyst degradation over AST's, though as described the method contains assumptions and therefore does not provide true ECSA values. ECSA is discussed further in the Chapter studying hydrogen oxidation reaction catalysts.

3.2.4. Degradation

The degradation of a catalyst may also be analysed through *ex-situ* testing, again in much shorter time periods than *in-situ* measurements. Accelerated Stress Tests (ASTs) can be performed both *in* and *ex-situ* and provide information on how the catalyst may degrade in real time within a fuel cell by cycling the catalysts through aggressive potentials. Many ASTs have been reported for the testing of ORR catalysts, as these are the most commonly studied catalysts.¹⁴² However, the ASTs for HOR catalysts should be different, as it has been shown that the potentials the catalyst will be subjected to in their lifetime in the anode is different to those ORR catalysts see in the cathode. Hinds *et al.* used reference electrodes placed throughout the single cell on both anode and cathode to show the potentials at the electrodes on start-up, which is the period the largest potential fluctuations are expected.¹³⁷

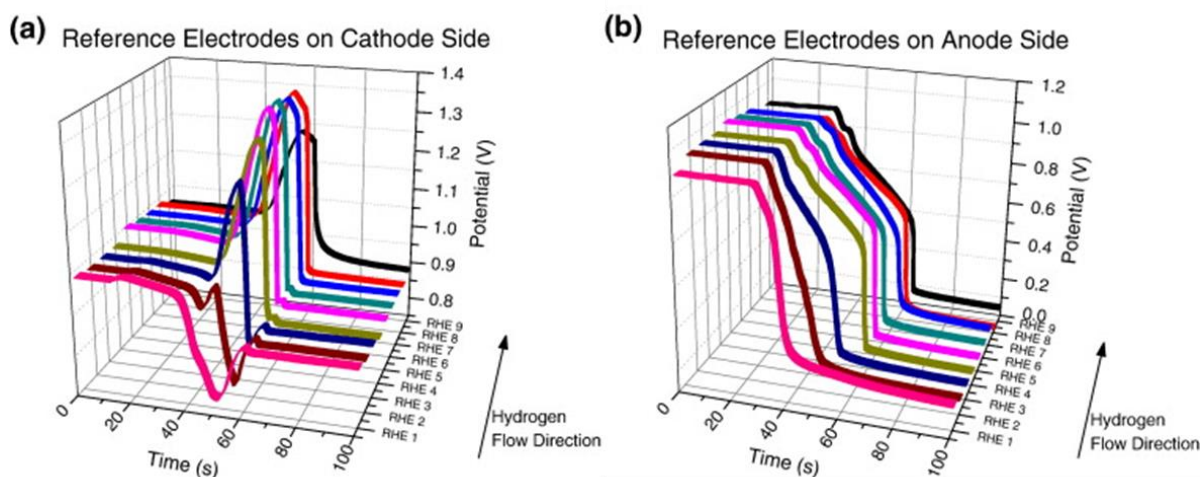


Figure 14 - Recorded potentials at the cathode (a) and anode (b) of the fuel cell at start up where RHE1 is the reference electrode closest to the fuel inlet. Reprinted from *Electrochemistry Communications*, 17, G. Hinds and E. Brightman, In situ mapping of electrode potential in a PEM fuel cell, 26-29, 2012, with permission from Elsevier.¹³⁷

AST cycles for an ORR catalyst are often in the range 1–1.6 V, however, as can be seen in Figure 14 the anode even at start-up will not experience these potentials. Therefore, the ASTs performed were in the range 0.05–1.0 V as this is applicable for a HOR catalyst. These were performed in a nitrogen saturated electrolyte by performing 1000 potential cycles between 0.05 V and 1.0 V at a voltage scan rate of 50 mV s⁻¹. After 20, 100, 500 and 1000 AST cycles, the ECSA was measured under a nitrogen saturated electrolyte, while potential cycling between 0.05 V and 1.0 V at a voltage scan rate of 20 mV s⁻¹.

3.3. Imaging

The imaging techniques, their scientific basis and background, used in this work are outlined below, many of these techniques were specifically chosen for their ability to image nanoparticles.

3.3.1. Scanning Electron Microscopy

Scanning Electron Microscopy (SEM) is a technique used for detailed surface study of a specimen by utilising a focused beam of electrons. SEMs may consist of different components, though most, including the ZEISS EVO10 used in this work had the following parts: electron optical column (electron source, electron gun, lenses, detectors), vacuum system, electronics and software.

The energetic electrons from the source travel down the column onto a series of lenses, which focus the beam into a point of around 1 nm in diameter onto the surface of the sample. This beam is then scanned across the specimen at low accelerating voltages, as the beam does not need to penetrate the surface of the specimen. The detectors then subsequently capture the resulting secondary electrons emitted from the specimen and the details are stored. The variations in brightness are used to present the data in an image with bright edges and dark recesses, while the magnification shows the difference between size of the presented image and the area scanned.

3.3.2. Transmission Electron Microscopy

Transmission Electron Microscopy (TEM) is a technique used for analysing a whole specimen rather than just the surface. Similar to SEM typical TEMs will consist of an electron optical column, vacuum system, electronics and software. Though the specimen used must be thin enough to allow the electron beam to pass through the sample (at high accelerating voltages), where transmitting electrons are produced and then projected onto the viewing device at the bottom of the column. The resulting image

is grayscale; this contrast is produced by the thickness of the sample or the density of different elements.

Scanning Transmission Electron Microscopy (STEM) combines SEM with TEM and allows the analysis of other signals which, cannot be accessed by TEM, for example EDX and HAADF. As with SEM, the beam of electrons is finely focused and scans across the specimen in a raster pattern. STEMs main benefit is its improvement of spatial resolution compared with SEM alone. The STEM presented in this work was completed on a JEOL 2100 FEGTEM. Field Emission (FE) microscopes use an electron probe, which is more stable and brighter than conventional guns which allows sensitive analysis at nanometre scale. FE imaging also provides illumination with a narrow energy spread which improves the final high-resolution image. Scattered beam electrons, which can be detected by STEM, come from beam electrons which have been elastically scattered by the nuclei of specimen atoms, those scattered through a large angle are detected by a high angle annular dark field detector (HAADF). In these images, heavier atoms are observed to be brighter. The resulting TEM or HAADF images can be used to measure particle sizes, this is commonly completed in ImageJ software. For very clear images with higher resolution and contrast against the background the automatic particle sizing technique can be used. ImageJ is the most commonly used image analysis program across biological and physical sciences, due to ease of use and access.¹⁴³ ImageJ analysis begins with conversion of a grayscale TEM image into a black and white image, known as thresholding. The program then identifies the edges or outlines of the particles in the black and white image, which provides a 2D projection with particle area, aspect ratio and orientation. This technique is greatly limited by nanoparticle aggregation and agglomeration, which is highly likely

in a majority of samples, particularly when beginning to produce a new catalyst and the synthesis method has not been developed to optimum standards. Agglomerated or aggregated particles are not distinguished and will either present as one large particle or its outline will not be present at all.

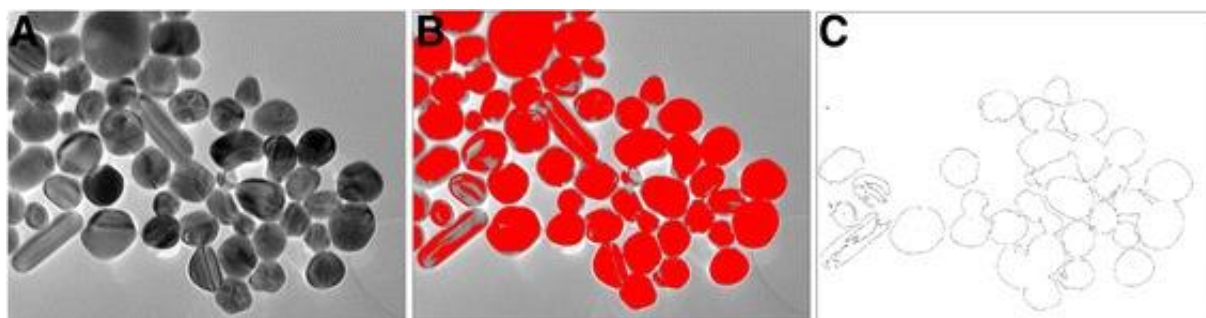


Figure 15 - Figure showing the limitations of ImageJ thresholding software, A) is the original TEM image of silver nanoparticles with clearly defined aggregated nanoparticles, B) is the same image, optimised in ImageJ software to distinguish background from particles and C) image produced after optimal thresholding, which does not show all nanoparticles present nor distinguish the individual particles. Reproduced from Nanoscale Research Letter, 11, M. Vippola, M. Valkonen, E. Sarlin, M. Honkanen and H. Huttunen, 169, 2016 an open access publication.¹⁴³

3.3.3. Energy Dispersive X-ray spectroscopy

Both SEM and STEM allow the use of energy dispersive X-ray spectroscopy (EDX) which provides chemical analysis of the specimen under review. Both STEM and SEM used in this work were equipped with Oxford Instruments EDX and INCA software was used to analyse results. The instrument detects X-rays, which are emitted by atoms in the specimen when the electron beam hits them. These characteristic X-rays are produced when the electron beam removes an electron from the inner most shell of the atom, creating a hole, which is then filled by an electron from an outer shell. This electron movement creates a characteristic photon (X-ray) which is then detected. The relative amounts of each element can be detected by counting the number of photons emitted. In this work, EDX was used in a line with the SEM and to produce a map with

the STEM, which allowed confirmation of the expected elemental framework of specimens.

3.3.4. X-Ray Fluorescence

X-ray fluorescence (XRF) is a non-destructive method, which may also be used to determine the elemental framework of a specimen. Rather than an electron beam, high energy X-rays are used to excite a specimen. A typical XRF will consist of an X-ray source, detector, electronics and software. XRF uses the same principles as EDX with the X-rays analysed being those that are emitted by the movement of the electron into the lower shell. The difference between the two techniques is use of an electron or X-ray beam for the initial excitation. XRF can also be used in mapping of elements to get an overall image of how the specimens are made up. This technique can be used quantitatively though this can be restrictive depending on the sample size. The XRF machine used in this work was a Bruker μ -XRF M4 Tornado.

3.3.5. X-Ray Computational Tomography

X-ray computational tomography (CT) allows non-destructive high-resolution visualisation of the structural properties of materials. The technique came from the medical sector which was transformed by its use and its creator Godfrey Hounsfield received the 1979 Nobel Prize for it.¹⁴⁴ Tomography is the analysis of numerous transmission radiographic projections taken of a sample at different angles. To obtain a tomograph, a sample is rotated in the field of an X-ray beam, and the incident X-rays are measured by a charge-coupled camera, which analyses the varying attenuation of the X-rays between different materials. This produces grayscale values which are treated with mathematical transforms from algorithms to produce two dimensional

images or 'ortho-slices'. These slices can then be stacked into a three-dimensional volume to identify key features and allow analysis of areas of interest in the sample. The reconstructed volume is composed of voxels (volumetric pixel) and allows complete visualisation of the sample.¹⁴⁵ The X-ray CT used in this work was a lab-based Zeiss Xradia Versa 520, with reconstruction completed via performed via cone-beam filtered-back projection algorithms using commercial software Reconstructor Scout-and-Scan, Zeiss, and visualisation achieved using Avizo Fire 9.4 software. Often this technique has been performed using synchrotron radiation though the improvement in resolution has allowed lab-based CT to provide nano-scale results with much simpler access.

3.3.6. Atomic Force Microscopy

Atomic Force Microscopy (AFM) allows structural characterisation by measuring the force created by dragging a cantilever over the surface of a specimen in a raster pattern. This can give atomic resolution and provides a three-dimensional image of the surface with information such as height, magnetism, friction and electrochemical properties. The AFM used in this work was a Bruker Dimension Icon, which uses temperature compensating position sensors to overcome noise in all axis, therefore providing better resolution. Gwyddion software was used to analyse the resulting images. The cantilever probe has a sharp pyramid shaped tip whose end has a nanometre-sized radius, helping provide the nm scale resolution. However, due to drift in the measurement as the cantilever moves across the surface, the vertical resolution is superior to the lateral. The interaction between the specimen and the tip is measured by the displacement of the tip, which is performed by bouncing a beam off the lever into a photodetector. The use of tapping mode has allowed improvement of the lateral

measurements, reducing the lateral force by allowing the tip to contact with the surface for a short time, enabled by oscillating the cantilever by tens of nm.

3.4. Characterisation

3.4.1. X-ray Diffraction

The use of X-ray Diffraction (XRD) provides the study of crystalline materials giving further information than that obtained from absorption techniques already mentioned. The XRD used in this work was a Bruker D8 Advance, which provides rapid, high-resolution data. A typical XRD instrument consists of an X-Ray tube, sample holder and detector. The technique uses the interaction of interference of X-rays produced from the tube with the crystalline sample. Constructive interference occurs when Braggs Law is satisfied:

3-11

$$n\lambda = 2d \sin \theta$$

Where n is the order of reflection, λ is the wavelength of the X-ray, d the spacing between the diffraction planes of the crystal and θ the angle of incidence. Due to the random orientation of the powder sample, the specimen should be scanned through a variety of 2θ angles, to obtain the different diffraction directions of the crystal. Small structures are difficult to measure via XRD, where nanoparticles or trace particles may go undetected and therefore provide incomplete or skewed results.

3.4.2. Inductively Coupled Plasma-Mass Spectrometry

Inductively coupled plasma mass spectrometry (ICP-MS) may be used to quantify elements in a specimen. ICP-Atomic Emission Spectroscopy (ICP-AES) may also be

used, ICP-MS has superior detection capabilities. The technique uses high temperature ICP source to decompose the specimen first into its elements and then into ions. This method requires precision in the sample preparation process as any errors here will directly affect the results. Samples must be in liquid form and solid samples may be analysed by digestion with an aggressive acid matrix. To reduce the interferences and drifts in the instrument the equipment will be run with calibration standards, which are applicable for the elements present in the sample. The ICP-MS used within this work was an Agilent 7500ce which can measure trace amounts of elements below fluorine to ppb-ppt levels. This system is also mounted with an auto diluting system to further reduce sample matrix effects. Phosphorous is difficult to detect with ICP-MS as the high silicon matrix used leads to polyatomic silicon which interferes with the measurement of $^{31}\text{P}^+$, the only isotope of P.

3.4.3. Thermogravimetric Analysis

Thermogravimetric analysis (TGA) is used to measure the effects of temperature increase over time on the mass of a specimen; this is known as dynamic TGA. Typical TGAs consist of a thermobalance (electronic microbalance, furnace, temperature programmer and recorder) which is under atmospheric control to allow the use of different gases to study specimens under different reactions, such as oxidation or reduction. Typically, the temperature range will be set above the decomposition temperature of the specimen, the reaction will be monitored, and the TGA curve studied.

3.5. *In-situ* Testing

Membrane Electrode Assemblies (MEAs) were produced to enable testing of the catalysts *in-situ* in the form of a single cell. This was performed in a Scribner 850e Fuel Cell Test Station, equipped with humidifiers to allow relative humidity (RH%) control of the input gases, a back-pressure system for controlling the pressure of the gases and a potentiostat to enable electrochemical measurements to be taken within the cell. Although *ex-situ* testing for the performance and degradation of a catalyst can be invaluable and less time consuming, *in-situ* testing is required as the performance of the catalyst within a fuel cell may be completely different from *ex-situ* results. Factors at play here can include; the humidity, temperature, water flows and also interactions between the catalyst and other materials within the fuel cell. The main difference to the catalyst performance though is the electrolyte, which in *ex-situ* is liquid and in the case of *in-situ* testing, the catalyst would not be completely wetted and would instead contend with the TPB. Further differences can come from the loadings of catalyst, which, for *in-situ* tests are around 10 times that of *ex-situ* tests, which will alter the kinetics within the layer.

3.5.1. Properties of MEA components

The Sigracet GDL 35 BC included a 5 % impregnation of PTFE and contained a mesoporous layer (MPL). The addition of PTFE reduces the porosity (likely due to blockage of pores) and resistivity of the GDL but increases the permeability, hydrophobicity. The MPL by definition has a lower porosity and so this also contributes to the GDLs reduced porosity. The addition of the MPL can also increase the GDLs roughness which can provide a higher water evaporation and is therefore is more likely

to prevent flooding.¹⁴⁶ El-Kharouf *et al.* showed that the GDL 35 BC had one of the highest surface roughness values when compared to other commercial GDEs.¹⁴⁷ The GDE used as a standard in this work was chosen because its base is the same Sigracet GDL 35 BC, with a consistent application of 0.4 mg cm⁻² of Pt catalyst applied. The equivalent weight (mass of polymer which corresponds to one mole of reactive side chain groups) of Nafion 212 is 1100 g eq⁻¹ and its thickness is 50.8 µm.

3.5.1.1.1. *In-situ* catalyst inks 80%

Similar to *ex-situ* testing a catalyst powder must be prepared for study by producing an ink from the powder to allow application onto the electrode to form a homogeneous layer. As the GDE has been cut to an area of 5.3 cm² the catalyst is weighed out to achieve a catalyst loading of 0.1 mg cm⁻². This loading is for the metal only and the weight of carbon must be taken into consideration, where the catalyst powder is 40 wt% metal and 60 wt% carbon support.

3-12

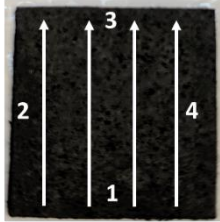
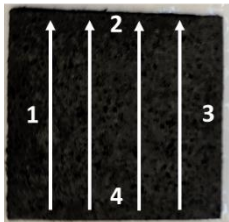
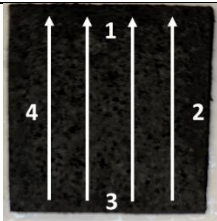
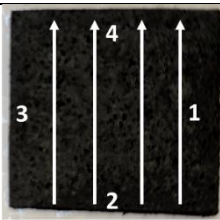
$$Metal\ content\ (\mu g) = 0.4(catalyst\ powder(\mu g))$$

To achieve this the catalyst powder is weighed out to less than 10 µg, next ultrapure water is added followed by IPA. The initial addition of water wets the catalyst and prevents the catalyst oxidising the IPA to acetone. Finally, Nafion is added as a binder and the solution is sonicated for one hour, ensuring the temperature stays constant. The amounts of ultrapure water, IPA and Nafion are added in the correct amounts to achieve a solution of 80% water, 19.8% IPA and 0.2% Nafion. A scalpel is used to precisely cut each GDE into a square of 2.3 × 2.3 cm to obtain an MEA active area of 5.29 cm² and the membrane to a square of 5 × 5 cm for an area of 25 cm². This larger

area of the membrane allows it to sit between the gasket in the fuel cell set up and prevent crossover which may occur if a smaller area was used.

This ink is applied to the GDL to produce a GDE, numerous deposition methods exist and requires consideration due to its impact on the TPB and overall catalyst performance. The simplest method is to apply a thick ink using a lab spatula to the GDL, though this produces inhomogeneous thick layers which are difficult to reproduce consistently and are therefore not a good option for comparison of catalyst inks. An evolution of this method is to use a similar thick ink and apply using a blade which has a consistent edge and set a certain distance above the GDL. This provides a more homogeneous thickness though pressing is required to ensure a mechanical stability of the layer.¹⁴⁸ Automated spraying is another common technique used in research labs to apply this ink layer, as it is a well performing method, producing homogeneous thin layers. The issues with this method are practical, set up times are long and with the highest risk of the application methods due to highest spread of particles into the air and surroundings, this also leads to loss of ink. There are benefits and negatives to all application techniques with different labs utilising different methods, to achieve results which are able to be compared the same application method must be used throughout. For this work, all MEA's were produced by painting the CL onto the GDL. This method provides homogeneous application and lower loss of ink compared to spraying, though its drawback is the length of time taken due to drying periods. Initially the GDL is weighed followed by application of painted layers of the prepared catalyst ink. The painting technique steps are presented in the Table below:

Table 5 - Painting steps used in the application of the CL onto the GDL in MEA preparation.

Step 1: Paint from edge 1 to edge 3 in four consistent strokes, leave until visibly dry and rotate 90 degrees.	
Step 2: Paint from edge 4 to edge 2 in four consistent strokes, leave until visibly dry and rotate 90 degrees.	
Step 3: Paint from edge 3 to edge 1 in four consistent strokes, leave until visibly dry and rotate 90 degrees.	
Step 2: Paint from edge 2 to edge 4 in four consistent strokes, leave until visibly dry and rotate 90 degrees.	

The steps above are continued until the desired amount of CL is applied, which is verified by the dried weight of CL applied to the MEA. The weight is measured again 24 hours after preparation to ensure the correct weight of catalyst was applied, to ensure the MEA is completely dry.

3.5.2. Hot Pressing

The anode GDE and cathode GDL are sandwiched together with the Nafion 212 membrane in between, as in Figure 16, a small a is written in the bottom left corner of

the membrane on the side of the anode GDE to help identify this when placing into the single cell test stand.

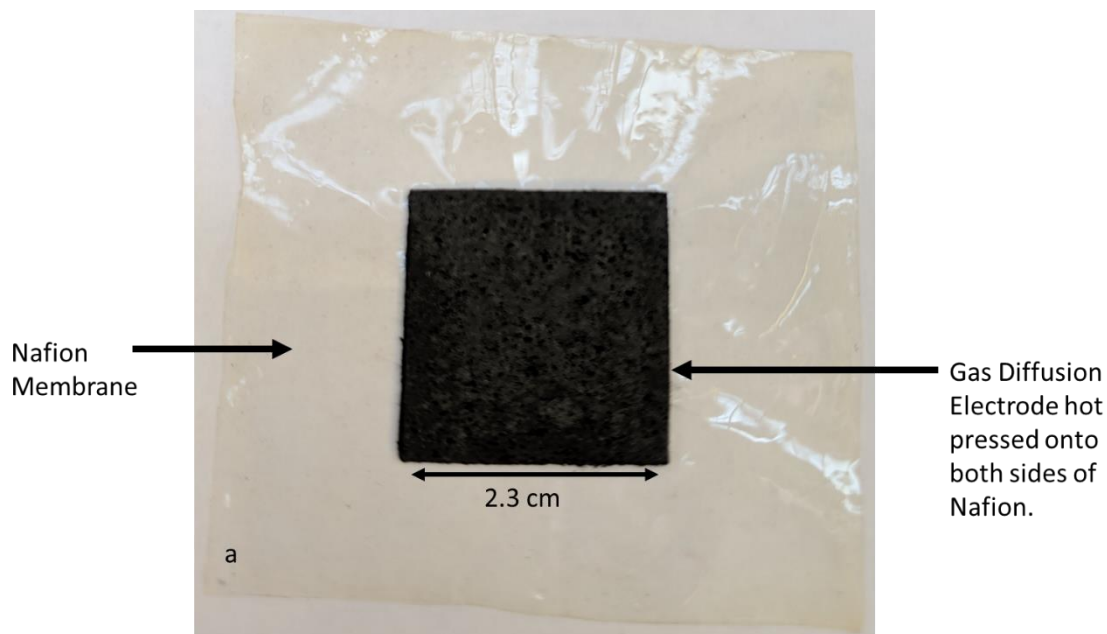


Figure 16 - Image of MEA with anode GDE and Nafion membrane visible, some delamination and pin pricks can be seen in GDE due to poor MEA hot press technique.

As with many aspects of laboratory work, the specific method of hot pressing is not typically included in a publication and each laboratory will typically have their own method which works best with the type of hot press used. The standard operating procedure (SOP) for the hot press was used initially, but inconsistencies in the outcome (from burnt to broken GDL) lead to improvements in this procedure and all MEAs used in this work were produced by this updated method.

Table 6 - Summary of previous and improved hot press method used for MEA production

	Previous Method	Current Method
Temperature	135–140 °C	130 °C
Time	2 mins	2 mins
Pressure	1 tonne	0.75 tonne
Protective layer	Aluminium foil	Tygaflor + aluminium foil

The aluminium foil used in the old method had the potential to stick to the GDL and often took part of the GDL away when removing the foil from the MEA. Meyer *et al.* previously showed that 130 °C produced optimum Nafion to electrode contact.¹⁴⁹ The addition of Tygaflor (a PTFE sheet providing anti stick properties) and the reduction of pressure reduced the likelihood of damaged MEAs in the hot pressing production stage. Once cooled down, the MEA is visually inspected for any damage or irregularity, which may affect the MEA performance. Once this verification is complete, the MEA may be tested in the test stand.

3.5.3. Single Cell Testing

The tests performed in this work followed the published EU testing procedure to give validation to results obtained and allow them to be compared with literature.⁷⁴ This protocol was produced by the EU in collaboration with the automotive sector and is aimed at standardising testing for fuel cell systems. The successful operation of a fuel cell is a function of degradation as well as performance. In this work, the MEA is tested in order to assess the catalysts ability to withstand degrading conditions. To achieve this a consistent load cycle is applied over time whilst measuring the voltage response to assess the MEAs endurance. The load cycle produced is from the test protocols suggested by the EU, which was derived from New European Driving Cycle (NEDC) adapted for FC vehicles. Vehicle components are typically tested according to drive cycles; these are different across the world and typically match the style of driving of the country it is applicable to. The NEDC, for example, has parts, which are typical for city driving followed by a section of motorway driving, whereas the US highway fuel economy-driving schedule (HWFET) is designed with less stopping time and has a higher average speed. As mentioned above single cell tests provide different results

to *ex-situ* testing, similarly, stack testing shows performance differences to single cell testing. Stack testing has a less controlled environment and more non-uniformities are present, as would be present in real life use of a fuel cell. The main non-uniformities in stack testing are cell voltages and these are often due to water and thermal management.¹⁵⁰

3.5.3.1. Test stand components

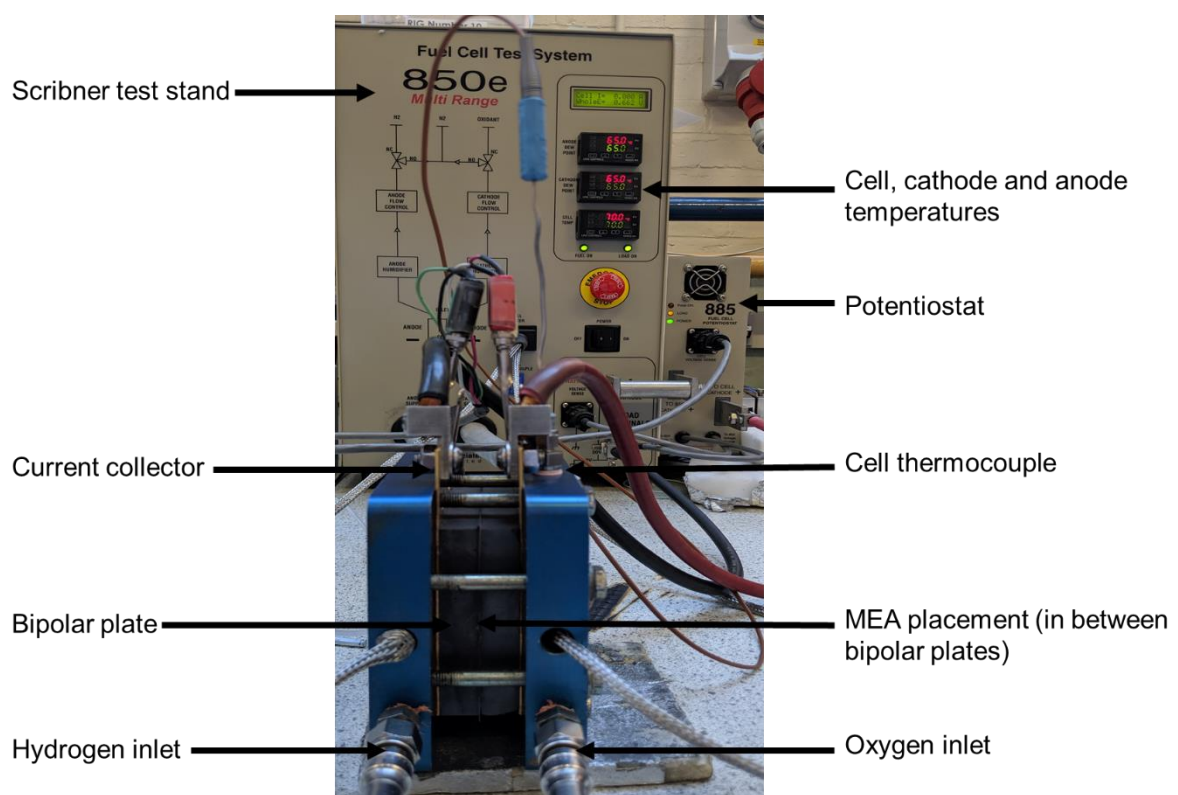


Figure 17 - Single cell test set up in forefront of image, with Scribner test stand in the background.

Figure 17 shows the setup of the single cell testing. The flow pattern of the bipolar plate is serpentine with an area of 5 cm². The gasket used and compression given by tightening the bolts in the setup is vitally important to the set up. Use of different GDE materials with different thicknesses will require different levels of compression and gasket thickness. Optimisation tests for this work dominated the overall time required

to perform tests. The final procedure included a Tygaflor gasket of 150 μm at both the anode and cathode with a torque of 5 Nm applied to each of the eight bolts holding the MEA in place. These bolts were tightened and untightened in the pattern indicated in each time to ensure evenly applied pressure.



Figure 18 - Pattern in which bolts are tightened on the Scribner single cell test rig in order to ensure even pressure across the MEA held inside.

3.5.3.2. Conditions

The standard temperature for all tests performed is 80 °C, as this is the most representative of the cell temperature found in automotive applications. The settings for each of these tests are set out in the Table below. The anode and cathode conditions are different, as they have been optimised for the gas they are supplying as fuel.

Table 7 - Test conditions at the anode and cathode of a fuel cell

	Anode	Cathode
Fuel inlet temperature	85 °C	85 °C
Fuel inlet humidity	64 RH%	53 RH%
Fuel inlet pressure	250 kPa	230 kPa
Fuel composition	H ₂ 5.0 quality	ISO 8573-1:2010
Fuel stoichiometry	1.3	1.5

The inlet temperature for both hydrogen and oxygen was 5 °C above the operating temperature of the cell to prevent water condensation at the inlet of the cell, which can occur at the connections, which act as a cold spot. Insulating foam was also secured around the inlet before each experiment to aid temperature consistency. These were implemented after initial experiments showed large amounts of flooding due to the presence of water and it became apparent it was due to cold spots in the fuel cell system.

The inlet humidity of a fuel cell should consider the operation in a fuel cell vehicle; typically, the hydrogen would be recirculated providing a dry hydrogen, though during operation the water produced at the cathode will move back to the anode through the membrane. Therefore, the EU recommend a 50 % RH that is the equivalent of 64 °C when the cell temperature is 80 °C. The oxygen is typically uncontrolled as air intake from the surroundings provides it; therefore, it is difficult to state common RH values, and so 30% RH is used to simulate slightly dry conditions, which can be gained from 53 °C when the cell temperature is 80 °C. The quality of hydrogen used in testing is higher than that suggested by the ISO 14687-2:2012 standard for vehicles. This is due to the severely degrading effects some contaminants can have on MEAs and so to ensure fair testing a high purity 99.999% hydrogen is used. The oxygen should also be kept as free as possible of impurities and free from oil to protect the fuel cell catalyst

from poisoning. The stoichiometric value is the multiple of the theoretical flow required for complete consumption of the pure fuel, which will vary depending on the current drawn due to Faradays Law.

3.5.3.3. Standard Test Procedure

The Table below shows the main step and requirements of the EU testing procedure and how they were performed in this work, the details of each step are discussed in further detail in the following section.

Table 8 - Short description of standard EU procedure for MEA testing

Step in method	Reason	Details
Leak test	Initial test which MEA must pass to show it	Pressure of nitrogen gas increased followed by removal of gas, pressure is monitored to ensure limited drop in pressure.
Break in	Ensure MEA is sufficiently hydrated, highlighting any issues with prepared MEA.	Slow increase in current draw from MEA held for 1 hour followed by cycling between high and low voltage with current response measured.
Conditioning test	Ensures fully hydrated MEA to level at which further tests can be carried out	Current density set, held and monitored for fluctuations above 5 mV. Once steady MEA may be tested.
Polarisation curve	Standard MEA test to allow comparison between MEAs	Set procedure steps between 0 – 2 A/cm ² and back down to 0.
Load cycles	Accelerated stress test which is similar to real world conditions	Load cycle calculated from current density measured at 0.65 V. Single cycle contains 35 steps which are repeated as many times as possible.

Before the MEA is tested experimentally, it must be activated to ensure hydration of the membrane, to reduce resistance and improve the interaction between the membrane and catalyst layer, providing the TPB. This is standardised to provide an equal start point of all MEAs tested. At the operating conditions listed above the MEA

is put through a leak test, a cell break in and finally a cell conditioning before the initial polarisation curves are taken.

The leak test ensures there is no fuel leakage from the system or crossover of gasses within the MEA due to pinholes and is run at room temperature. Nitrogen flow is begun at both the anode and cathode, with an increased pressure to reference conditions. The nitrogen flow is removed, and the pressure drop measured for 10 minutes, with a pass criterion of less than 0.3 kPa per minute drop.

The break-in procedure has all conditions set to reference, but the pressure should be lower, at 150 kPa at the anode and 130 kPa at the cathode. The current density is increased by 100 mA cm^{-2} per minute up to 800 mA cm^{-2} , ensuring the voltage does not drop below 0.4 V. Once at the set current density the cell is left to stabilise for 6 hours. The voltage will steadily increase over this time as the membrane is hydrated. The current density is then increased to 1 A cm^{-2} and left for a further two hours. At the end of the two hours, a reference voltage is taken, before cycling up to 0.8 V for 5 mins followed by 0.4 V for 5 mins. This is repeated once with a final cycle up to 0.8 V before a second reference measurement is taken at 1 A cm^{-2} for 5 minutes. The acceptance results are a fluctuation of less than $\pm 5 \text{ mV}$ between the reference points 1 and 2. If this does not occur then the current density is held at 1 A cm^{-2} for a further hour and the break-in procedure repeated.

The cell conditioning procedure is then performed where all the reference conditions are set, and the voltage is monitored. Once this has not varied more than $\pm 5 \text{ mV}$ in an hour the MEA is ready to be tested.

The polarisation curve should be taken to a maximum of 0.4 V and no lower to prevent damage to the MEA, all polarisation curves performed had a caveat setting which would reverse the experiment if this value was reached. The current density is steadily increased up to a value of 2 A cm⁻² and then the polarisation curve is reversed as can be seen in Figure 19. Each of these steps are held for long enough to ensure the stabilisation of the voltage, for current densities up to 0.1 A cm⁻² this is 60 seconds and above is 120 seconds.

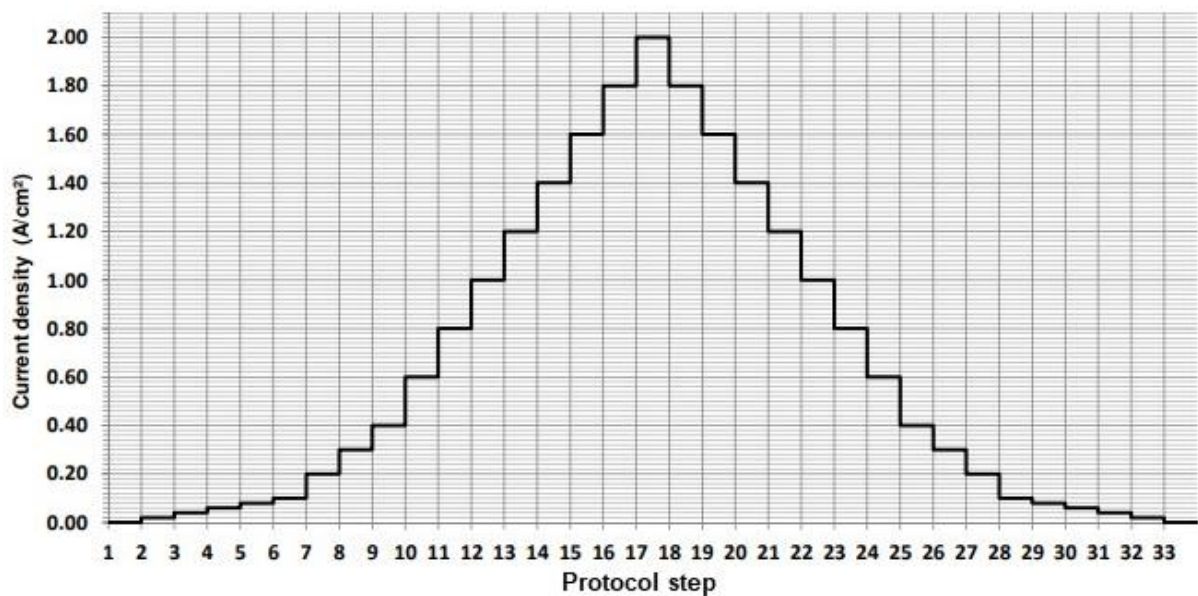


Figure 19 - Consecutive current density steps from the EU protocol for single cell testing of an MEA. Reprinted with permission from the EU Harmonised test protocols for PEMFC MEA testing in single cell configuration for automotive applications, JRC Science for Policy Report, Georgios Tsotridis *et al.*, 2015.⁷⁴

3.5.3.4. Degradation Testing

The load cycling to represent long-term use within a vehicle and the current density set values are produced from the load, which would be required for each point in the drive cycle. As this is a function of the load these values change each time, resulting in a time-consuming procedure to set up. The 100% load is the current density value at 0.65 V on the of the polarisation curve measured in the previous stage. Table 9 shows an example of these load percentages, which represent the different points in the NEDC drive cycle and their corresponding values when calculated from a polarisation curve.

Table 9 - Load test points

Step	Time (s)	Dwell (s)	Load (%)	Current Density (mA)
1	0	15	0.0	0.000
2	15	13	12.5	9.375
3	28	33	5.0	3.750
4	61	35	26.7	20.025
5	96	47	5.0	3.750
6	143	20	41.7	31.275
7	163	25	29.2	21.900
8	188	22	5.0	3.750
9	210	13	12.5	9.375
10	223	33	5.0	3.750
11	256	35	26.7	20.025
12	291	47	5.0	3.750
13	338	20	41.7	31.275
14	358	25	59.2	44.400
15	383	22	5.0	3.750
16	406	13	12.5	9.375
17	418	33	5.0	3.750
18	451	35	26.7	20.025
19	486	47	5.0	3.750
20	533	20	47.7	35.775
21	553	25	29.2	21.900
22	578	22	5.0	3.750
23	600	13	12.5	9.375
24	613	33	5.0	3.750
25	646	35	26.7	20.025
26	681	47	5.0	3.750
27	728	20	41.7	31.275
28	748	25	29.2	21.90
29	773	68	5.0	3.750
30	841	58	58.3	43.725
31	899	82	41.7	31.275
32	981	85	58.3	43.725
33	1066	50	83.3	62.475
34	1116	44	100.0	75.000
35	1160	21	0.0	0.000

Each single load cycle takes 1181 seconds, and 50 of these cycles is considered to be one test block.

4. TEST METHOD VALIDATION OF NAFION IONOMER ADDITION TO MEA

4.1. Motivation

Standard test procedures were optimised as part of this work, such as changing the hot pressing technique used to reduce likelihood of damage of the MEA in its production (detailed in Section 3.5.2.) and altering AST tests to create test conditions more suitable to the catalyst produced compared with standard tests used and presented in literature (detailed in Section 3.2.4.). This Chapter provides results which were obtained to analyse the addition of a Nafion layer to a commercial MEA which is a standard step in the MEA production procedure in the University of Birmingham laboratory. This Chapter highlights the many steps which must be undertaken when creating test procedures to produce results with high confidence.

The MEA construct stops an optimum contact between the catalyst layer and the membrane due to a restriction in the flexibility of the material preventing intimate contact; therefore, an ionomer is required to improve the triple phase boundary (TPB) between the electrolyte, catalyst particle and gas. Early MEAs were produced by using high loadings of Pt on PTFE and then hot pressing these to either side of a membrane.¹⁵¹ Following this, Nafion use as an ionomer to allow proton transport was initially applied as a separate solution layer over the top of the catalyst layer. By impregnating this layer with Nafion solution and successfully extending the TPB, and using Pt supported on carbon as catalyst, the metal loading was able to be reduced by tenfold whilst keeping the same level of performance.¹⁵² However further work showed this improvement still only provided around 20 % Pt utilisation.¹⁵³ In 1992 Wilson *et al.* used Nafion ionomer as a binder for the first time, showing its use as an addition to the

catalyst layer can allow this to be hot pressed straight onto the membrane, providing similar performances to the previous design but with substantially reduced Pt loadings ($0.15 \text{ mg}_{\text{Pt}} \text{ cm}^{-2}$).¹⁵⁴

Universities and companies often have working procedures that are not published and are passed from researcher to researcher internally. Often published works may be difficult to replicate due to the differences in working procedures, which can change the outcome of experiments. Such details as test conditions, sample preparation and test set-ups can significantly vary results obtained. Even in clinical environments where standardisation and harmonisation are paramount, with calibration and traceability highly focused on, results are often not consistent.¹⁵⁵ This Chapter focuses on one such working procedure which occurs in the sample MEA production. *In-situ* testing requires the sample production of an MEA, with one GDL coated in the catalyst of interest, the other a commercial GDE to ensure standard results, which will not impede the measurement process of the electrode of interest. Commonly a Johnson Matthey GDE is used as the commercial catalyst; it is difficult to obtain detailed information on the makeup of this GDE other than the type of GDL and the catalyst loading (typically $0.4 \text{ mg}_{\text{Pt}} \text{ cm}^{-2}$). The common procedure used in the University of Birmingham labs is to apply a layer of Nafion ionomer solution onto this commercial electrode before adding it to the Nafion membrane and GDE of interest to hot press and produce an MEA.¹⁵⁶¹⁵⁷ This production method was suggested in 1998 by Lee *et al.* who showed improved activities by the addition of Nafion onto a commercial GDE. However, commercial GDEs are continually being updated and improved and as with all experiments, before application within tests, the passed down method should be re-evaluated to ensure it

still provides the optimum results. This Chapter tests the current method used and assesses its viability.

4.1.1. Preparation

MEAs were produced using Johnson Matthey GDEs ELE0165 (GDL Sigracet SGL39BC with a catalyst layer of $0.4\text{mg}_{\text{Pt}}\text{ cm}^{-2}$) as both the anode and cathode, dry Nafion 212 (Dupont, USA) was used as the membrane without any pre-treatment. MEAs were prepared with two GDEs placed on either side of a Nafion membrane. The reference MEA used two GDEs with a Nafion membrane in between. The MEAs with additional Nafion ionomer were produced by painting a thin Nafion solution layer on top of the GDE (dry weight of Nafion 0.6 mg cm^{-2}) and left to dry. The Nafion solution was produced by diluting Nafion dispersion D1021 water based 1100 EW at 10 wt% (Ion Power, USA) in IPA and water. The MEAs were hot pressed for 3 minutes with an applied pressure of 400 psi at $130\text{ }^{\circ}\text{C}$.¹⁵⁸ Two of each MEA were produced, one for X-ray CT and SEM testing and one for *in-situ* testing.

4.1.2. SEM and Line EDX

The SEM images, Figure 20Figure 21, were taken of a cross section of the MEA, to show the GDL, CL and Nafion membrane. Both the MEA with extra Nafion and without were scanned in the same way. An EDX line scan (Figure 22) was run over both samples and the samples analysed for their fluorine content, utilising the technique benefit which allows spatial recognition of elements.

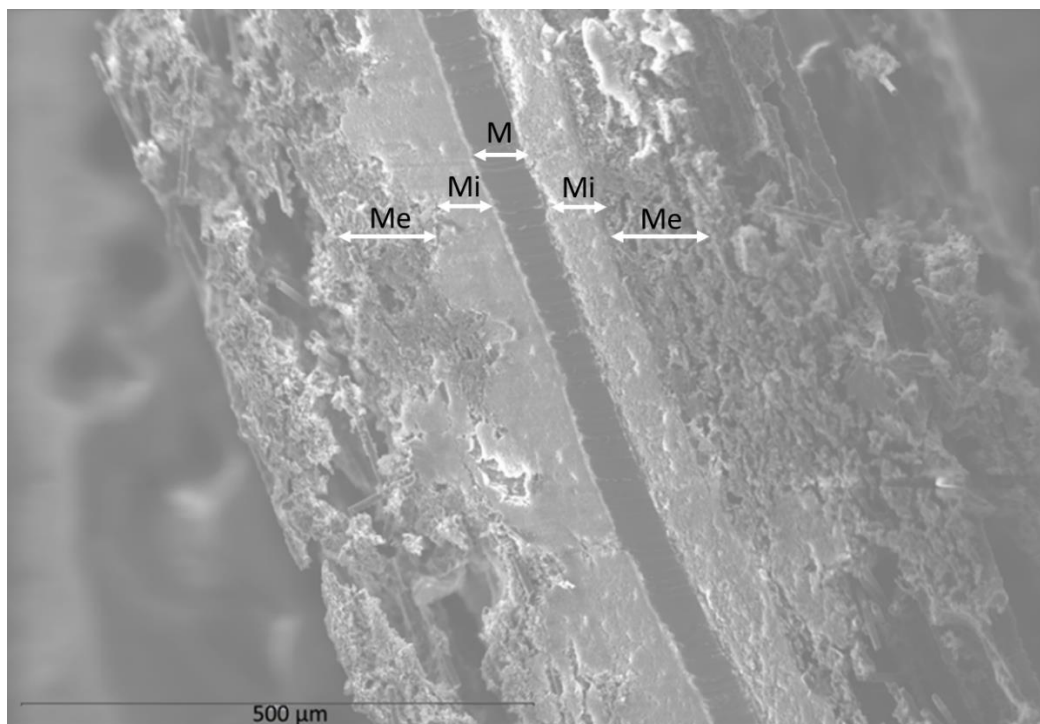


Figure 20 - SEM image of cross section of MEA containing the extra Nafion layer, with Nafion membrane visible running from top to bottom of image (M) surrounded by microporous CL (Mi) then the more porous mesoporous GDL (Me) on the outside of the image.

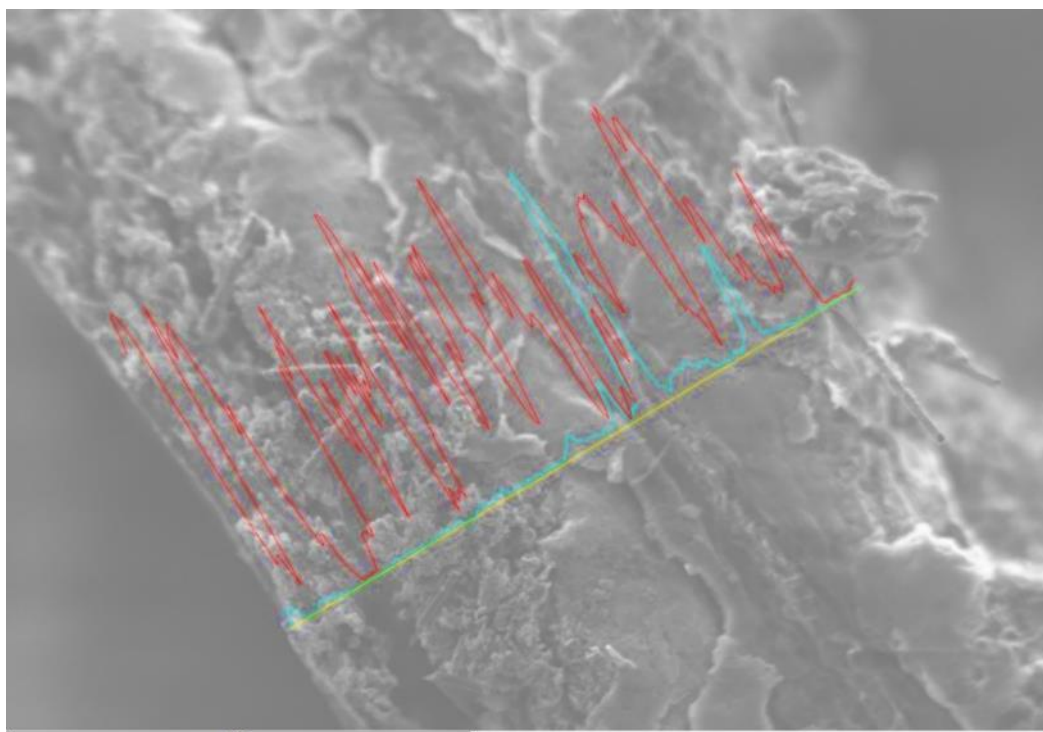


Figure 21 - SEM image cross section of MEA without the extra Nafion layer, including yellow line indication the area where the EDX line scan was taken with the F (blue) and C (red) EDX measurements imposed on the image.

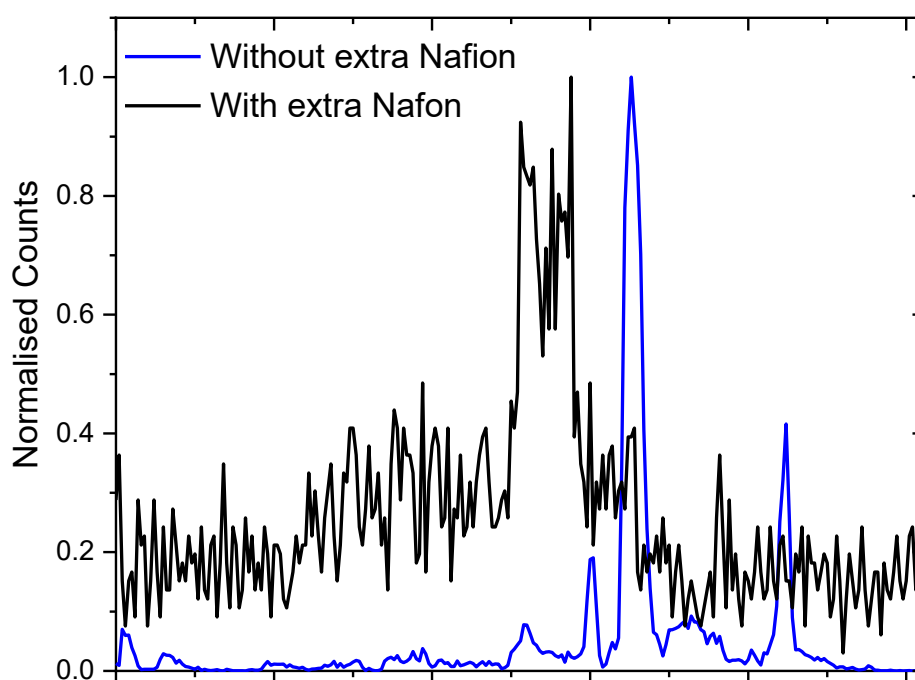


Figure 22 - EDX of fluorine levels in the two samples shown in the SEM images above, one with and one without extra Nafion applied.

The resulting fluorine EDX line scans are shown in Figure 22, the values were normalised to account for variable exposure times between the samples. The sample without extra Nafion has a very clear peak where the Nafion membrane is located in the sample and a low baseline suggesting a lower amount of fluorine in the rest of the sample. The line scan of the sample with extra Nafion supplied has not only a wider peak around the membrane but also a higher baseline suggesting a larger amount of F throughout the sample.

4.1.3. X-ray CT

X-ray computational tomography (CT) was performed using a lab-based Zeiss Xradia Versa 520 (Carl Zeiss XRM, Pleasanton, CA, USA).¹⁵⁹ The samples investigated were prepared by punching a 1 mm disc of the MEA which was subsequently mounted upon a pin. The scans were performed with an accelerating voltage of 80 kV and a beam

current of 87.5 μA resulting in a beam power of 7 W. All images were acquired using a 40 \times magnification objective to give a pixel resolution of 0.191 μm . In all cases, an exposure time of 20 s was used to provide sufficient quality in the radiographs with 3201 projections acquired in each scan. Reconstruction of the micro-CT radiographs was performed via cone-beam filtered-back projection algorithms using commercial software ('Reconstructor Scout-and-Scan', Zeiss, Carl Zeiss., CA, U.S.A.). Visualisation was achieved using Avizo Fire 9.4 software (Avizo, Thermo Fisher Scientific, Waltham, Massachusetts, U.S.).

4.1.3.1. Ortho Slices

A non-local means filter was applied to the radiographs to reduce the noise in the images and aid the segmentation of the image into the top and bottom catalyst layer. To ensure over-smoothing did not occur low filtering was initially applied and was increased to a point where the signal to noise ratio allowed for representative visualisation of the sample, this same level was applied to each radiograph to facilitate comparative examination. Each ortho-slice above shows two catalyst layers with a Nafion membrane separating them. The much starker contrast which can be seen in Figure 23 and Figure 24 between the outer part of the scan and the internal part (membrane and catalyst layer) made segmentation based on grayscale thresholding much easier. The ortho-slices produced of the MEAs after single cell testing (Figure 25 and 26) did not have this contrast and so the separation was not possible, though it can be seen that the catalyst layer did not change in thickness before and after scanning. If these MEAs had undergone longer cycling or ASTs, then we would expect to see a thinner catalyst layer in the after ortho-slices.¹⁶⁰

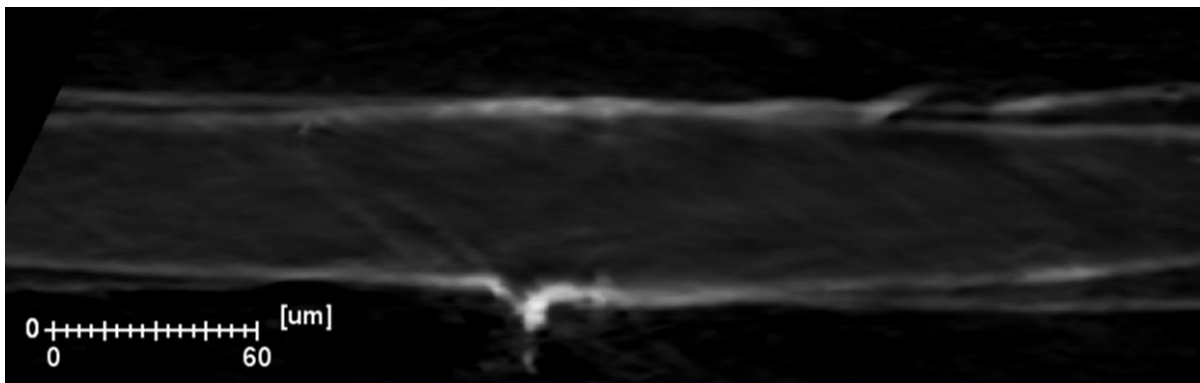


Figure 23 - Without Nafion before single cell testing

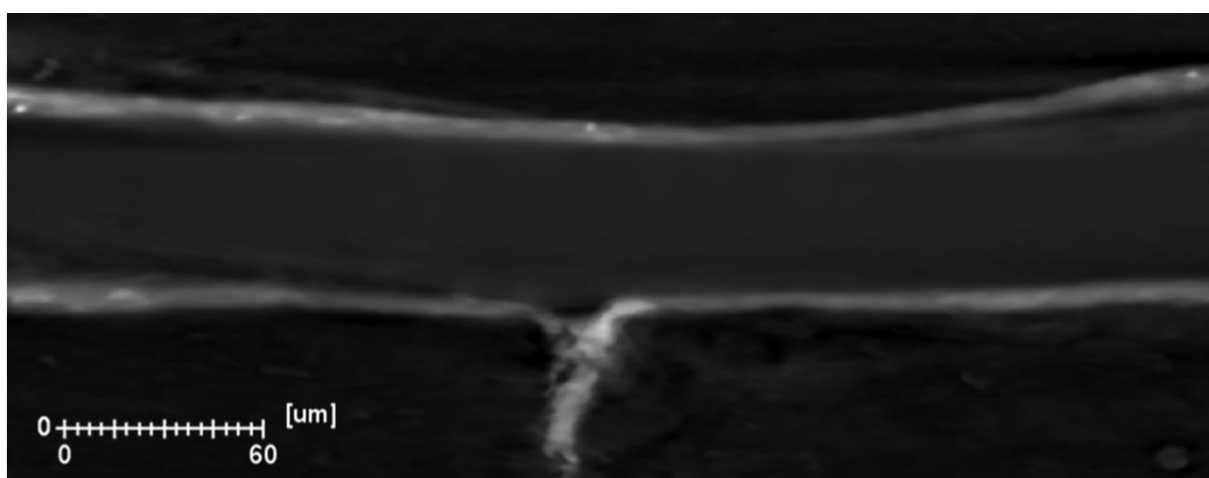


Figure 24 - With extra Nafion before single cell testing

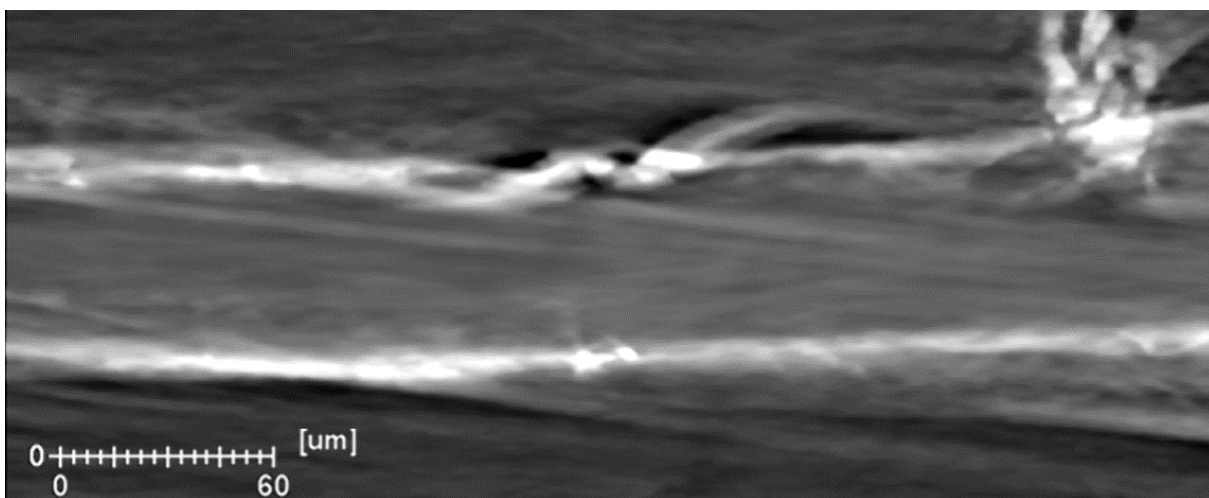


Figure 25 - Without extra Nafion after single cell testing

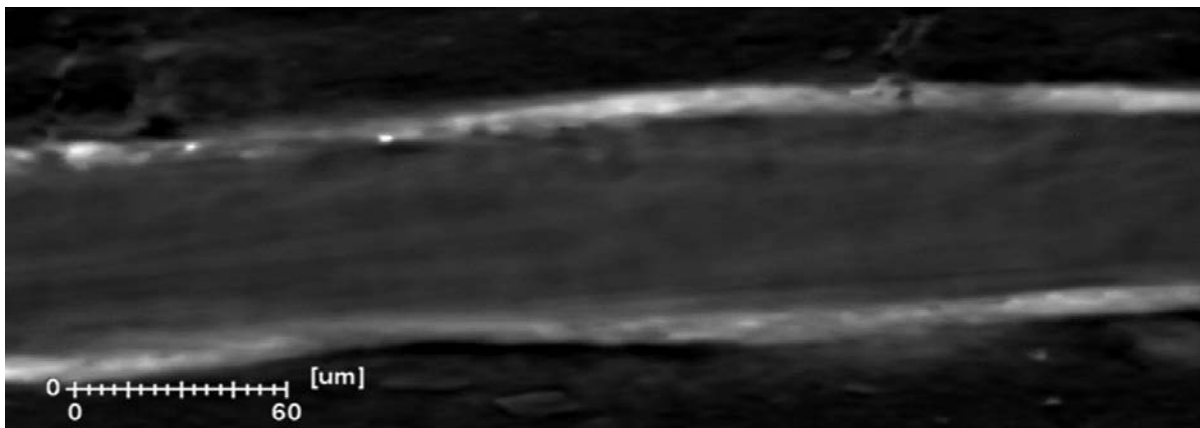


Figure 26 - With extra Nafion after single cell testing

4.1.3.2. Surface Models

The segmentation above allowed the production of images below, which shows both the top and bottom of the catalyst layers (these are the sides of the CL, which are in contact with the Nafion membrane rather than the carbon support).

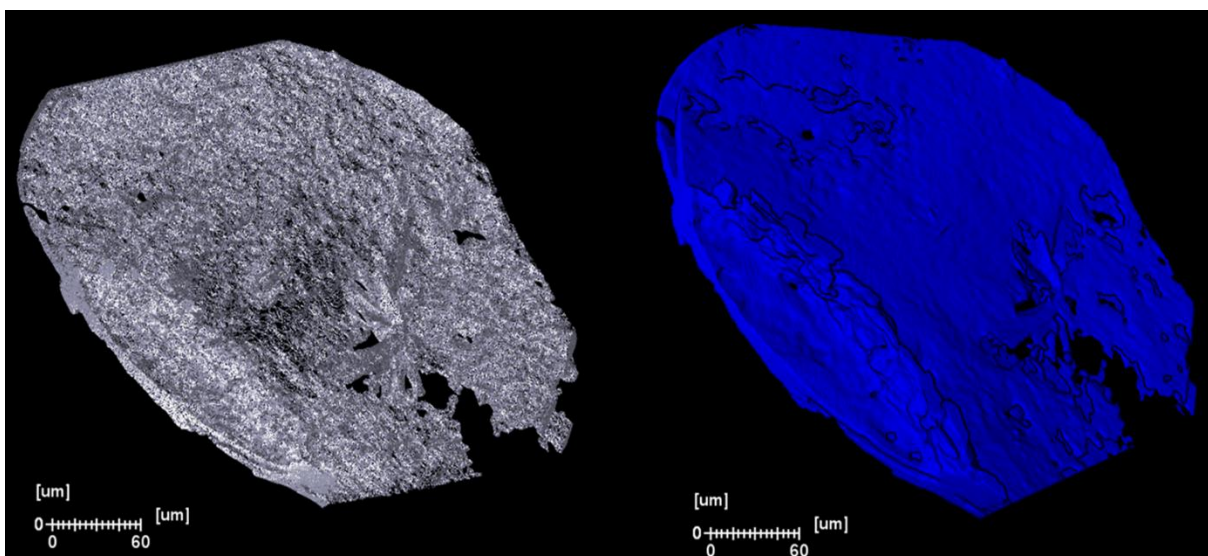


Figure 27 - 3D renderings of the segmented ortho-slice of the top catalyst layer without extra Nafion

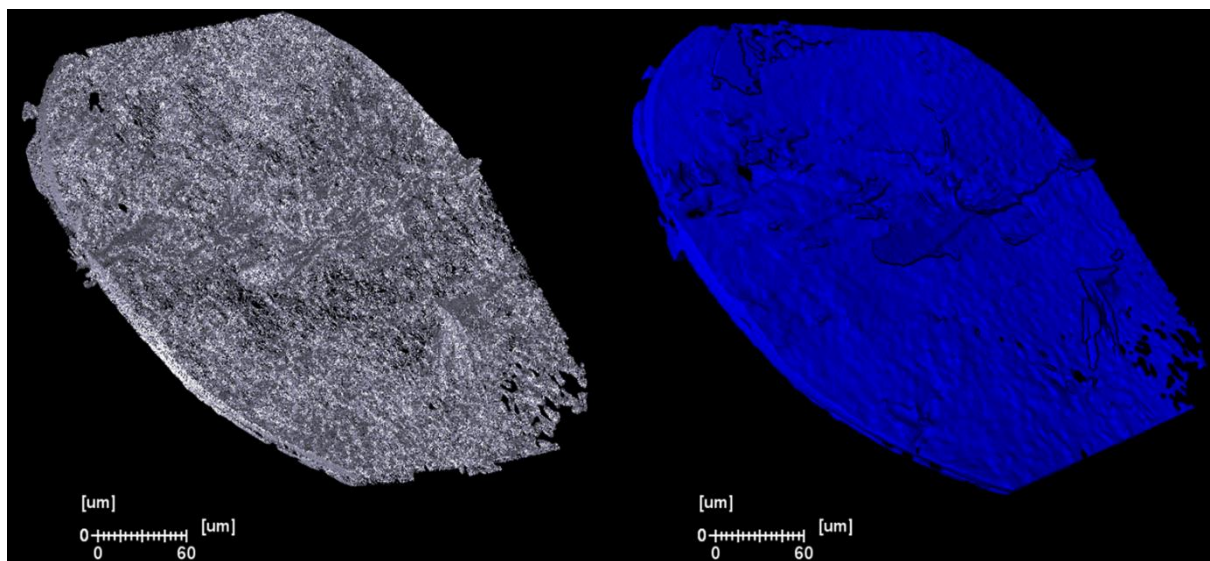


Figure 28 - 3D renderings of the segmented ortho-slice of the bottom catalyst layer without extra Nafion

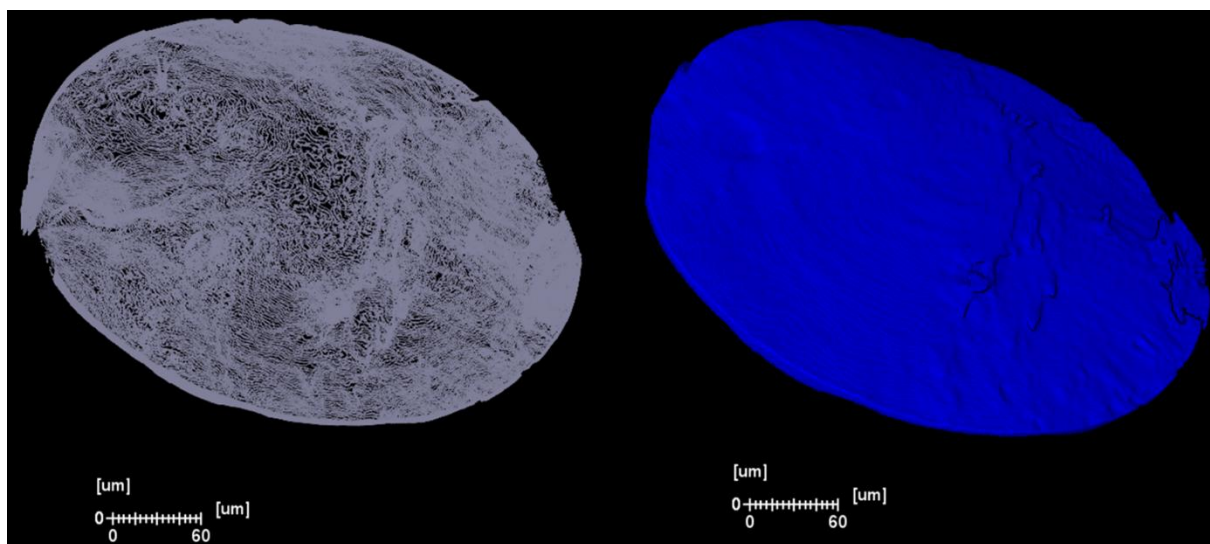


Figure 29 - 3D renderings of the segmented ortho-slice of the top catalyst layer with extra Nafion layer

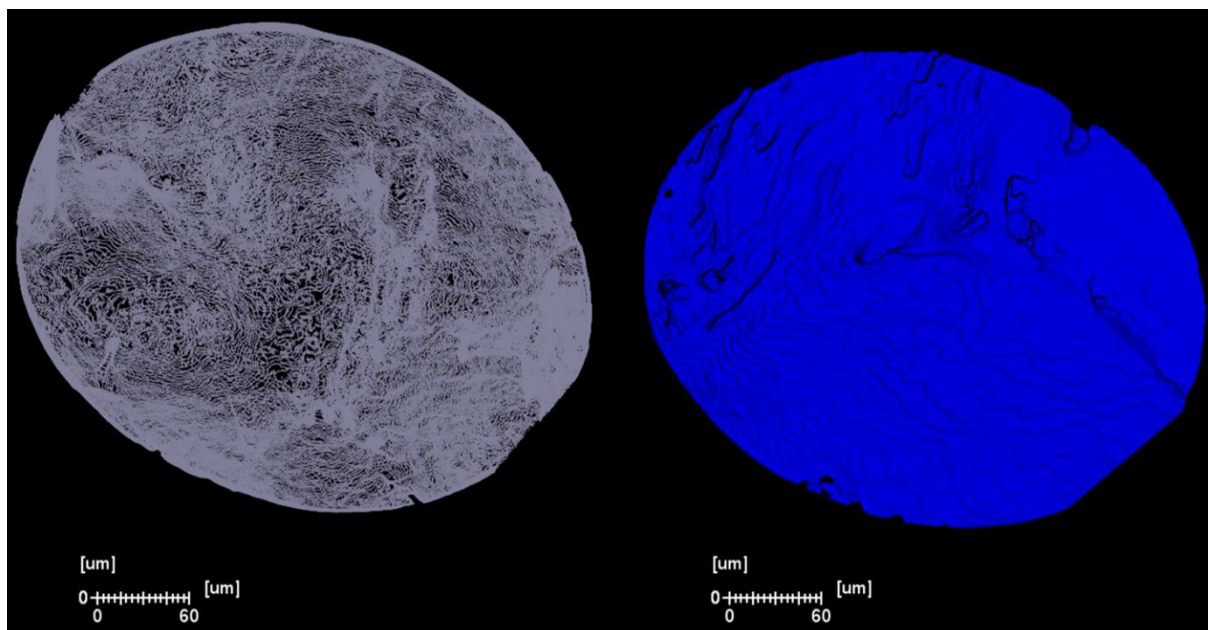


Figure 30 - 3D renderings of the segmented ortho-slice of the bottom catalyst layer with extra Nafion layer

The contour lines module in Avizo was used to produce the white images on the left in the Figures above. This is to show the topography whereas the blue images were produced thorough surface generation and are volume rendered. In the white contour lines images, the black areas show small differences from the base and so these are the flatter areas. It can be seen that both top and bottom with extra Nafion (Figures 29 and 30 respectively) have a larger amount of black compared to the renderings without extra Nafion (Figures 27 and 28), which infers a smoother surface. Therefore, qualitatively this technique shows that the addition of Nafion produces a smoother catalyst surface.

The generated surface was then further analysed using the surface area volume module in Avizo. This was completed on the top CL without and with extra Nafion, Figure 27 and Figure 29 respectively. This provided the surface area in μm^2 and

volume in μm^3 , which can then provide the surface area by volume of each sample as shown in Table 10.

Table 10 - Surface and Volume measurements calculated from the surface area and volume module in Avizo.

Sample	Surface area (μm^2)	Volume (μm^3)	Surface area per unit volume ($\mu\text{m}^2 \mu\text{m}^{-3}$)
Top Without extra Nafion Figure 27	676,832	1,550,774	0.437
Top With extra Nafion Figure 29	340,075	1,281,236	0.265

This module allowed quantitative measurement of the two CL and showed a reduction in surface area per volume of $0.17 \mu\text{m}^2 \mu\text{m}^{-3}$, equal to a loss of 40% surface area when Nafion ionomer was added. A higher surface area of MEA's is desired as the larger the SA the higher the TPB.

4.1.4. *In-situ* testing

The results of *in-situ* testing shown in Figure 31 - Comparison of *in-situ* testing of MEA with extra Nafion added in production and without extra Nafion added in production. show that the addition of Nafion solution onto the commercial GDE does not improve the *in-situ* performance. Both polarisation curves begin with high OCV values as would be expected from commercial GDEs, after around 1000 mA cm^{-2} the reduced performance of the MEA with added Nafion solution begins to show. This area in the polarisation curve suggests Ohmic losses, which are due to the reduction of electron and ionic movement, indicating that the Nafion solution impedes the transport of ions and electrons. This is also shown in the resistance measurements at 2000 mA cm^{-2} ,

which is higher (16.7 mΩ) for the MEA with extra Nafion solution than the MEA without (13.8 mΩ).

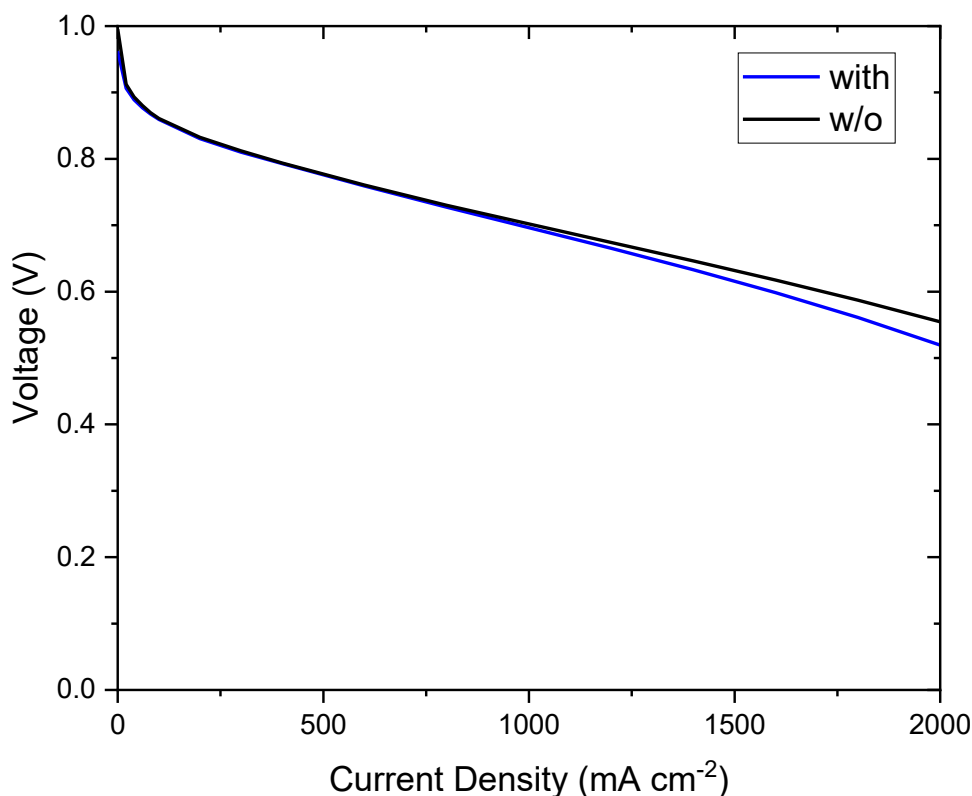


Figure 31 - Comparison of *in-situ* testing of MEA with extra Nafion added in production and without extra Nafion added in production.

4.2. Conclusions

The work in this section provided conclusive results that the addition of Nafion onto the commercial MEAs tested does not improve the activity of the *in-situ* testing. X-ray CT was used to show increased smoothness and decreased surface area to volume ratio by 40% when Nafion ionomer is added to the MEA surface, while SEM and EDX indicated the presence of fluoride in both the MEA with added Nafion and without;

indicating an optimum Nafion amount had already likely been added in the commercial manufacturing process. *In-situ* testing also showed that not only did the extra Nafion MEA perform worse than the MEA without extra Nafion, but it also had higher resistance values. This Chapter highlights the importance of ensuring techniques stay up to date as they are disseminated to new members of a team as small changes in materials can mean that an added step reduces the quality of testing rather than improving it.

5. SYNTHESIS, CHARACTERISATION AND TESTING OF PALLADIUM ALLOY CATALYST

5.1. Synthesis of PdIrAu/C catalyst

To prepare the catalyst a sol-immobilisation synthesis method was utilised which is similar to that reported by Hutchings *et al.*¹³⁸ The salts of all three metals, PdCl₂ (Sigma Aldrich, 99%), IrCl₃ (Heraeus Chemicals, 54% metal content) and HAuCl₄·3H₂O (Sigma Aldrich, 49 % metal content) were added to ultrapure water with the resistivity measured as $\geq 18.2 \text{ M}\Omega \text{ cm}$ (Millipore) in a 1:1:1 molar ratio and stirred for 30 mins. Following the published procedure mentioned above, polyvinyl alcohol, PVA (Sigma Aldrich, Mw 80,000), used to prevent sintering in the annealing stage, was added to the solution to achieve a ratio of PVA : (Pd + Au + Ir) = 1.2 (w/w).¹³⁸ Then, sodium borohydride, NaBH₄ (Sigma Aldrich, 98 %) was added such that NaBH₄ : (Pd + Au + Ir) = 5 (mol/mol), and the solution stirred for 30 minutes for sol generation. After this period the solution was immobilised onto carbon Vulcan XC-72R (Sigma Aldrich) which was added to the solution to achieve C:(Pd + Au + Ir) = 60:40. This was then left to stir at the highest setting (the same stirring plate was used throughout for consistency) for two hours to achieve a homogeneous mixture. Next, the supported catalyst was filtered and washed thoroughly with ultrapure water, before drying in the oven for 14 hours at 120 °C, to yield a fine black powder. Previous work has suggested improved catalytic performance after annealing, therefore this product was heated to different temperatures (400 and 600 °C) to allow comparison of optimum annealing temperature.¹⁶¹

5.2. TGA

After preparation of the nanoparticles as described in the synthesis method above, TGA was used to confirm the synthesis obtained a catalyst with 40 wt% metal loading on carbon within the error margin of the TGA. The sample was heated in a crucible with a lid under air in the temperature range 25 – 900 °C at a rate of 10 °C min⁻¹ to gain well-defined peak points. Figure 32 below shows the gradual combustion of carbon between 450-650 °C leaving the 40 wt% metal. Confirming the synthesis technique produced a catalyst in the expected amounts, proving the synthesis is an efficient method.

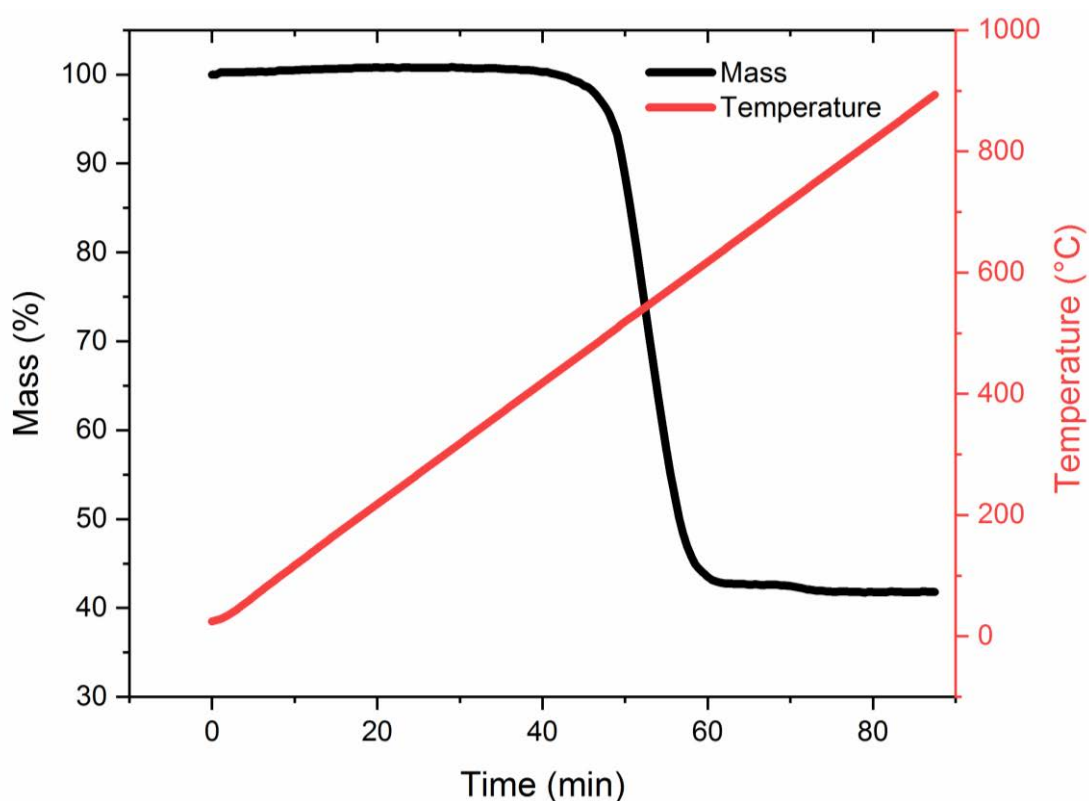


Figure 32 - Thermogravimetric measurement showing the loss of carbon leaving the metal content as the residual mass

5.3. TEM

The three differently annealed catalysts (non-annealed and annealed at temperatures 400 and 600 °C) were each dissolved into a solution, with 1 mg catalyst to 1 mL IPA (25% purity). This was then applied to a holey carbon TEM grid and analysed to obtain the particle size. The TEM micrographs shown in FiguresFigure 33Figure 34 and Figure 35 highlight that each catalyst, whether annealed or not are agglomerated and not well dispersed over the carbon support. However, in Figure 34 the highest agglomeration by far can be seen in the 600 °C annealed catalyst, where the sample has passed the point of agglomeration, and had coarsened. The 400 °C annealed catalyst shows poor dispersion, however the particles are still only agglomerated and not yet coarsened, providing a larger surface area than the 600 °C annealed PdIrAu/C. Unfortunately, the particles were too agglomerated to produce a histogram to indicate exact average particle size, though for the PdIrAu/C catalyst supported on carbon the metallic particles are around 5 nm. The HAADF image in Figure 36 also illustrates the lack of coarsening in the 400 °C annealed sample. Therefore, all further testing was completed on the 400 °C annealed sample. This sample will also have been heat treated enough so that the PVA used in synthesis will have decomposed which is vital as any residual PVA could affect the dissolution of the catalysts.^{162,163}

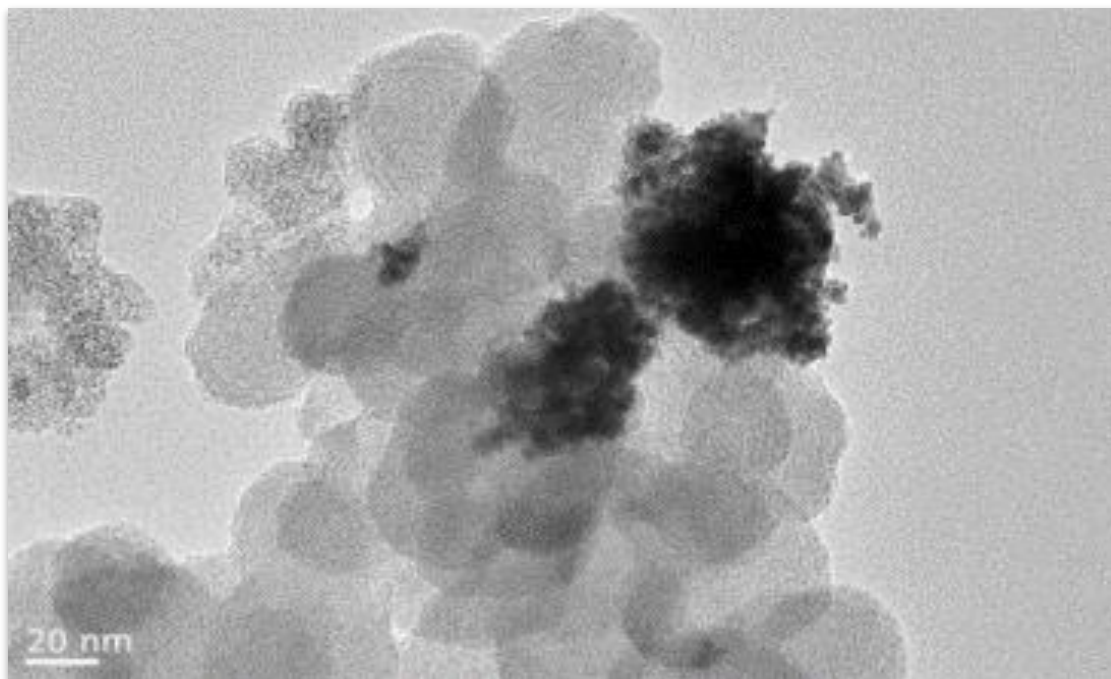


Figure 33 - TEM image of PdIrAu catalyst (dark black agglomerated particles) supported on carbon black (larger onion like particles) annealed at 120 °C under nitrogen.

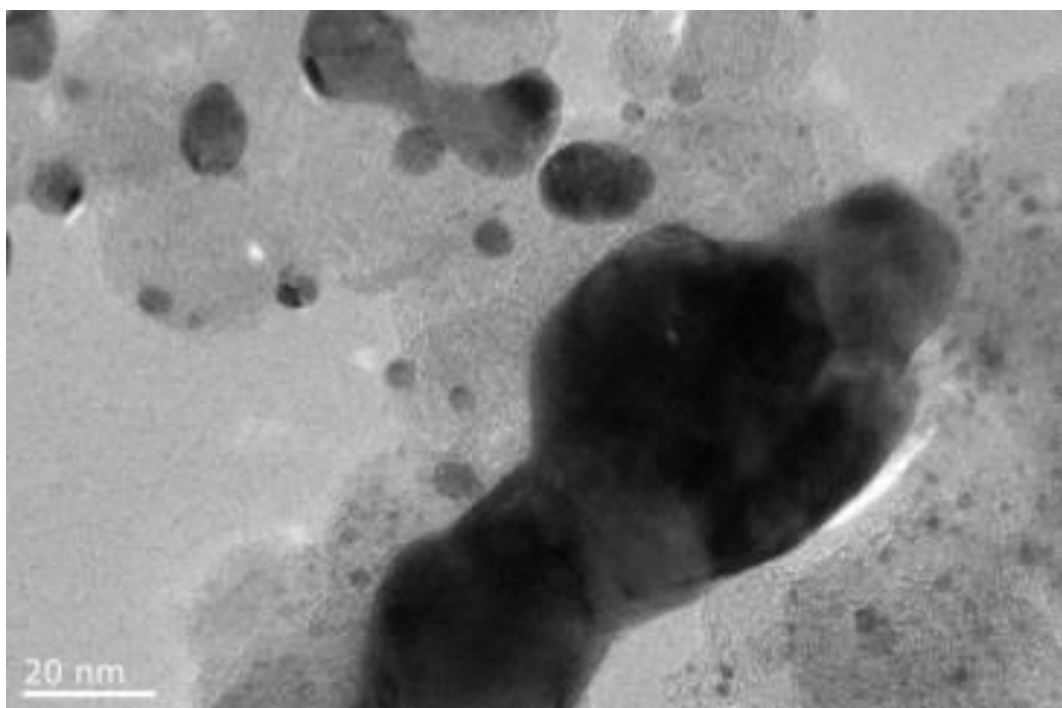


Figure 34 - TEM image of PdIrAu catalyst (large dark black coarsened particles) supported on carbon black (onion like particles) annealed at 600 °C under nitrogen.

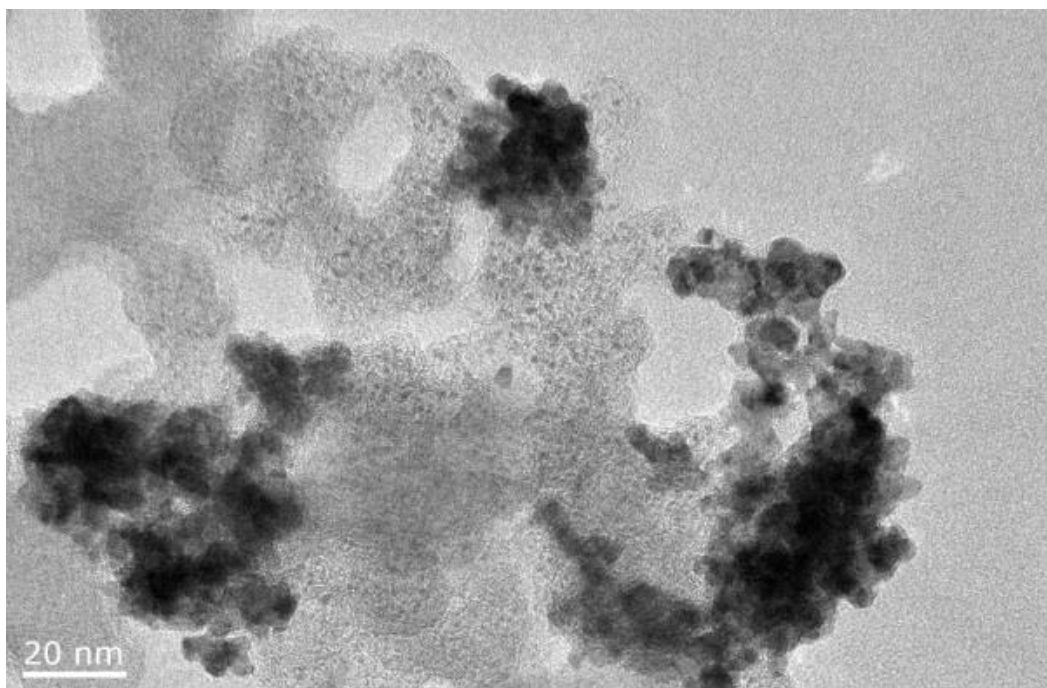


Figure 35 - TEM image of PdIrAu catalyst (dark black agglomerated particles) supported on carbon black (larger onion like particles) annealed at 400 °C under nitrogen.

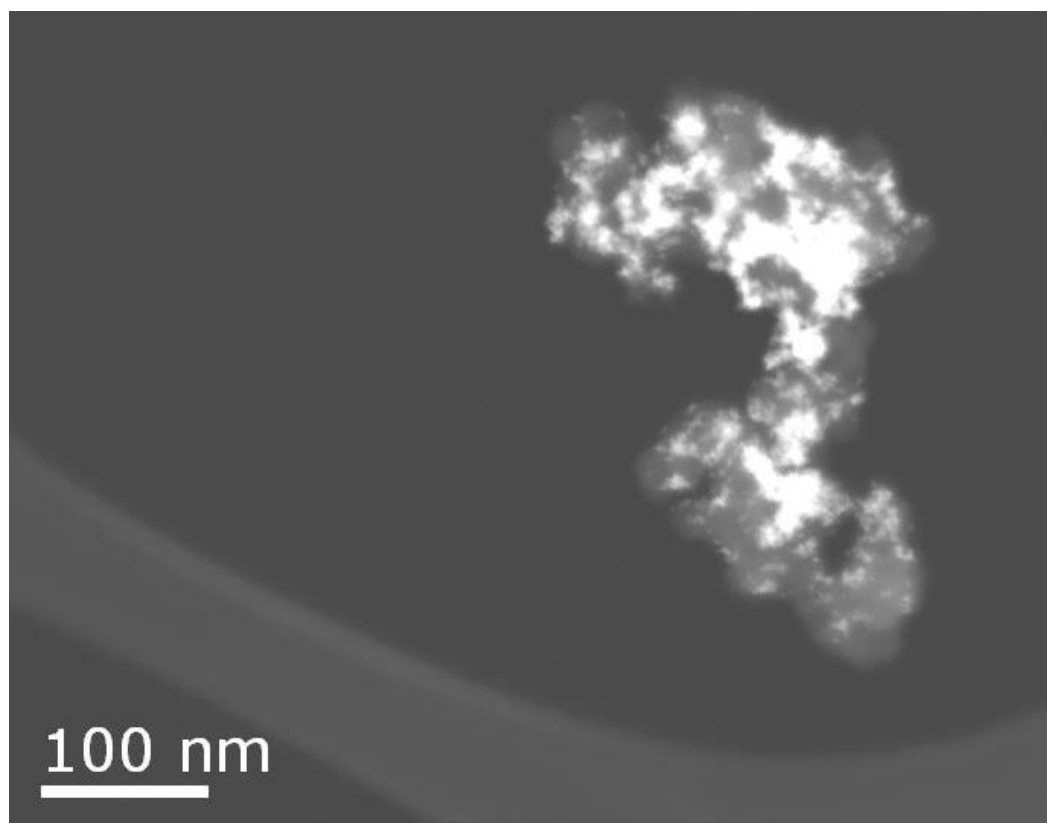


Figure 36 - HAADF image of PdIrAu catalyst (dark black agglomerated particles) supported on carbon black (larger onion like particles) annealed at 400 °C under nitrogen.

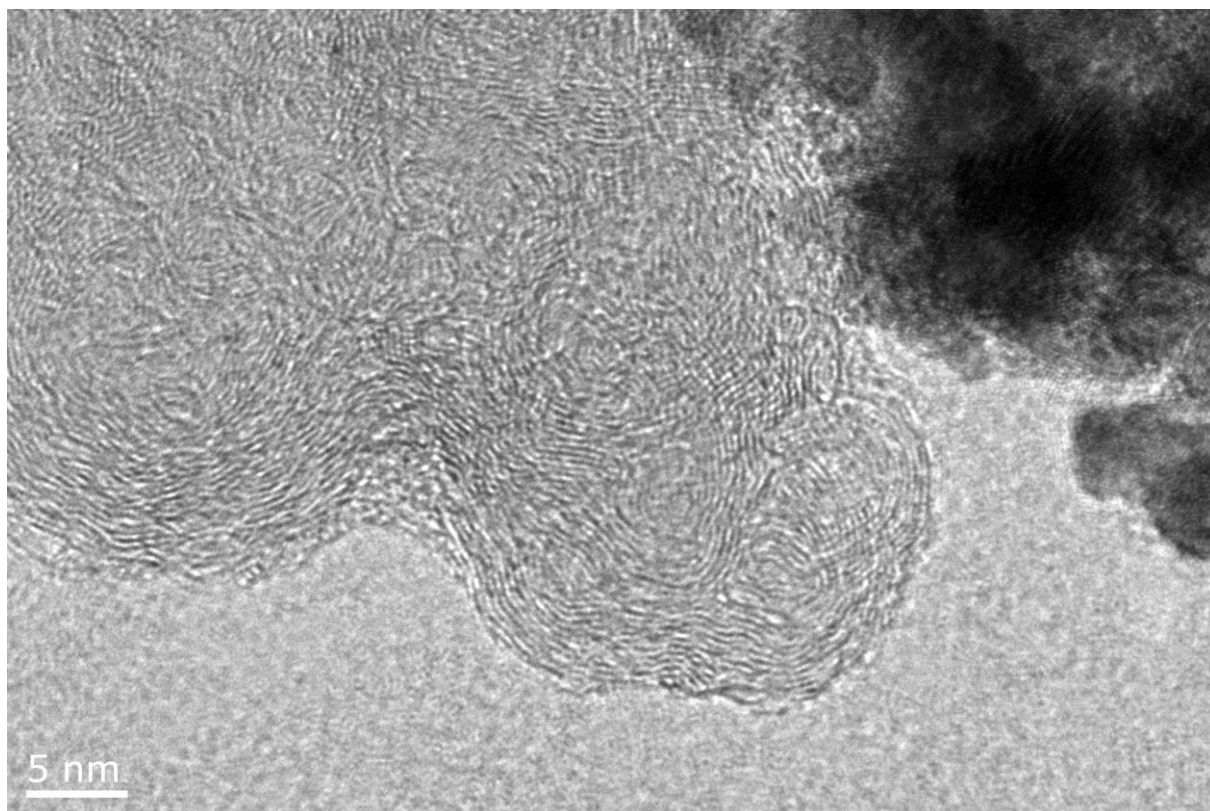


Figure 37 - TEM image of the 400 °C annealed PdIrAu sample.

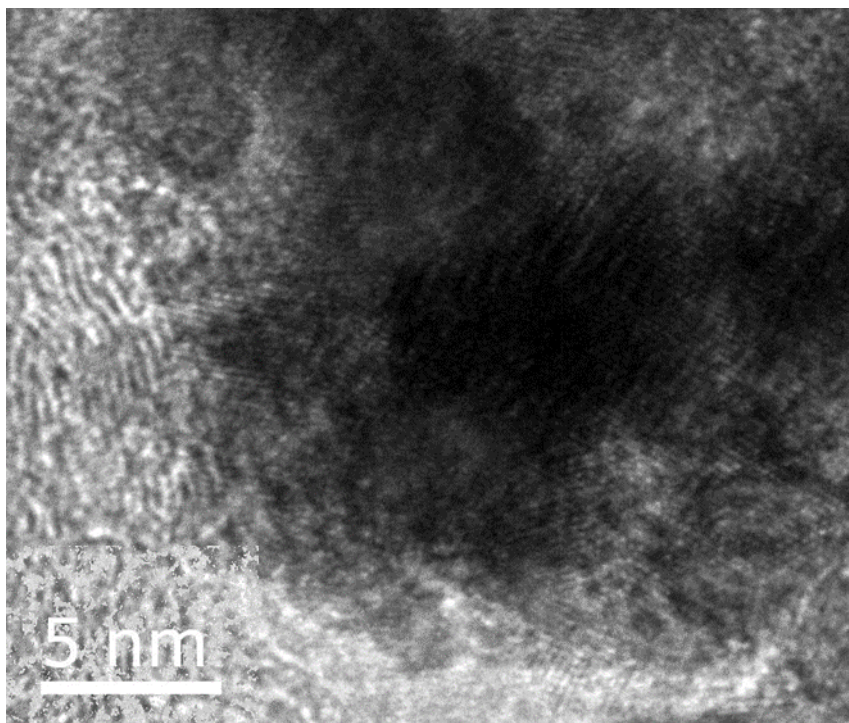


Figure 38 - Magnified top right section on Figure 37 showing PdIrAu/C particles where the lattice spacing is clearly evident.

The lattice spacing shown in Figure 37 and magnified in Figure 38 was measured using ImageJ software, ten lattice spaces were measured to produce an average spacing of $d = 0.245$ nm. Within the region of error of measurements this shows an fcc (111) lattice plane as the values for the (111) plane of Pd, Ir and Au are 0.22, 0.22 and 0.24 nm respectively.^{164,165,166} It has also previously been shown that strain within the particles can cause an increase in lattice spacing.¹⁶⁷

5.4. EDX including mapping

The EDX imaging (Figure 39) obtained from the PdIrAu/C catalyst at all annealing temperatures showed Pd, Ir, Au and C and elemental mapping of the annealed samples showed good dispersion of the metals within the nanoparticle. However, imaging showed small particles of Ir around the particle, whereas Pd and Au are almost completely within the particle. It has previously been shown that Ir can decompose during TEM analysis because of the reducing ability of the electron beam used.¹⁶⁸

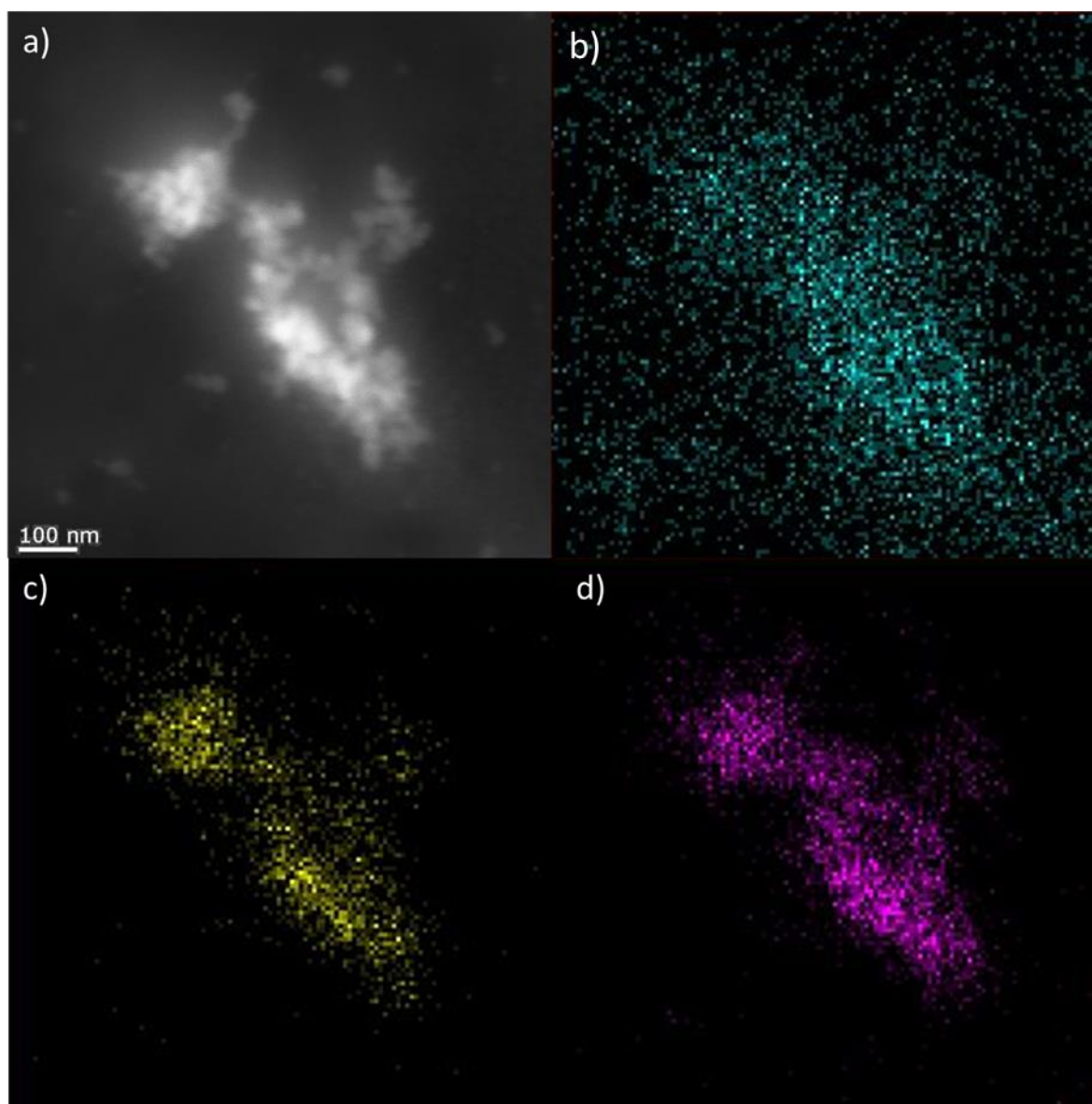


Figure 39 - a) Initial HAADF image, b) EDX map of Ir content, c) EDX map of Pd content, d) EDX map of Au content.

5.5. XRF

X-ray Fluorescence was used to analyse the impact the ASTs had on the composition of the catalyst. The XRF technique used is non-destructive and is therefore, a useful technique for before, and after analysis as it does not affect the sample. The XRF technique allowed quantification of the Pd, Ir and Au before and after the ASTs to gain

understanding of the dissolution of the metals. This was completed by way of measuring the peaks in the spectrum produced at the energies at which the peaks appear for the particular elements as can be seen in Figure 42 and Figure 43. The low energy peak could be used for Pd (around 2.8 keV), however the higher energy peaks had to be used to analyse Ir and Au (around 9.2 and 9.7 keV respectively) as the low energy peaks for Au and Ir (around 2 keV) were overlapping and so could not be distinguished. The percentage loss calculated was taken from the reduction of the area under each peak attributed to the metal, by integrating this area and analysing the difference. The reduction in the Pd peak is also visually observable in the sample including Au when compared to the spectra without Au.

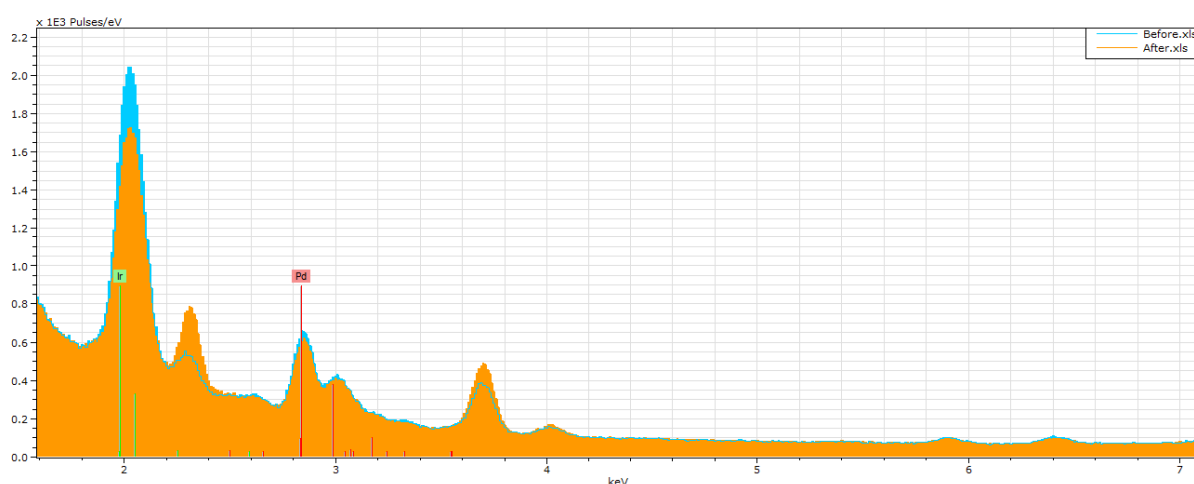


Figure 40 - XRF spectra of PdIr/C in low energy region with Pd and Ir peaks highlighted.

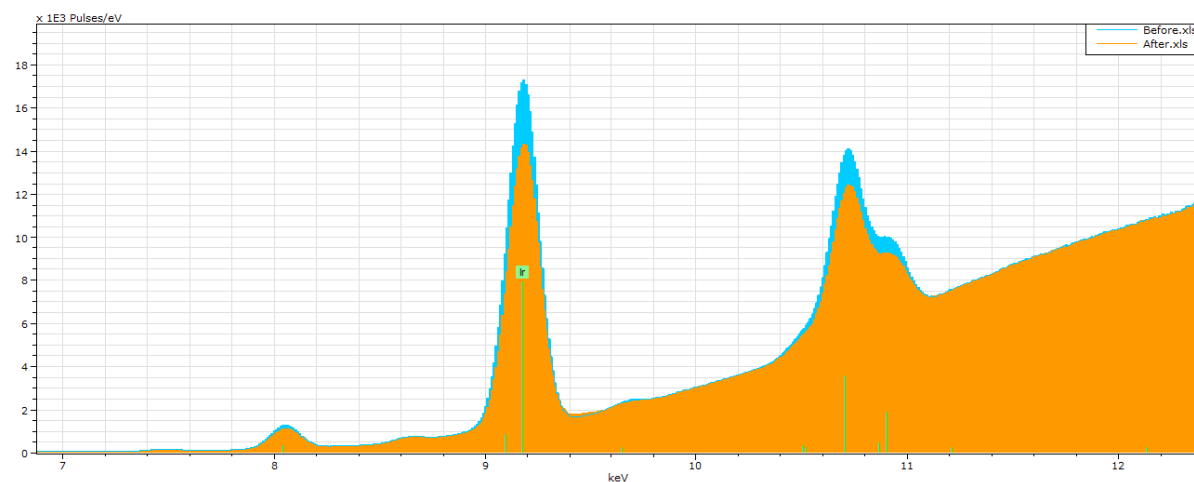


Figure 41 - XRF spectra of PdIr/C in high energy region with Pd and Ir peaks highlighted.

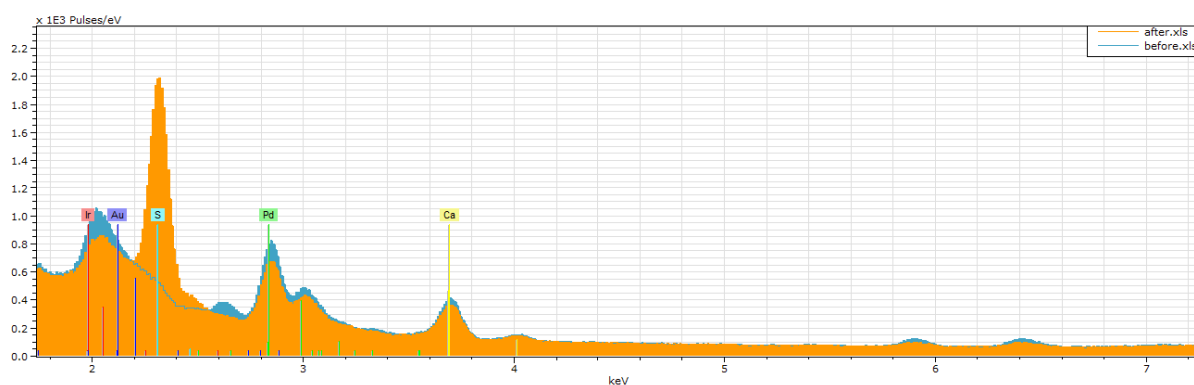


Figure 42 - XRF spectra of PdIrAu/C in low energy region with Pd, Ir and Au peaks highlighted.

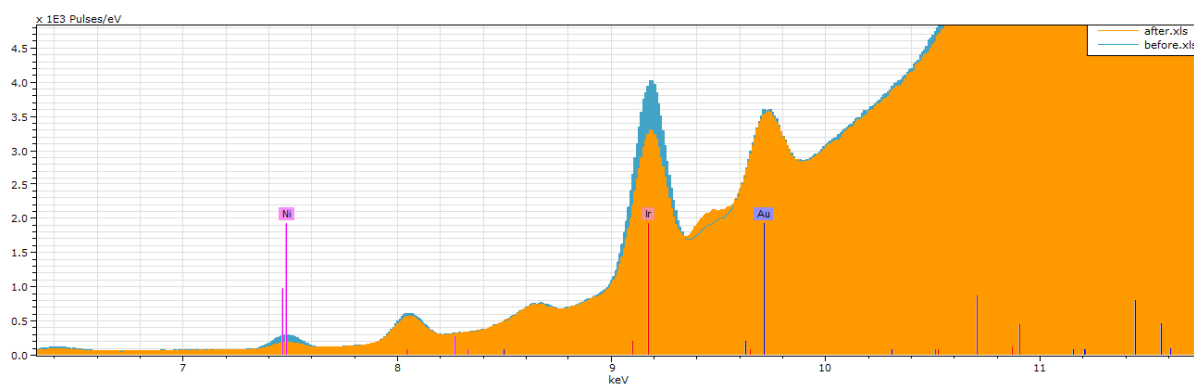


Figure 43 -XRF spectra of PdIrAu/C in high energy region with Pd, Ir and Au peaks highlighted.

PdIr/C showed a loss of 16% of Ir after AST cycling and a 5% Pd loss. Although Pourbaix diagrams of Ir suggest that it should not dissolve at this pH and potential range, these XRF results suggest otherwise. The XRF results also showed the addition of Au into the catalyst increases the dissolution of Pd rather than stabilises it with Pd and Ir both losing 14% and Au losing less than 1% after ASTs. The XRF results do not complement the ICP-MS results, which were also performed after AST cycling and are the opposite of what is theoretically expected. These results are more likely to be incorrect due to the very small size of the nanoparticles, which are too small for the size of the X-Ray source and therefore make XRF more of a qualitative rather than quantitative experiment for nanoparticle sizes of around 5 nm. These XRF results therefore can be looked at as a qualitative study, which confirms all three metals; Pd, Ir and Au are present in the alloy both before and after AST cycles, as can be seen in Figure 44.

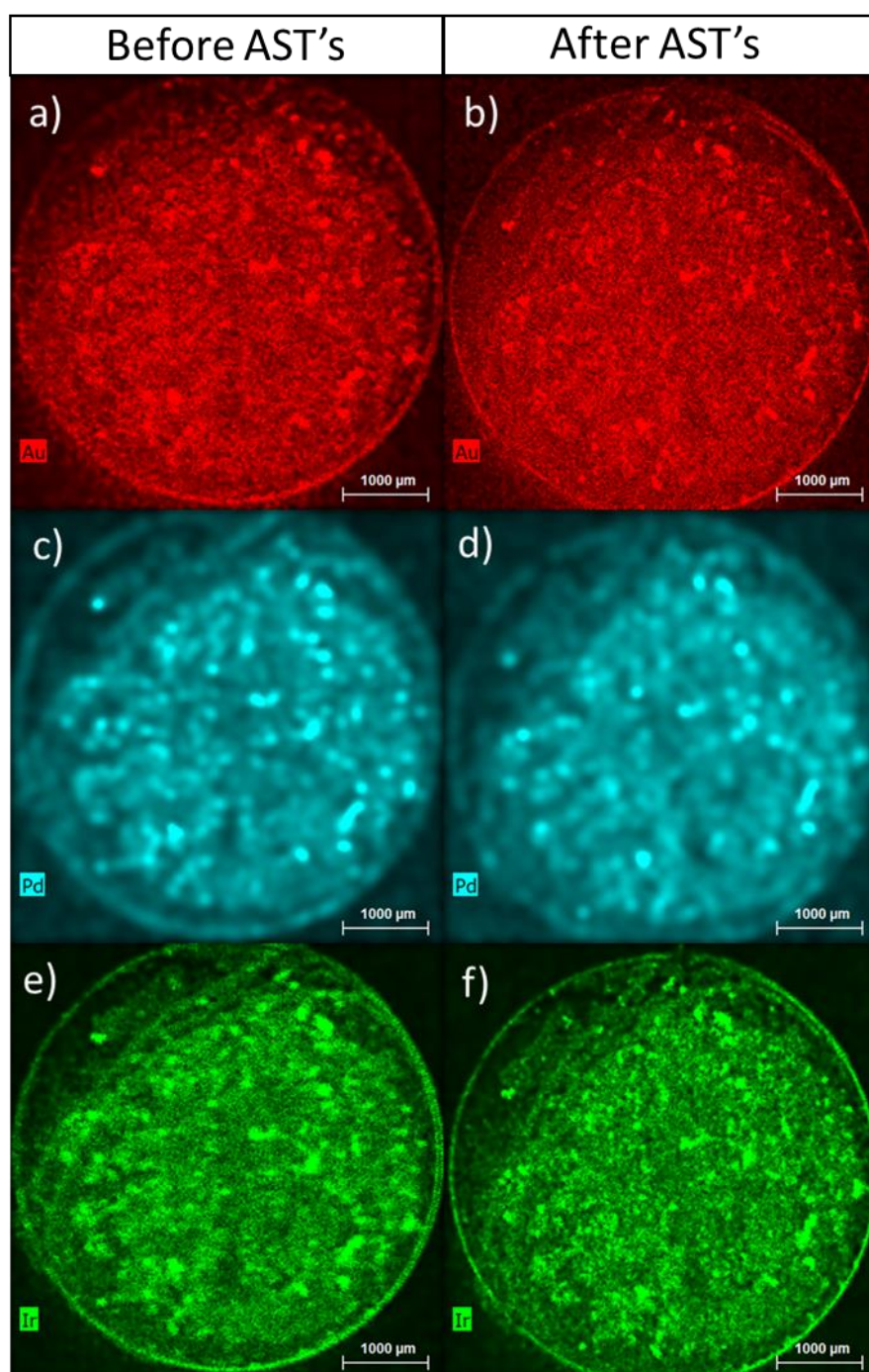


Figure 44 - XRF images of a coated circular RDE tip with elemental analysis of a) Au before AST cycles b) Au after AST cycles c) Pd before AST cycles d) Pd after AST cycles e) Ir before AST cycles and e) Ir after AST cycles.

5.6. XRD

Next, the structure of the catalyst annealed at 400 °C was investigated by XRD and the resulting diffraction pattern of PdIrAu/C is shown in Figure 45 alongside PdIr/C for comparison. The three major peaks in each spectrum at around 40°, 45° and 68° can be attributed to the (111), (200) and (220) planes respectively of a face centred cubic lattice.¹⁶⁹ Pd, Ir and Au all form face centred cubic lattices.

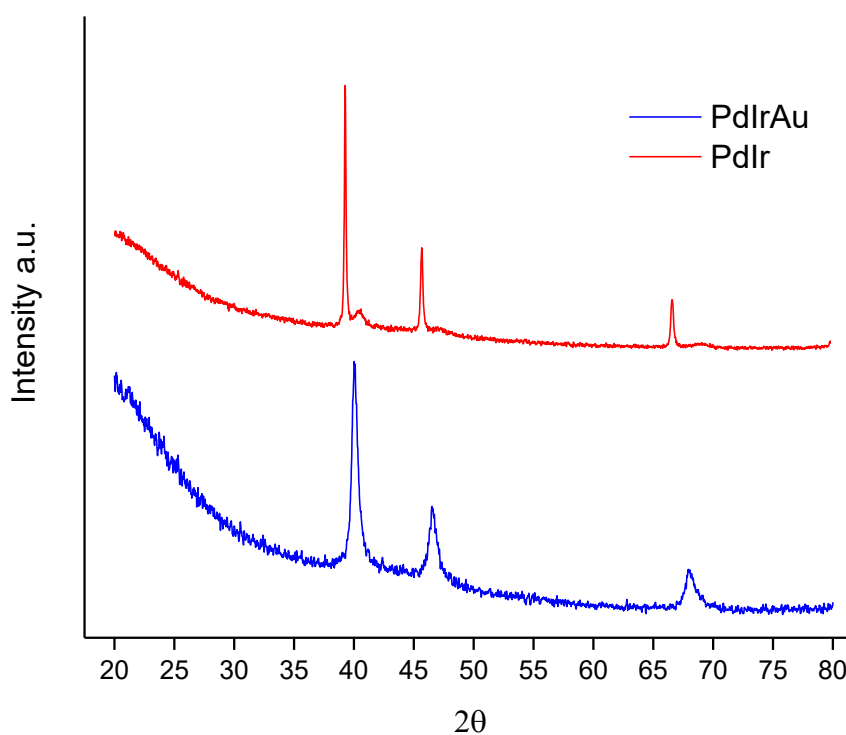


Figure 45 - X-ray diffraction pattern of PdIrAu/C catalyst.

A change in lattice parameter can indicate alloying where Ir and Au particles are inserted into the Pd lattice thus changing the lattice parameter. The atomic ratios of Pd, Ir and Au are 137, 136 and 144 pm respectively.¹⁷⁰ The PdIrAu/C peak is shifted to lower 2θ and has a larger lattice parameter as Au is larger, which indicates that

some extent of alloying has taken place. Additionally, as there are not separate peaks but a single peak at each plane indicates that all three of the metals have formed an alloy. Previous work has also shown Au and Ir to alloy with Pd by analysing the XRD result in this way.^{96,127,171} The particle size was not measured via XRD as the XRD measures average crystallite size instead of particle size, and as these particles are likely to consist of more than one crystallite, XRD crystallite size is typically smaller than TEM particle size.

5.7. *Ex-situ* degradation

The electrochemical performance of the catalyst was then investigated via cyclic voltammetry. Cyclic voltammetry was used to calculate the electrochemically active surface area (ECSA) of the catalyst, these were recorded under a N₂-saturated electrolyte, while potential cycling between 0.05 V and 1.0 V at a voltage scan rate of 20 mV s⁻¹. *Ex-situ* advanced stress tests (ASTs) were also performed in a N₂-saturated electrolyte by performing 1000 potential cycles between 0.05 V and 1.0 V at a voltage scan rate of 50 mV s⁻¹. The potential cycling in the ASTs will continually alter the potential the catalyst is subjected to and this is a useful method to predict how a catalyst will behave under normal fuel cell operating conditions. In this case, the ASTs are run in this range because these are the most likely potentials an anode catalyst is likely to be subjected to under start-up and shut-down conditions within an operating fuel cell.¹³⁷ The degradation tests used in this work are similar to the standard DoE test procedures commonly used in the assessment of electrocatalysts; however, these have been adapted for the anode catalyst as described in the methods Chapter.⁷³

The ECSA is typically used as a measure of both the catalytically active area and a means to monitor the catalyst loss or degradation. The dissolution of each metal from the alloy depends on the pH of the surrounding solution and electrode potential; this behaviour can be predicted by Pourbaix diagrams, which are shown in Figure 46, the details of these are not required but are used to highlight the higher potential at which oxides are formed on Au than both Ir and Pd.

The metal dissolution can occur by both surface oxidation and by the reduction of already formed surface oxides. The Pourbaix diagrams of Pd, Ir and Au at low pH will reach its corrosion potential at 0.987 V, 1.15 V and 1.68 V respectively. Due to the properties of the individual metals, precise ECSA measurements of the alloy are difficult, different electrochemical techniques can be employed however each require assumptions which may compromise the results. CO stripping which is common for Pd catalysts did not give a reliable result with only a very small change in current density produced in the CO potential region. This is due to the Au content of the alloy which does not adsorb CO in the same way, Al-Odail *et al.* showed that an increasing content of Au makes the technique inapplicable to catalysts containing Au as can be seen in Figure 47.¹²⁹

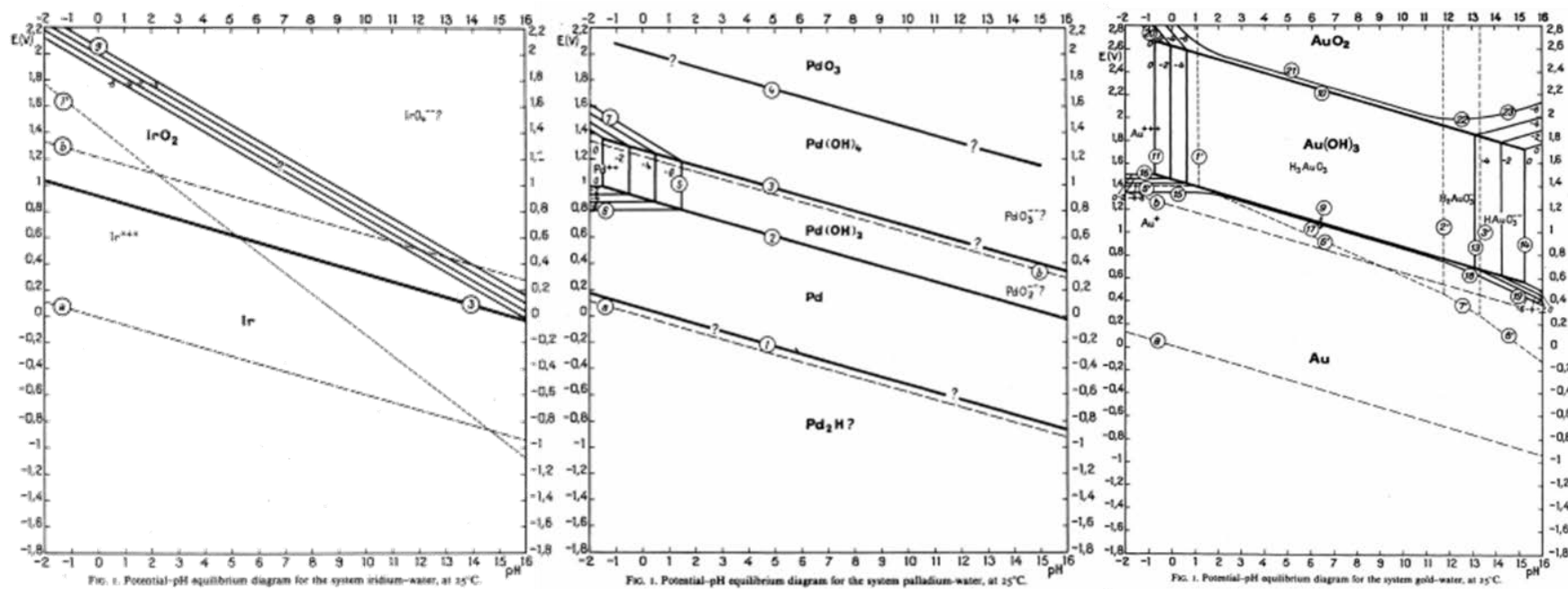


Figure 46 - Pourbaix diagrams of iridium, palladium and gold.

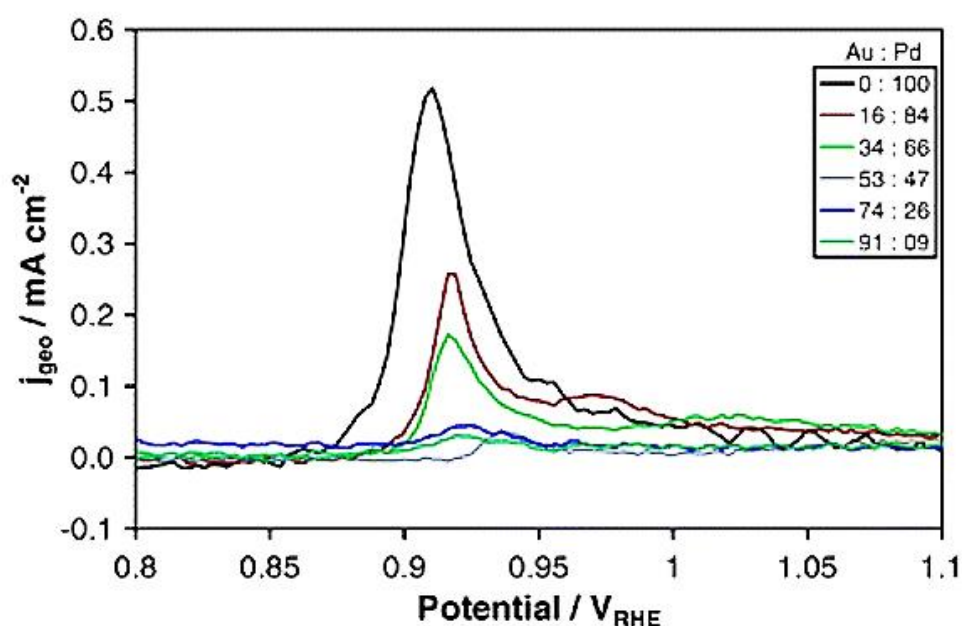


Figure 47 - Reducing CO stripping curve with increased Au content in PdAu catalyst. Reproduced from with permission from PCCP owner societies.¹²⁹

Surface oxide desorption has also previously been used for ECSA measurement though in this case the presence of Ir meant that the oxides present could not be stripped fully and produced poor results. Another method of ECSA measurement for is mercury deposition, though in this case it could not be used as mercury breaks the gold lattice bonds through amalgamation.¹⁷² The commonly used average for Pt ($210 \mu\text{C cm}^{-2}$) is often applied without knowing the proportions of the crystal faces at the surface which would affect this value. However, for Pd it is even more difficult due to the H adsorption. The result of all the above factors is that the calculation of the ECSA in this case should be viewed as an indication of rather than an exact measurement.

ECSA measurements were taken before any AST cycles were performed and these initial values were then compared to the ECSA measurements after 20, 100, 500 and 1000 AST cycles. Figure 48 compares the ECSA loss compared to the initial ECSA value. This process was repeated 3 times and the error between these measurements

is shown in Figure 48. This Figure shows a greater loss of ECSA initially for the PdIr catalyst until AST 500 where PdIrAu has a larger ECSA loss than PdIr and this continues to the ECSA measurement after AST 1000. Whilst Figures 49 and 50 show the PdIrAu/C and PdIr/C ECSA measurements after the AST cycles respectively.

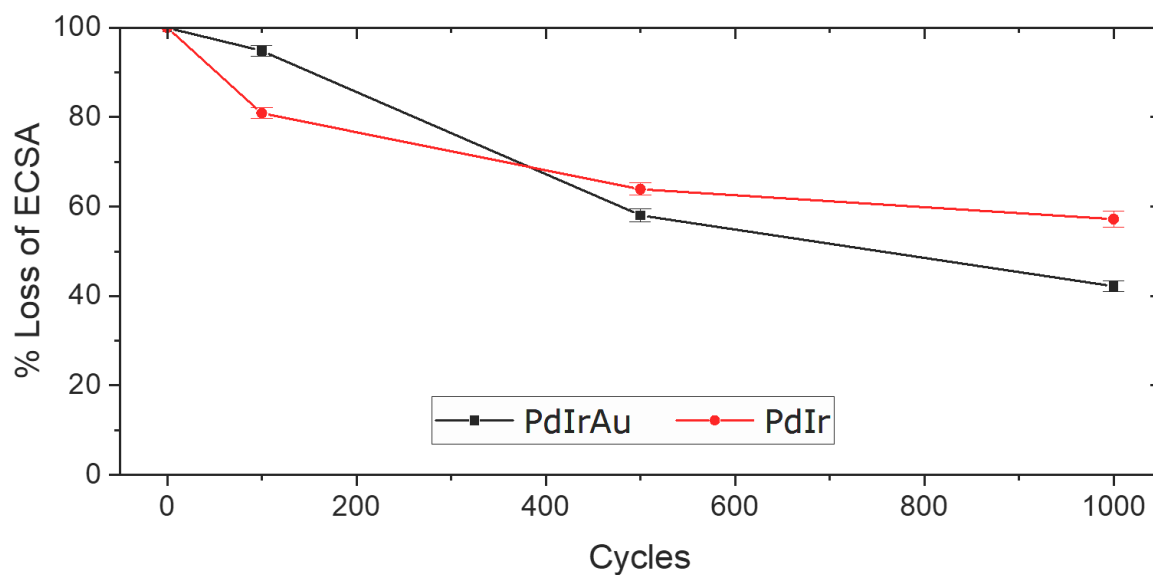


Figure 48 - Graph depicting the remaining ECSA after AST cycling of the PdIr/C and PdIrAu/C catalysts

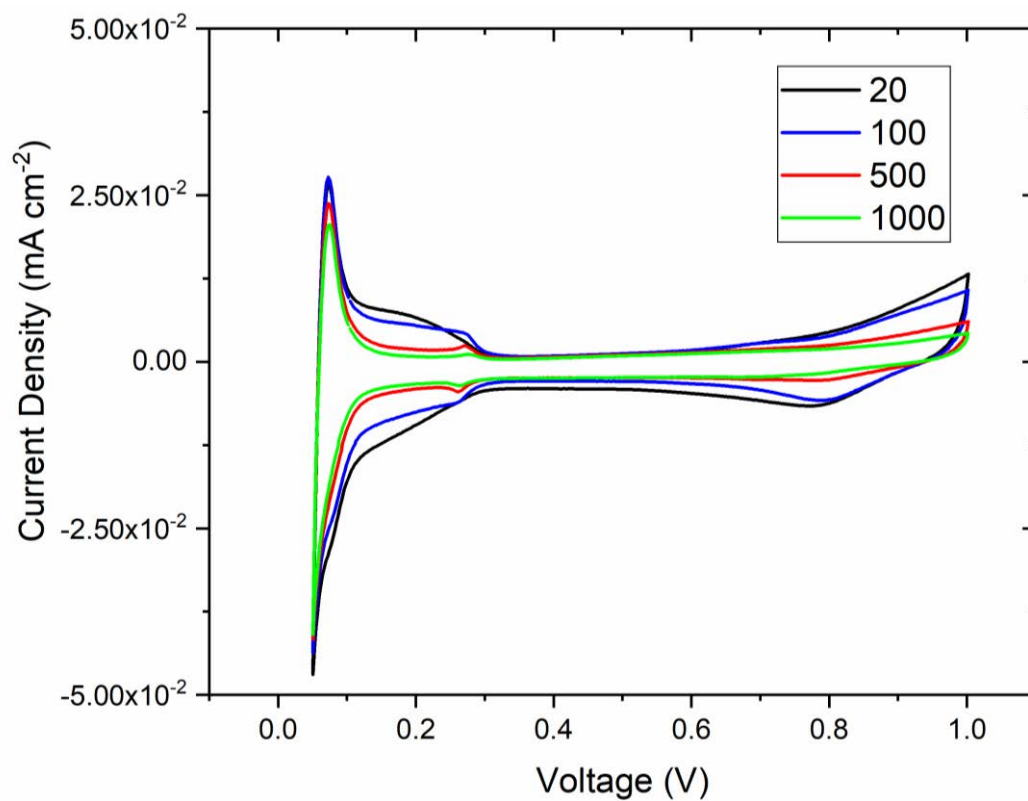


Figure 49 - Cyclic voltammograms of PdIrAu/C catalysts after 1000 AST cycles

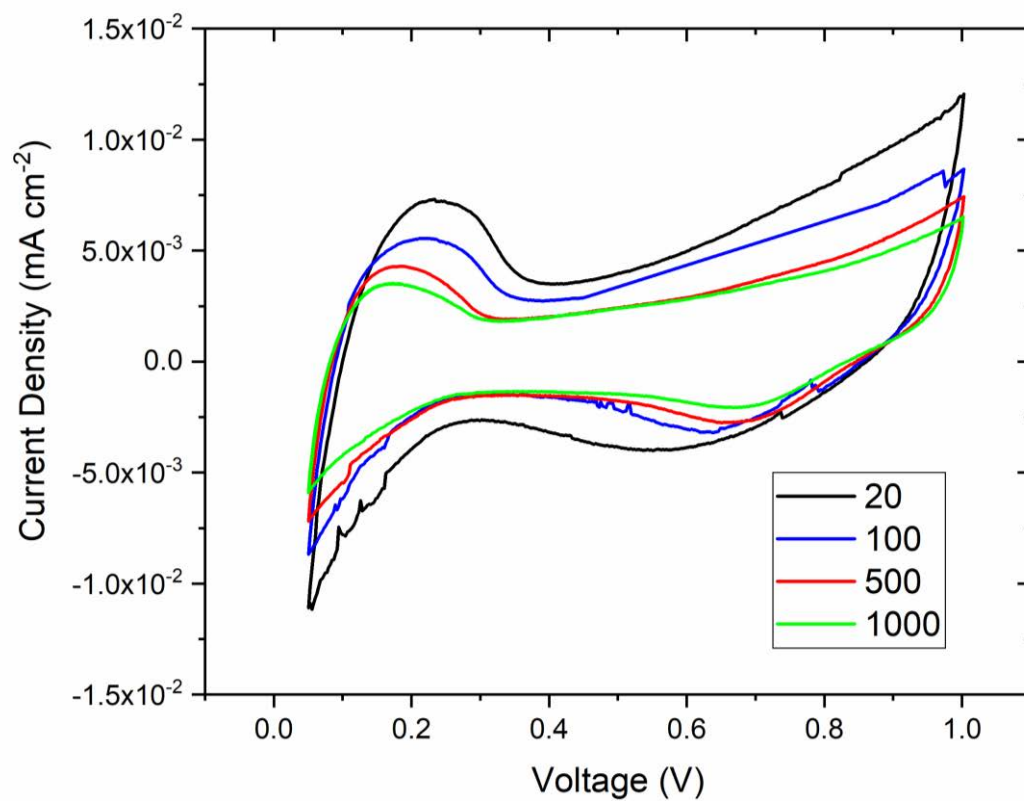


Figure 50 - Cyclic voltammograms of PdIr/C catalysts after 1000 AST cycles

5.8. ICP-MS

To complement this approximate analysis, ICP-MS was used to measure the amount of metal lost into the electrolyte from the electrode after 1000 AST cycles. 20 mL of electrolyte was collected after 1000 AST cycles, this analysis allowed the quantification of metal dissolution caused by the potential cycling. The ICP-MS results show that by adding Au into PdIr after 1000 cycles there is less degradation, and this is likely due to the higher potential onset of the oxide peak. To show this later onset of the oxide peak Figure 51 below shows that in this case the addition of Au into the alloy has moved the oxide peak to a higher onset potential and therefore reducing the main dissolution pathway for Pd, confirming why there is less Pd loss. This increase in onset potential has been shown by others previously upon alloying Pd with Au, further confirming the creation of an alloy through this synthesis method.⁹⁶

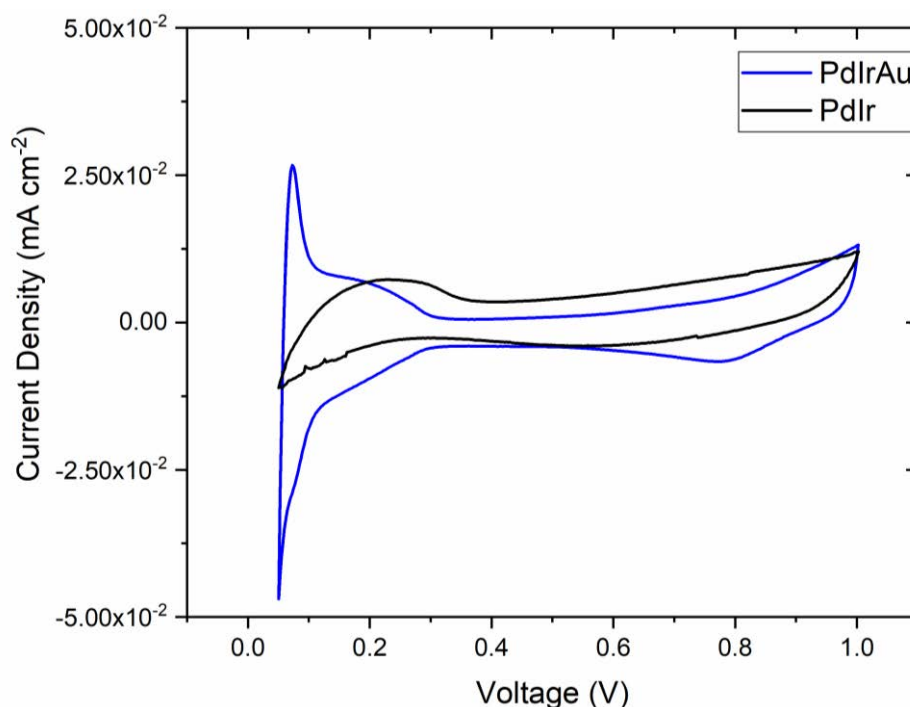
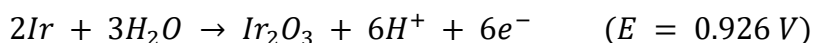


Figure 51 - Comparison of cyclic voltammograms of the PdIr/C and PdIrAu/C catalysts. The onset potential of the PdIrAu/C catalyst is at a higher potential than that of PdIr/C.

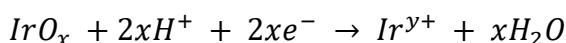
Figure 52 and Figure 53 show the ICP-MS results of the loss of each metal after AST cycles. Au is not included as the loss was too small and was under the detection limits of the ICP-MS. The ICP-MS shows a greater loss of both Ir and Pd in PdIr/C than in PdIrAu/C. A large loss of Ir can be seen in PdIr/C. This was also seen in previous dissolution work by Jervis *et al.* which also indicated a higher loss of Ir than Pd in a PdIr/C catalyst via ECSA analysis.¹⁷³ While Ir should not directly dissolve electrochemically in the potential range 0–1 V, its dissolution due to reversible formation of surface oxide does occur in this region 5-1.¹⁶⁸

5-1



It has also previously been suggested that dissolution can occur due to the reduction of the irreversible oxide Equation 5-2. This has been well documented and is thought to be due to the difficulty in removing oxide from the crystalline structure.¹⁷⁴

5-2



The results in Figure 48 show a larger ECSA loss for PdIrAu/C after 1000 cycles than PdIr/C and at first look, this does not correlate with the ICP-MS results. The ECSA experiments were completed only as an indication and ICP-MS is a much more reliable technique due to fewer assumptions, particularly with the elements studied here. However previous reports of Ir inhibiting the absorption of hydrogen by Pd may explain the higher ECSA of PdIr/C.^{175 176} If this is the case then as Ir is dissolved from the PdIr/C, the remaining Pd will absorb more hydrogen creating a retention of ECSA which is erroneous.

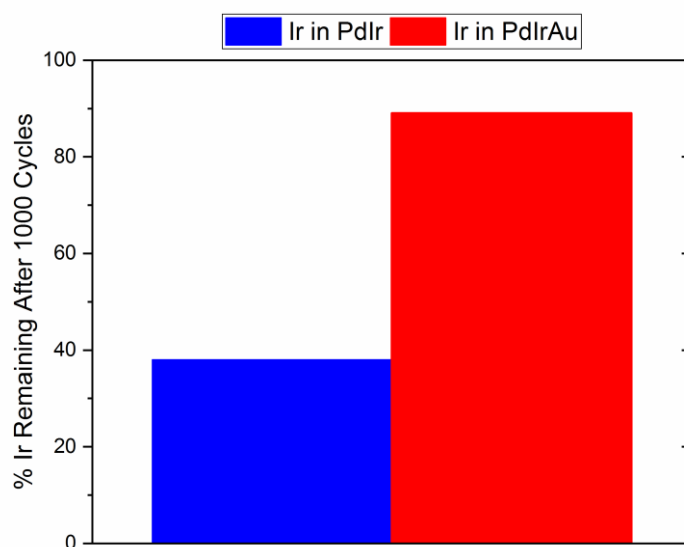


Figure 52 - Graph indicating the percentage of Ir remaining in the catalyst particles after AST cycling.

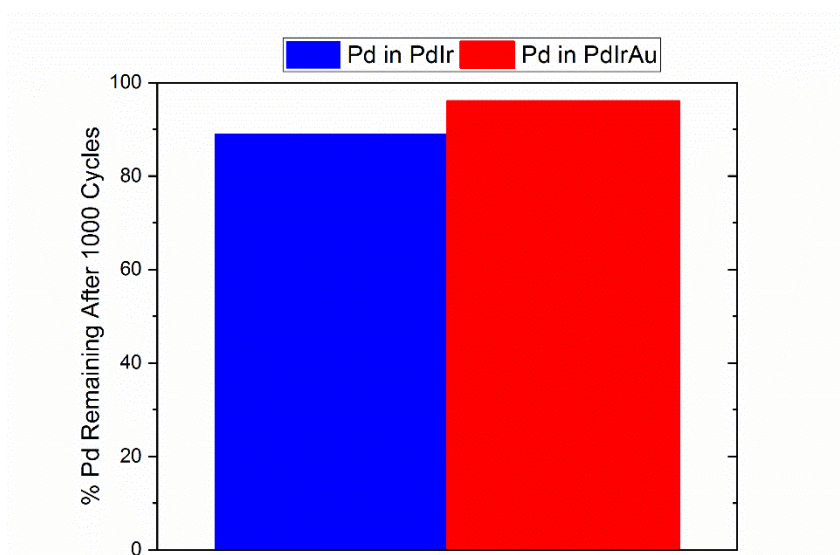


Figure 53 - Graph indicating the percentage of Pd remaining in the catalyst particles after AST cycling.

This work shows a larger dissolution for Ir than previous papers, however the potential range reported there was higher (1.0–1.6 V) which is the common test method for PEM ORR catalysts.^{177 98} As mentioned earlier this is not a reasonable AST test for an anode catalyst as it has been shown that the potential range the anode catalyst will see, even on start-up and shut-down is between 0 and 1 V.¹³⁷ Cherevko *et.al.* have also shown

that above 1.0 V Ir showed very little dissolution which would also correlate with this difference in results.¹⁷⁷

The ICP-MS results show that by adding Au into PdIr after 1000 cycles there is less degradation, and this is likely due to the higher potential onset of the oxide peak. Figure 51 above shows that in this case the addition of Au into the alloy has moved the oxide peak to a higher onset potential and therefore reducing the main dissolution pathway for Pd, confirming why there is less Pd loss.

5.9. *In-situ* degradation

PdIrAu/C applied to an MEA as the HOR catalyst was assessed by *in-situ* testing within a Scribner 850e single cell test stand. The MEA was produced and the test conditions used were as described in Section 3.5. PdIr/C was also applied to an MEA and tested in the same way to provide an assessment of how the addition of Au into the alloy changes the performance and stability with real fuel cell conditions.

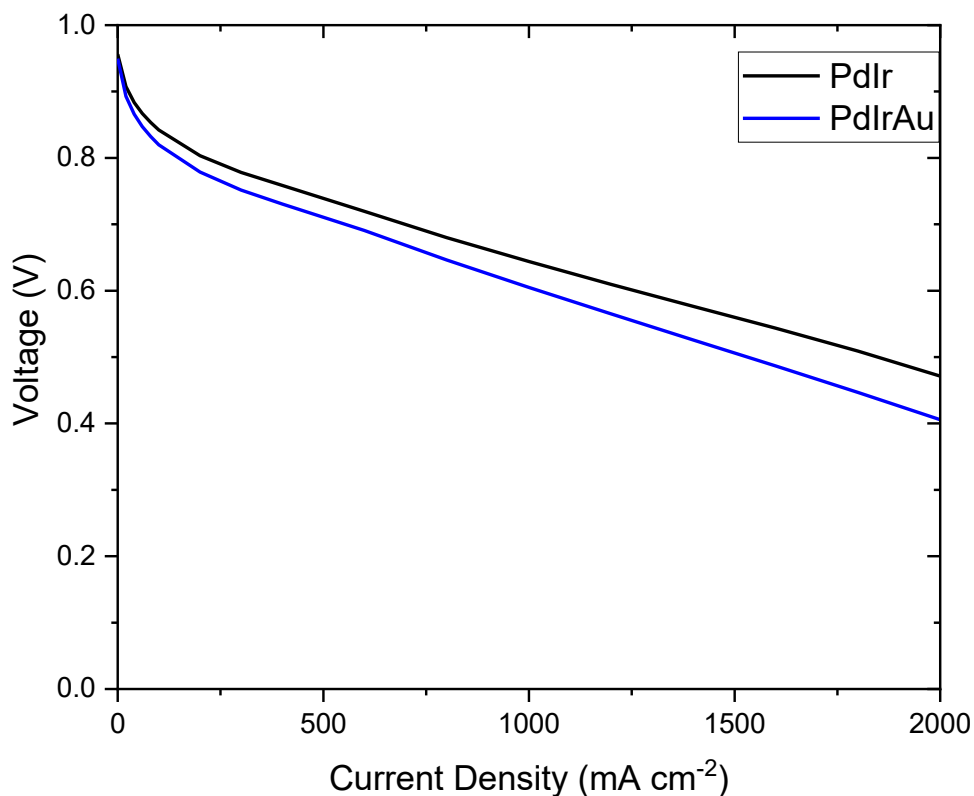


Figure 54 - Initial polarisation curves for PdIr/C and PdIrAu/C taken after cell break in conditions

The initial polarisation curves taken after the fuel cell break in periods are shown in Figure 54. Both have acceptable OCV values with the PdIr/C catalyst performing better in the initial measured polarisation curve, with a higher OCV and final voltage at 2 A cm⁻². A higher current density at 0.6 V, which is the typical working voltage of a cell, can also be seen.

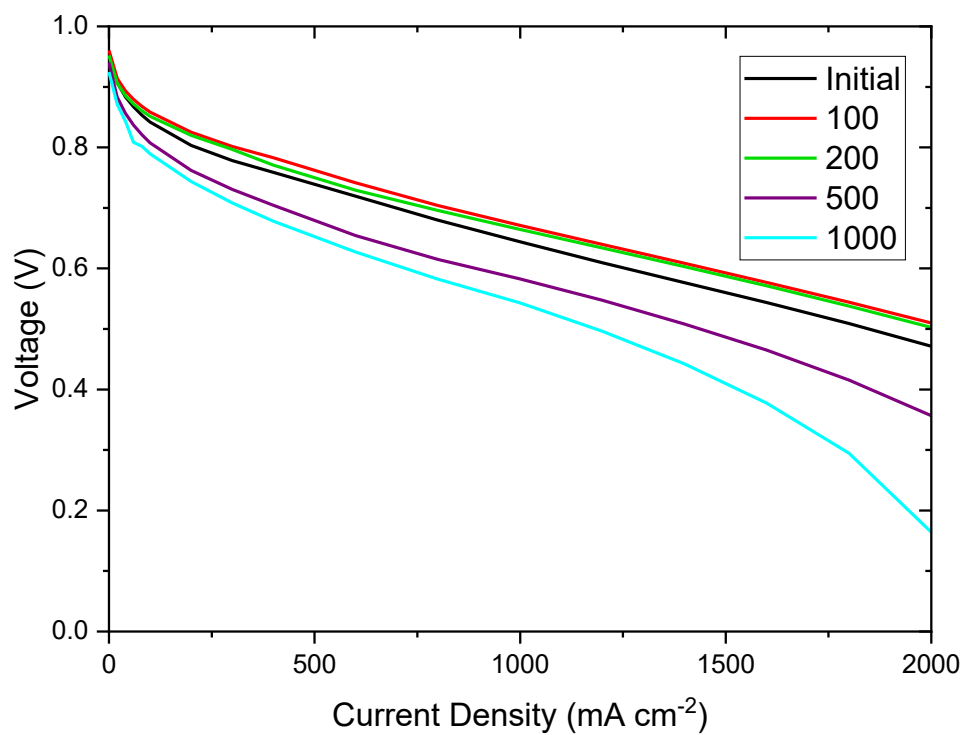


Figure 55 - Polarisation curves after AST cycling of PdIr/C

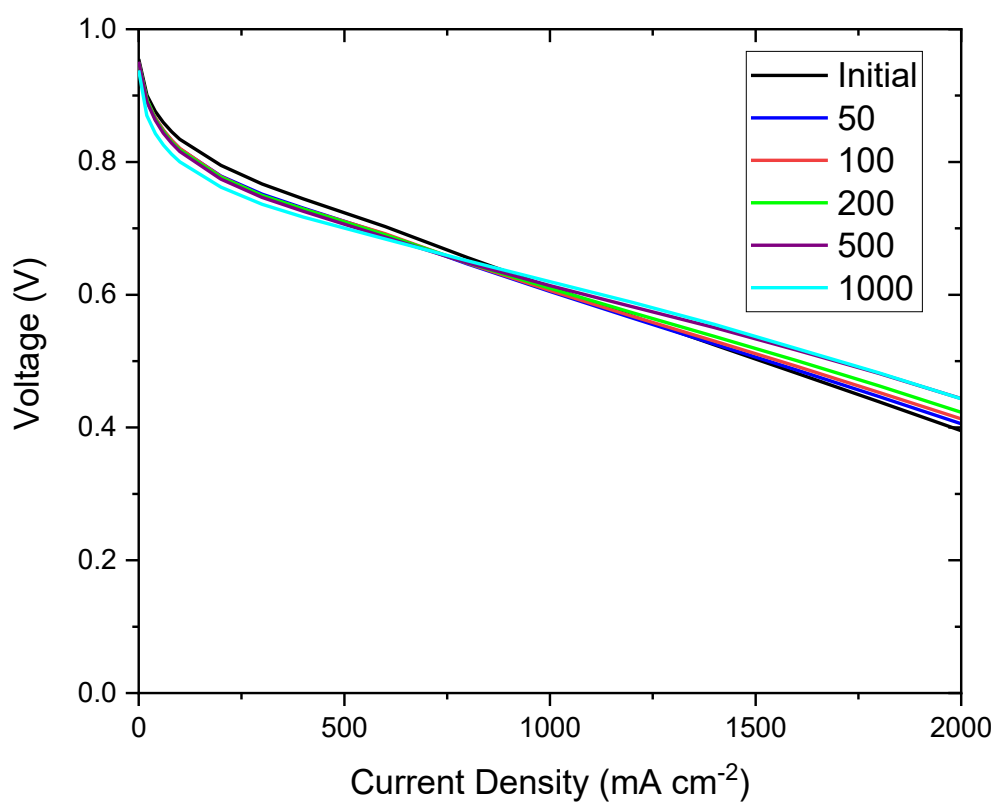


Figure 56 - Polarisation curves after AST cycling of PdIrAu/C

The PdIr/C catalyst performs well in the initial test and following 100 AST cycles, where the catalyst improves, this is assumed to be due to further 'bedding in' of the catalyst due to improvements in the interactions between the catalyst layer and the membrane and GDL. After 200 ASTs there is a small decrease from the previous polarisation curve measured, though this is only slight. After 500 ASTs the polarisation curve is significantly decreased which indicates a degradation of the catalyst due to stability. Further degradation is seen after 1000 ASTs and the polarisation curve drops to well below 0.4 V for the first time, below this potential would provide poor results in a fuel cell and testing is often stopped once this potential is realised.

In contrast to the loss in activity of the MEA shown in Figure 55 by PdIr/C, Figure 56 shows no such decrease in activity but actually the opposite and an increasingly improving polarisation curve from current densities above 750 mA cm⁻². The increasing number of AST cycles continually significantly improves the polarisation curves until 1000 AST cycles which has a very similar curve to that measured after 500 ASTs indicating the point where the 'bedding in' has reached its optimum point. The polarisation curve measured after 1000 cycles has lower values than the initial polarisation curve until around 1000 mA cm⁻² where the curves crossover and the AST polarisation curve has higher values. At lower current densities the losses potential are due to activation losses, though neither of the MEAs showed drastic losses to suggest pin holes in the MEA and the high OCV measurements point to well-made MEAs and lack of issues in the test set up. Losses at higher current densities (>1000 mA cm⁻²) are due to ohmic losses. The improving polarisation curve in this area supports the 'bedding in' theory as resistances due to restriction of ionic and electronic flow are reduced.

Figure 57 shows the comparison of the polarisation curves produced by the two catalysts after 1000 AST cycles.

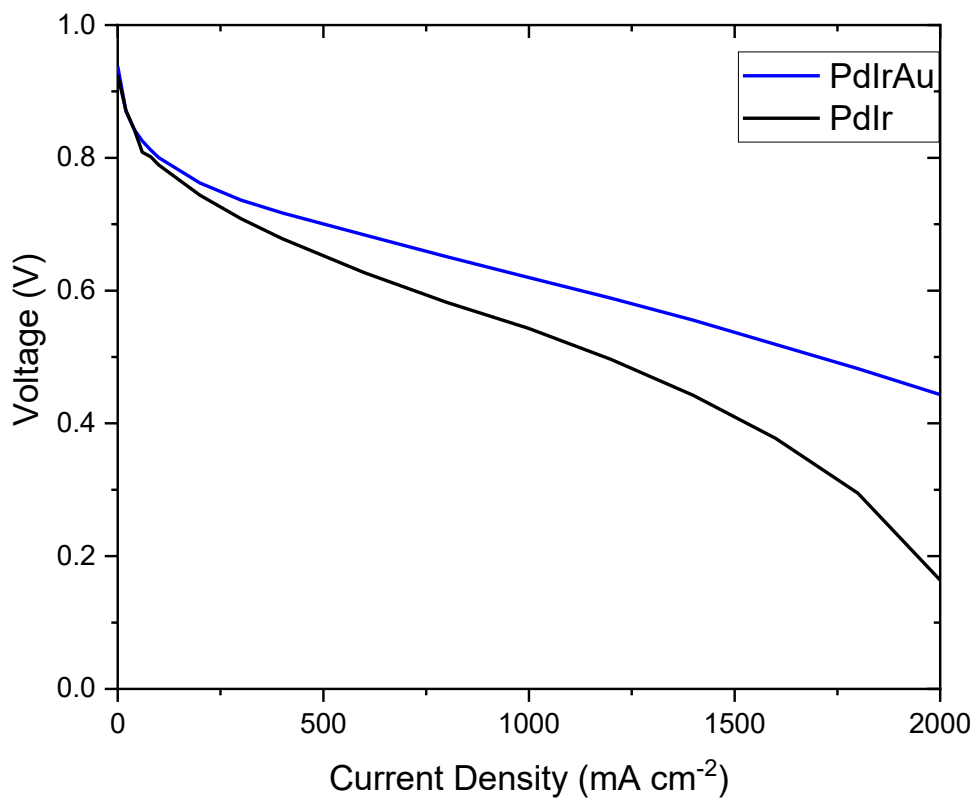


Figure 57 - Polarisation curves after 1000 ASTs for PdIr/C and PdIrAu/C taken after cell break in conditions

Table 11 - Summary of *in-situ* tests comparing the initial polarisation curves with those measured after 1000 ASTs.

	OCV (V)	Current density at 0.6 V (mA cm ⁻²)	Final voltage at 2000 mA cm ⁻² (V)
Initial polarisation curve of PdIr	0.956	1200	0.471
Initial polarisation curve of PdIrAu	0.950	1000	0.406
Polarisation curve of PdIr after 1000 cycles	0.925	700	0.164
Polarisation curve of PdIrAu after 1000 cycles	0.938	1100	0.443

Table 11 shows the increase of all values for the PdIrAu/C after 1000 ASTs and the reduction of all values for PdIr/C. PdIrAu/C provided a 37% better polarisation curve after 1000 cycles than PdIr/C and a voltage over 0.4 V at 2000 mA cm⁻² allowing the continued use of the MEA at this high current draw, whereas PdIr/C drops well below 0.4 V which is the value at which the MEA would stop being used. Additionally, at 0.6 V, the voltage at which a fuel cell is commonly held at the PdIrAu provides a 36% higher current density compared with PdIr after 1000 ASTs. The *in-situ* tests clearly show an improved stability when adding Au in to the PdIr/C binary catalyst, confirming the results of the *ex-situ* testing.

5.10. Discussion

Although similar in many ways to Pt, palladium is known to have a faster dissolution rate, widely regarded to be because of its reactions with oxygen, such as its higher oxide formation and oxygen absorption into its outer lattice layers playing a large part in its dissolution. Previous work has shown that Au does not start dissolving until potentials above 1.4 V, several pathways for this have been previously suggested though non agreed upon.¹⁷⁸ While elsewhere researchers have shown that by alloying Pd with Au the oxide peak can be moved to higher potentials which reduces the main dissolution pathway for Pd.^{178,179}

5.11. Conclusions and Future Work

A novel ternary HOR catalyst supported on carbon is reported. TEM analysis showed the best annealing temperature out of those tried and the resulting catalyst was characterised. EDX confirmed the presence of each metal and XRD showed the existence of some alloying of the three metals. AST cycles were used to degrade the

catalyst and ICP-MS was used to analyse the supporting electrolyte to determine the amount of dissolved metals, this confirmed the theory that the addition of gold into the alloy would increase the overall oxidation potential of the catalyst and therefore reduce the degradation of the catalyst via the oxidation pathway. The *in-situ* results confirmed this increase in stability as the PdIr/C polarisation curves degraded after 1000 ASTs and the PdIrAu/C catalyst polarisation curves did not. Although the results of this Chapter indicate an alloy and the synthesis method used here has produced alloys when used for binary metal alloys, further study using synchrotron X-ray powder diffraction, SXRPD, (which can provide higher resolution results) could be used to further prove the catalyst is a true alloy as well as improved TEM inspection of particles before and after exposure to potential cycling to ascertain the surface structure of the PdIrAu/C alloy after synthesis and if this is changed by the ASTs.

6. ELECTROLYSER INTRODUCTION WITH SYNTHESIS OF Ni₂P CATALYST

6.1. Introduction

The following Chapter moves away from the hydrogen oxidation reaction and onto the hydrogen evolution reaction found in electrolyzers. This work was supported by PV3 Technologies who manufacture and develop electrochemical materials. Their desire for this project was to assess the use of transition metal phosphides for their use within acid electrolyzers, with an overall aim for a synthesis method which is scalable from laboratory to industry production. This Chapter begins with a general background and small literature review of current catalysts followed by details of current state of the art synthesis methods for Ni₂P and then the method development of a new synthesis method and finally the imaging of the catalyst product.

Hydrogen production is required to fuel the hydrogen economy; currently the largest proportion of industrial hydrogen production is through steam reformation, which unfortunately relies on the very fossil fuels from which we are trying to move away. However, electrolysis offers the potential for a more environmentally friendly method of hydrogen production, particularly when run on renewable electricity. Currently electrolysis is primarily used for industrial applications where it has a clear cost advantage; an example of this is in the food industry in Eastern Canada, which takes advantage of the hydroelectric plants in the area. In 2007 it was reported only 4 % of global hydrogen production is produced by electrolysis.¹⁸⁰ Water splitting through electrolysis in industry has traditionally used alkaline based electrolysis mainly because of low investment costs which are due to the use of non-PGM metals as electrocatalysts and low cost electrolyte.¹⁸¹ Alkaline electrolyser cells (AECs) have

been used in industry for over a century and have proven lifetimes which are profitable and satisfactory for continuous operation.¹⁸² Most electrolyzers used in industry are run at high current densities, which also requires a high operating voltage because of kinetic losses. Costs are incurred by running at high voltages, however they are offset by the smaller electrolyser size gained from running at high current densities.¹⁸³ To reduce the Ohmic losses caused by running at high current densities a highly conductive electrolyte is required. As H_3O^+ and OH^- are highly conductive, an electrolyte with a large amount of either of these is ideal hence, highly acidic or highly basic conditions are preferred. Although alkaline electrolyzers have proven their worth, this work will focus on acid-based electrolyzers. An expert elicitation paper recently published indicated that from the top three types of electrolyzers, polymer electrolyte membrane electrolysis cell (PEM-EC), alkaline electrolysis cell (AEC) and solid oxide electrolysis cells (SOEC), experts believed PEM-EC to be the most dominant in our energy future providing hydrogen for not only use in fuel cells but for the Power-to-Gas industry too.¹⁸⁴

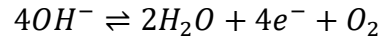
Table 12 - Electrolysis cell types and their common attributes

Fuel Cell Type	Acronym	Operating Temperature	Electrolyte	Charge Carrier
Alkaline	AECs	<80°C	KOH or NaOH	OH^-
Solid Oxide	SOECs	>700°C	Ceramic	O^{2-}
Polymer Electrolyte Membrane	PEMECs	<80°C	Nafion	H^+

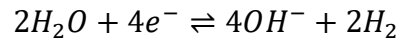
6.1.1. Alkaline electrolysis cells (AECs)

As mentioned above AECs have so far been preferred in industry and they may be scaled depending on the hydrogen demand (from 0.5 to 800 N m³ h⁻¹).¹⁸⁵ The liquid electrolyte used is KOH or NaOH (25–30 wt% in conditions found in most AECs) and the hydroxyl charge carrier ions formed at the cathode, migrate to the anode where the anode reaction takes place.

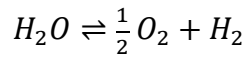
6-1



6-2



6-3



A diaphragm is used in AECs in the electrolyte, in the centre of the cell to separate the gases. It is a microporous material (pore sizes <1µm) which allows the transport of water and hydroxyl ions and so must have high ionic conductivity, corrosion resistance in alkaline media and high permeability to water.¹⁸⁵ Asbestos was initially used as the diaphragm material though no longer due to safety issues and NiO is a good alternative with different fabrication methods used to control its structure and thickness.¹⁸⁶ IrO₂ and RuO₂ would both be the most applicable catalysts for the AEC but these oxides are not stable in alkaline media and therefore typically Ni, Co, Fe and even Pt activated C are used.¹⁸⁷

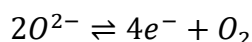
Although AECs are widely used they have lower efficiencies than PEMECs thought to be due to their higher cell resistance due to both the macroporous electrodes and thick

diaphragm.¹⁸⁵ It has also been shown that state of the art technologies PEMECs have three to five time the current densities of AECs.¹⁸⁸

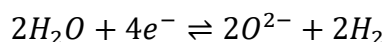
6.1.2. Solid Oxide Electrolysis Cells (SOECs)

The higher working temperatures offer the advantage of a lower electrical energy demand for operating the fuel cell. Steam is used instead of water and is reduced to hydrogen gas and oxide ions which migrate to the anode where they are oxidised, producing oxygen.

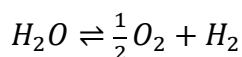
6-4



6-5



6-6

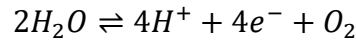


Another advantage to SOECs is their possible use of electrolysis of CO₂ to CO. Materials used are very similar to those in SOFCs (outlined in section 1.2.4) and have therefore advanced due to the research performed in that area. The degradation of cell performance are due to the high operating temperatures and use of steam. Therefore, resistances must be low and to achieve this, materials are very thin. The thin materials increase the time taken to assemble cells which in turn increases production costs, which would need to be reduced in order to achieve successful penetration into the commercial electrolysis market.

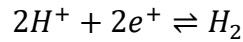
6.2. Polymer electrolyte membrane electrolysis cells (PEMECs)

In PEMECs water is supplied to the anode where it is split into oxygen, electrons and protons. These protons then travel through the membrane to the cathode where they combine to form hydrogen.

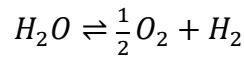
6-7



6-8



6-9



As the electrolysis cell has the reverse chemical reaction to a fuel cell, so then can the efficiency equation be reversed and be given by the higher heating value of the hydrogen (ΔH_{HHV}) produced divided by the electrical energy input:

6-10

$$\eta = \frac{\Delta H}{\Delta G} = \frac{286}{237} = 121\%$$

Though heat (48.6 kJ of energy) is also required to split water, as this is not included in the above Equation the efficiency is artificially high.¹⁸⁹ The theoretical voltage under standard conditions is also the same as in a fuel cell, 1.229 V, though electrolysis cells do not run at this voltage. Opposite to a fuel cell which runs under its theoretical voltage, electrolyzers run well above, around 1.6–2.0 V to drive the kinetics of the electrolysis reaction. The heat required in PEMECs is generated from the resistance from electrical and ionic flows within the cell and therefore, instead of 237 kJ of

electrical energy required; it is actually 286 kJ to split water. Increasing the theoretical voltage to 1.48 V. At this voltage excess, all heat will be used in the reaction, though operating cells are above this and so produce excess heat. Efficiencies of electrolyzers are often quoted using different calculation methods, it is important to standardise the efficiency calculation worldwide to enable fair assessment and comparison of electrolyser projects across the world to ensure the most successful are taken forward.

6.2.1. Components

The components of the electrolyser cell are shown below in Figure 58. PEMECs were initially produced in the 1960's by General Electric to be used as an alternative to AEC due to their improved cell efficiencies and flexible operation and higher gas purities.¹⁹⁰ PEMECs also provide high current densities and voltage efficiencies, good load range and quick system response which allows the flexible operation.¹⁹⁰ By 1973 they were already providing cell lifetimes of 15,000 hours without high performance degradation, using Pt and Ir as catalysts.¹⁸⁸

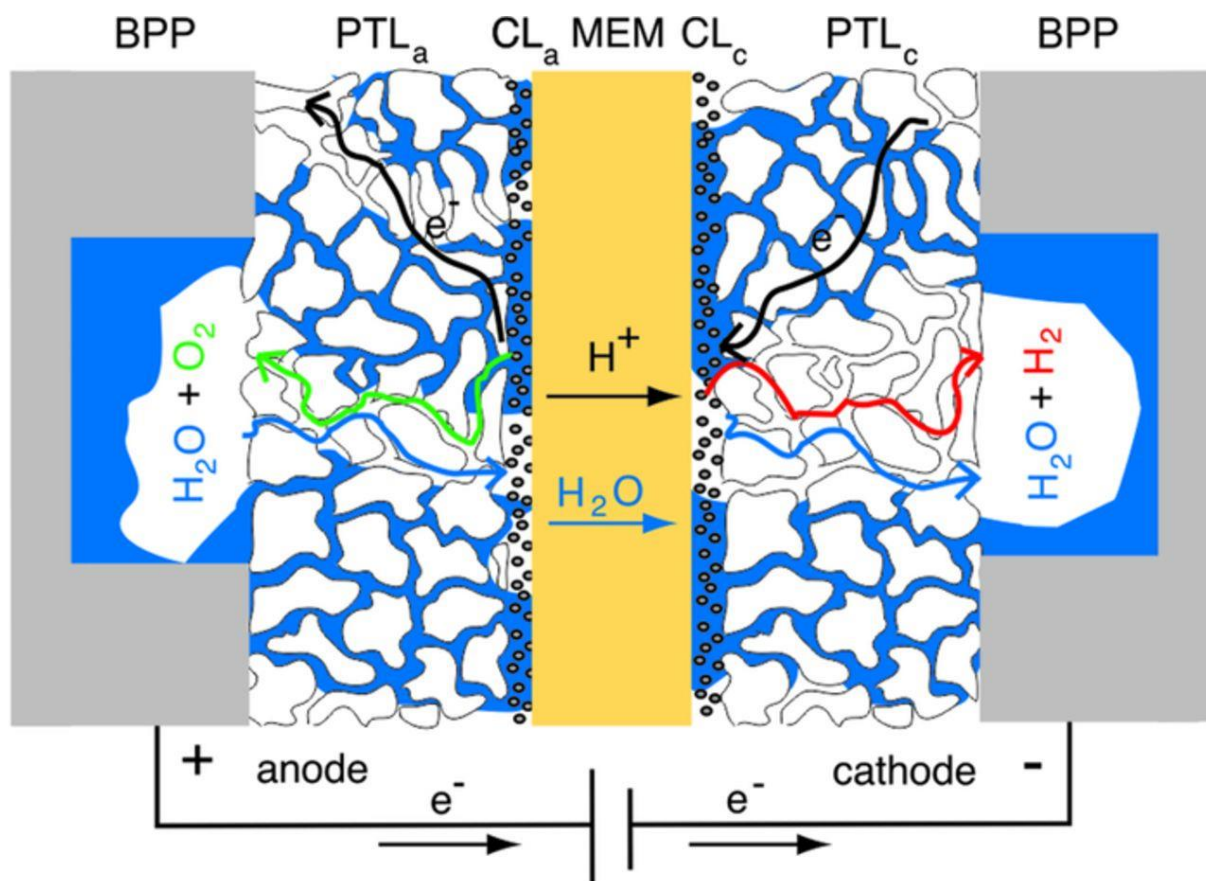


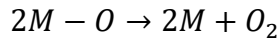
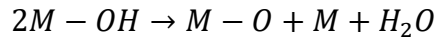
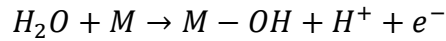
Figure 58 - The cross section of a PEM electrolyser cell, showing the components where the porous transport layers (PTL) are the electrodes. Reprinted from Journal of The Electrochemical Society, Ugljesa Bbic *et al.*, Critical Review – Identifying Critical Gaps for Polymer Electrolyte Water Electrolysis Development, 164, 4 F387-F399, 2017.¹⁸¹

Although a PEMEC is formed of all the same components, which are typically found in a fuel cell, the materials used are very different. This is due to the higher potentials used, which are corrosive to carbon materials, therefore the catalyst support, GDL and bi-polar plates must be made from metallic materials. Typically the catalyst layers are applied to the membrane, before metallic meshes are applied to provide support and electrical conductivity.¹⁹¹ Additional Nafion solution layers have also shown improved stability and performance when added to the solid Nafion before catalyst layer addition.¹⁹² The membrane used is still commonly a perfluorosulphonic acid polymer such as Nafion, Flemion and Fumapem typically with thicknesses of between 100–200 μm to provide a low Ohmic drop.¹⁸⁶

6.2.2. OER

As with FCs the oxygen reaction dictates the efficiency of the EC as it has larger over potential losses compared to the HER. This high anodic potential combined with the acidity of the membrane, mean the catalyst is typically a noble metal. It is still the best compromise between stability and performance when used as the anode catalyst.¹⁹³ The reaction mechanism of the OER is still not fully understood and this has led to difficulties in creating a catalyst that is optimised for its use. Kinetic studies and DFT calculations have produced different reaction mechanisms but none have yet been validated by experimental results.¹⁹⁴ The kinetic method suggested the oxide path below which can also be validated by a Tafel slope of the Ru catalyst, though, it could also be ascribed to other steps and so the debate goes on in literature.¹⁹⁵

6-11

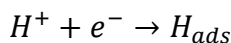


6.2.3. HER

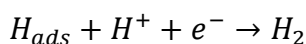
In alkaline media the HER is impeded and the exchange current densities on common catalysts are around two orders of magnitude less than in an acidic environment.¹²³ Though in the acidic environment of PEMEC the HER is the less difficult reaction and so a larger selection of materials may be used as catalysts. The reaction mechanism is similar to the HOR but in the opposite direction. It begins with the Volmer step

followed by either the Heyrovsky or Tafel step. At low H_{ads} coverage the Heyrovsky step is more likely and at high H_{ads} coverage the Tafel is more likely.¹⁹⁶

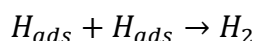
6-12



6-13



6-14



The analysis of a Tafel slope obtained from experimental analysis can indicate which of these steps is dominant (120, 40 and 30 mV dec⁻¹ for the reaction steps Volmer, Heyrovsky and Tafel respectively).¹⁹⁷

A good HER catalyst is one with a low Tafel slope and high exchange current density. The overpotential is the difference between the measured experimental potential and the thermodynamic reduction potential and this can also be used as a measure of a good electrocatalyst, the lower the better.¹⁹⁶ There are not DOE or EU standardised testing for EC electrocatalysts and typically chronoamperometry is used to analyse the degradation where the voltage is held for a long duration. ICP-MS can also be used to give an accurate analysis of durability.¹⁹⁸

6.3. Common Catalysts

The acidic environment provided by the membrane means that noble metals are commonly used to prevent the oxidation and dissolution of the catalyst and Pt is the most common used as the hydrogen evolution reaction (HER) catalyst. The cost of a catalyst can be made up of two parts, the 'hard' cost which is determined by the type

of metal used, for example noble metals which are scarce and which have many other applications in industry will have high 'hard' costs, which are liable to fluctuations due to market changes. There are also 'soft' costs, which are much more stable as they are down to the synthesis method, which stems from, the cost of energy to heat the reaction, the vacuum atmosphere required, or the use of hazardous reactants. It is important to consider these costs when planning for scale up from lab to larger scale catalyst production. There can also be an environmental impact in demanding production processes and therefore synthesis methods, which reduce required temperatures and improve safety, are required. Platinum has the highest catalytic ability for the HER of all metals and the only improvements come from optimising in a nanoparticle system.

6.4. Alternative catalysts

Some transition metal catalysts are known to have high HER activity though low stability in the acidic environment, one method explored to improve this stability is combining it with other elements. The move to non-PGM was facilitated initially by Parsons who studied the HER reaction providing the theoretical basis, followed by Nørskov who utilised DFT to analyse different catalyst options and finding the MoS₂ NPs are promising, due to their binding energy of hydrogen being close to zero.¹⁹⁹²⁰⁰ The research around MoS₂ has steadily grown and the catalysts HER activity, once thought to be modest, has greatly improved. This was sparked by further DFT study showing that particular sites on the MoS₂ is active to the HER and so research has followed, improving initially the amount of these sites and then electrically modifying the sites to heighten their activity.¹⁸³ Following the discovery of the sulphides HER capability, researchers began to look elsewhere, and carbides were found to be a

viable option. MoC supported on CNTs gave lower HER overpotential than and sulphide previously studied.²⁰¹

6.5. Nickel Phosphide Catalyst

Transition metal phosphides date back centuries though their applications were hindered due to their dangerous synthesis methods.¹⁹⁶ In 2005 as MoS₂ was discovered to be a good catalyst for HER via DFT, so too was Ni₂P. Liu *et al.* showed that Ni₂P has better activities over Pt and Ni and they surmised this was due to the strong bonding of H-Ni in the Ni₂P which causes a poisoning of the surface which increases the HER activity.²⁰² The theory of the creation of Ni₂P came from combining the activities of hydrogenase enzymes with the solid surfaces of common FC catalysts. Combining Ni and P can provide both ligand and ensemble effects. The Ni-P bond creation both stabilises the Ni 3d levels and has a small charge transfer, giving a ligand effect. The ensemble effect caused by P actually reduces the overall active sites, which benefits the HER catalysis by reducing the poisoning effects of S.²⁰² Finally the addition of P can also improve the stability, as the metal is thermodynamically less favourable and because the phosphate formed on the surface during oxidation can protect the transition metal within the whole range of electrolyser potential regions.²⁰³ Ni₂P has the hexagonal crystal structure seen in Figure 59.

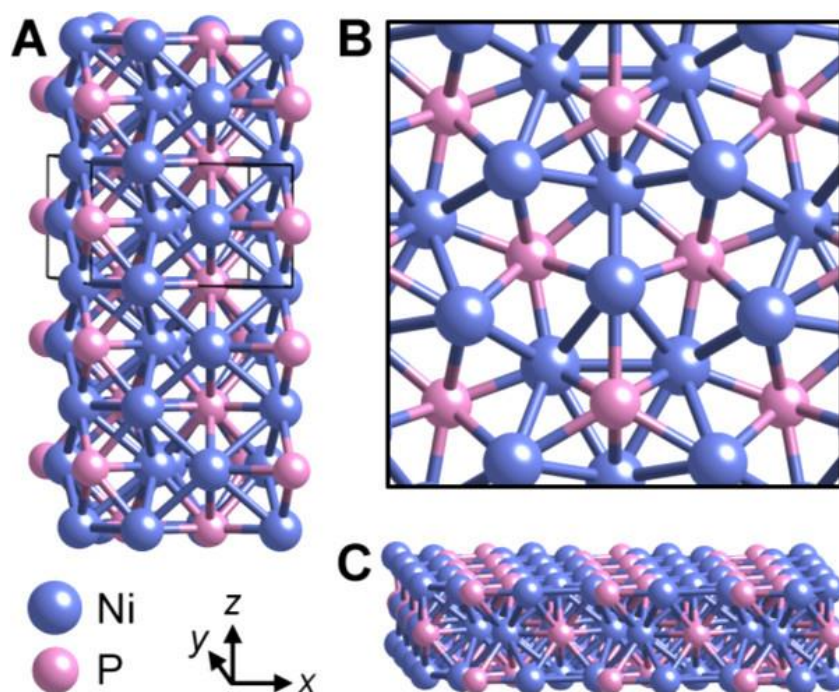


Figure 59 - Crystal structure of Ni₂P A) four stacked unit cells, B) top down view of (001) surface and C) side view showing the (001) surface. Reprinted with permission from Nanostructured Nickel Phosphide as an electrocatalyst for the Hydrogen Evolution Reaction, Popczun, E. J. *et al*, J. Am. Chem. Soc, 2013, 135, 9267-9270. <https://pubs.acs.org/doi/10.1021/ja403440e> Copyright 20013 American Chemical Society.²⁰⁴ Reader note – further permissions related to the material excerpted should be directed the ACS.

WP, MoP and CoP are other phosphide catalysts which have shown promising results for the HER.^{205,206,207} The combination of Co and P is a promising one and experiments have shown that a higher content of P increases both activity and stability by trapping H⁺ during the HER.²⁰⁸ The common method of doping provided by electrodeposition does not create a metal phosphide but rather a phosphorous doped transition metal with P levels below 15 at %, this level of P does not provide the advantages of actual metal phosphides, demonstrating that the synthesis method must be considered to produce the optimum end result.²⁰³

6.6. Motivation

The electrocatalyst cost in PEMECs is reportedly <13% of the overall electrolyser expense, even when using costly noble metals, though this still could be prohibitive to the overall commercialisation of PEMECs and so cost optimisation and availability of components are an interesting area of study.¹⁸³ Therefore this work focuses on the HER catalysts in acidic media without precious metals. The desired characteristics for HER catalysts are durability, efficiency and that it is cost effective. The catalytic ability can be measured by the exchange current density as this shows the rate moving between H^+ and H_2 at equilibrium.

6.7. Standard method

The standard synthesis method is a solution phase method which utilises tri-n-octylphosphine (TOP) as a source of phosphorous. It has previously been suggested the C-P bond in TOP can only be broken above 300 °C which would allow metal phosphides to be produced.¹⁹⁶ Though it has now been shown that the onset of phosphorous insertion into the nickel lattice begins as low as 150 °C.²⁰⁹ Suggesting a lower temperature for the production of Ni_2P nanoparticles is feasible. The use of TOP at high temperatures requires caution due to the possibility of the decomposition of phosphine leading to liberation of phosphorous, which is highly corrosive and flammable. Because of this risk the reaction is carried out under vacuum and argon atmosphere to provide air free conditions.²⁰⁴ Octadecene is and other organics such as octyl ether are used as solvents due to their high boiling points, required for the reaction. Nickel (II) acetylacetonate is the most common nickel source used along with

a capping agent, such as oleylamine. These reagents are also commonly used in the production of Co₂P nanoparticles.

6.8. Method development of Ni₂P Synthesis

Table 13 summarises the successive steps taken in method development to create a successful synthesis method before elaboration of these steps in following pages.

Table 13 - Steps taken during synthesis method development

Requirement	Initial approach	Implemented improvement
Step 1 - Safety	Creation of synthesis area inside fume hood, including signage to prevent others from using fume hood at same time.	Safety catches applied to fume hood area to prevent unnecessary opening during synthesis operation.
Step 2 - Vacuum	Application of vacuum to neck of round bottom flask.	Application of vacuum to top of Liebig condenser to allow improved insertion of reactants into vessel.
Step 3 - Argon atmosphere	Procurement and insertion of Argon gas bottle and line into laboratory.	No further improvements required.
Step 4 - Condenser	Use of existing lab Liebig condenser to provide condensing of hot vapours back into reaction vessel.	Larger length and diameter Liebig condenser to allow for excess vapour produced in synthesis.
Step 5 - Vessel size	Use of round bottom flask of dimensions applicable to heating mantle and neck dimensions suitable for attachments	Increased size of round bottom flask to reduce pressure and prevent escape of vapour to surroundings.
Step 6 - Temperature	Utilising a heating mantle with high temperature capability.	Use of an oil bath considering oil properties.

The initial method used for the synthesis of the Ni₂P particles used a three neck round bottom flask (50 mL) containing borosilicate stir bar fitted with a thermometer adapter, Liebig condenser and a gas inlet. Due to the hazardous materials used, the synthesis was performed in a fume hood with no other experiments taking place at the same time with warnings placed on the fume hood and a child lock in place on the fume hood to

prevent unnecessary opening and exposure. Before sealing the flask Nickel (II) acetylacetonate (acac) (0.25 g, 95% purity, 0.98 mmol), 1-octadecene (4.5 mL, 90% purity, 14.1 mmol), oleylamine (6.4 mL, 19.5 mmol) and tri-n-octylphosphine (1.89 mL, 85% purity, 4.4 mmol) were added. The setup was then placed under vacuum and was stirred and heated using a heating mantle (size allowed use of 50 mL round bottom flask) for 1 hour to 120 °C. Stopper in top of Liebig condenser to allow vacuum. The stopper was then taken out of top of Liebig condenser and vessel placed under argon atmosphere (entering via cannular, to base of flask). The solution was heated to 320°C and held there for 2 hours. The heating mantle was turned off to allow slow cooling of the reaction until the solution reached 200 °C. The reaction was cooled quickly to room temperature by removing from the heating mantle. The solution was then transferred to a centrifuge tube and centrifuged. The initial synthesis method failed for numerous reasons and the method was adapted over several weeks to obtain the Ni₂P particles. Each of the points below had to be altered due to difficulties in the set up.

The heating mantle used was a small size and could hold at maximum a 50 mL round bottom flask. This along with a small Liebig condenser was purchased to fit the heating mantle. During the heating process, above 180 °C a black vapour was produced from the liquid reactants, this was not contained within the flask and black vapour visibly escaped the reaction vessel via the Quickfit joint. The joints had increased security through silica gel added to the interior of the joint and parafilm applied to the exterior of the joint. Due to the small flask used, the joints were close to the heating mantle causing the parafilm to melt allowing the escape of vapour. The flask and Liebig condenser used were substituted for larger sizes, allowing the correct size of Liebig

condenser meant optimum condensing of the reactant vapour, preventing build-up of pressure, which caused the vapour to escape initially.

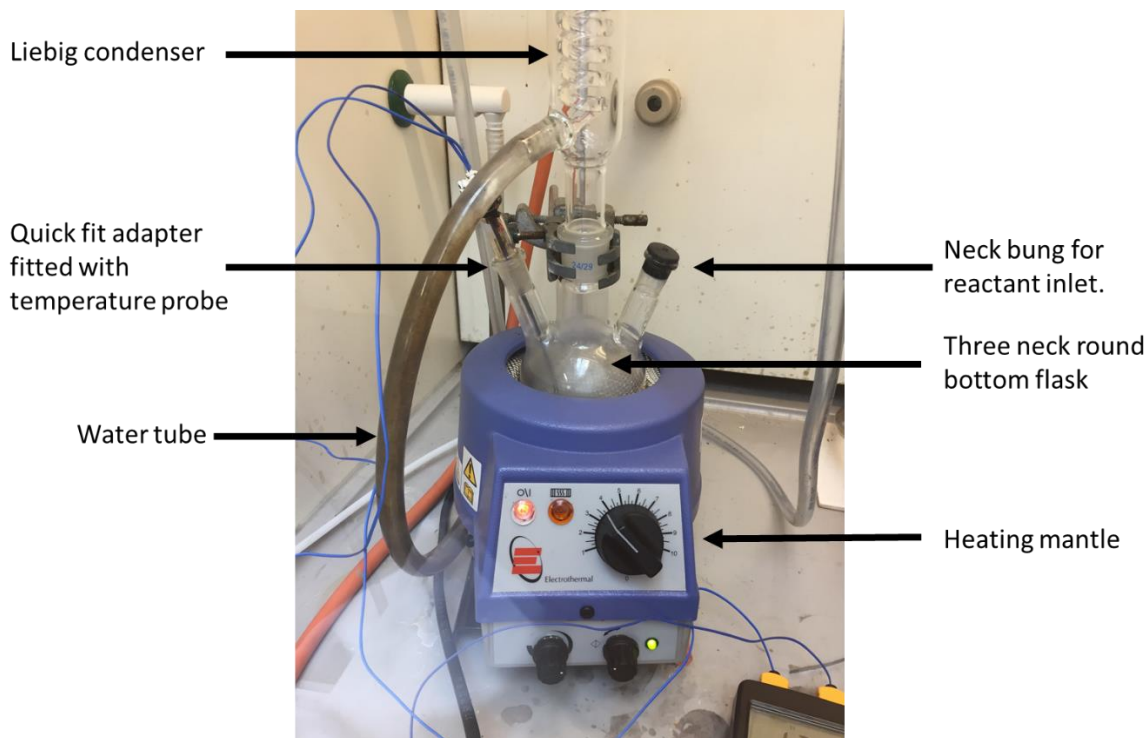


Figure 60 - Set up of synthesis apparatus after step 4 in Table 13 above.

A change to the heating apparatus was also made to an oil bath to allow improved heating of the synthesis. The oil used in the bath was chosen for its high smoke and flash point allowing the temperatures needed for the reaction to be reached. The reaction temperature was reduced in order to evaluate the product of the synthesis at a lower safer temperature. After the changes made the resulting set up could reach 200 °C and this was held for two hours and the resulting particles analysed.

6.9. TEM and HAADF

The synthesised nanoparticles were spherical in shape with an average size of 4 nm as shown by the analysed TEM images. The samples produced were checked in many

locations to ensure the particle sizes were consistent throughout the sample and not only the case in one small area and to give impartial representation of the sample.

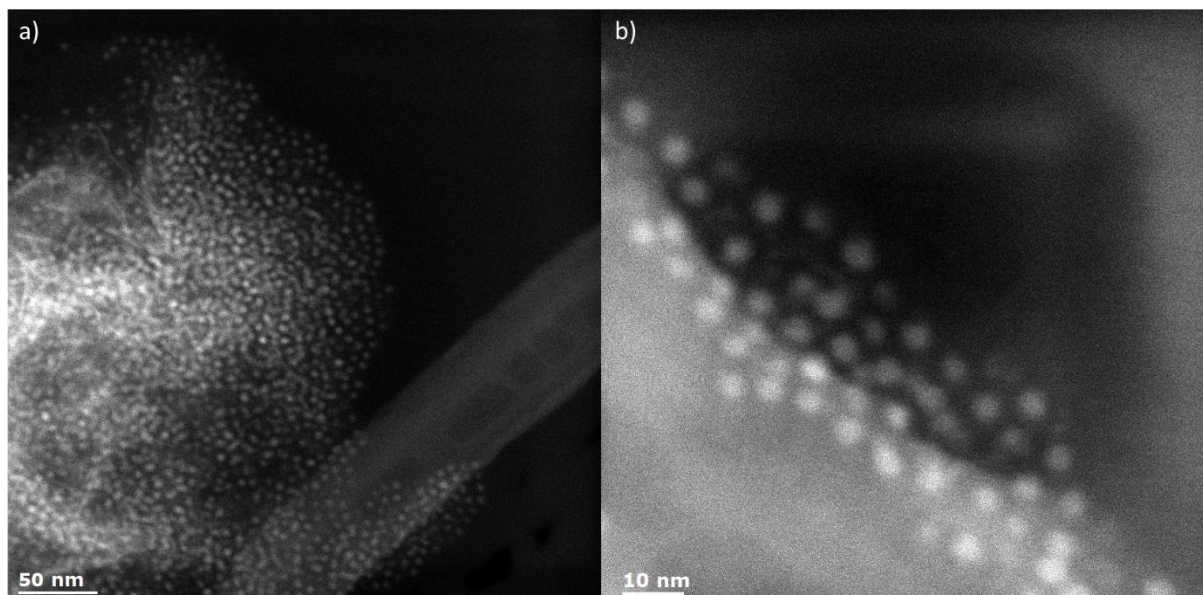


Figure 61 - HAADF images of Ni_2P particles at a) 50 nm zoom and b) 10 nm zoom showing consistent particle sizes throughout the sample.

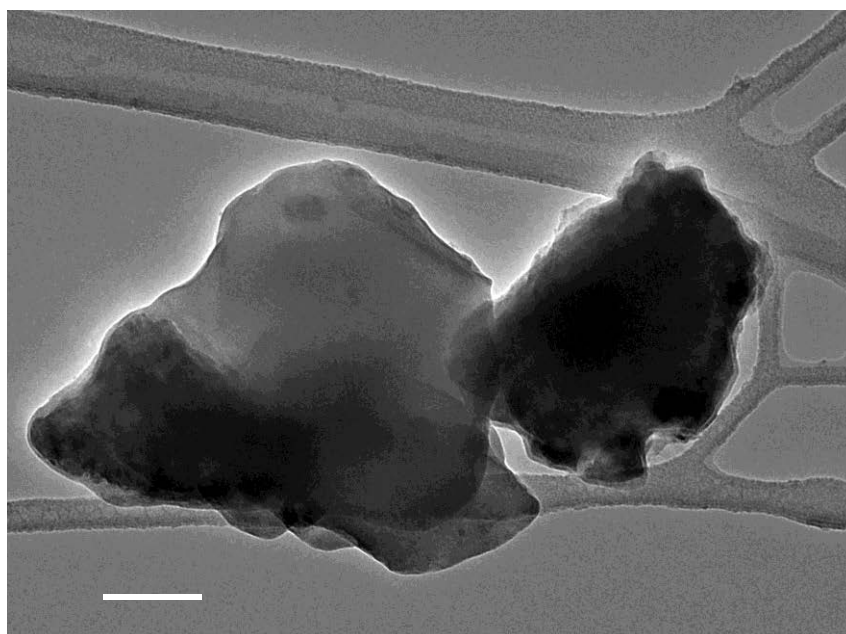


Figure 62 - TEM image of commercial bulk Ni_2P particles were imaged for reference against the synthesised Ni_2P nanoparticles.

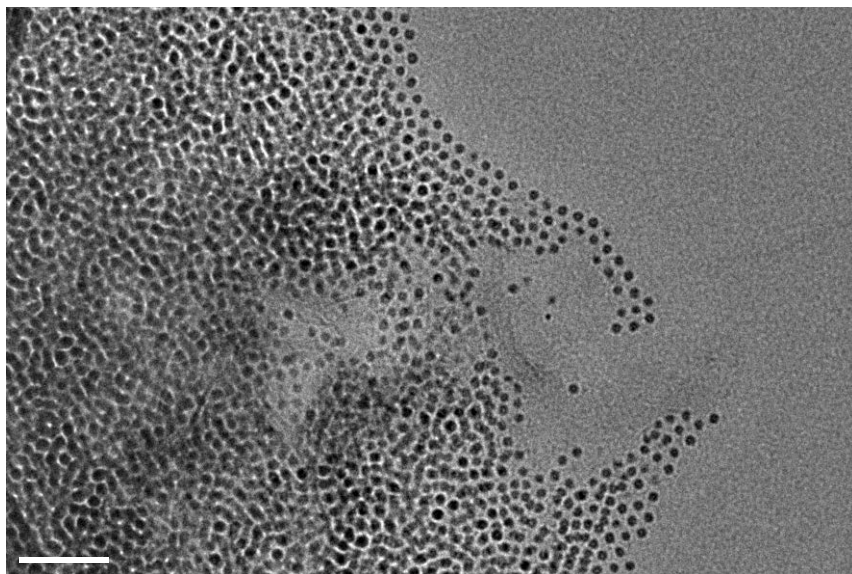


Figure 63 - TEM image at 50 nm zoom showing well dispersed Ni_2P nanoparticles. On the left side of the image the particles are well defined, and their spherical shape is clear.

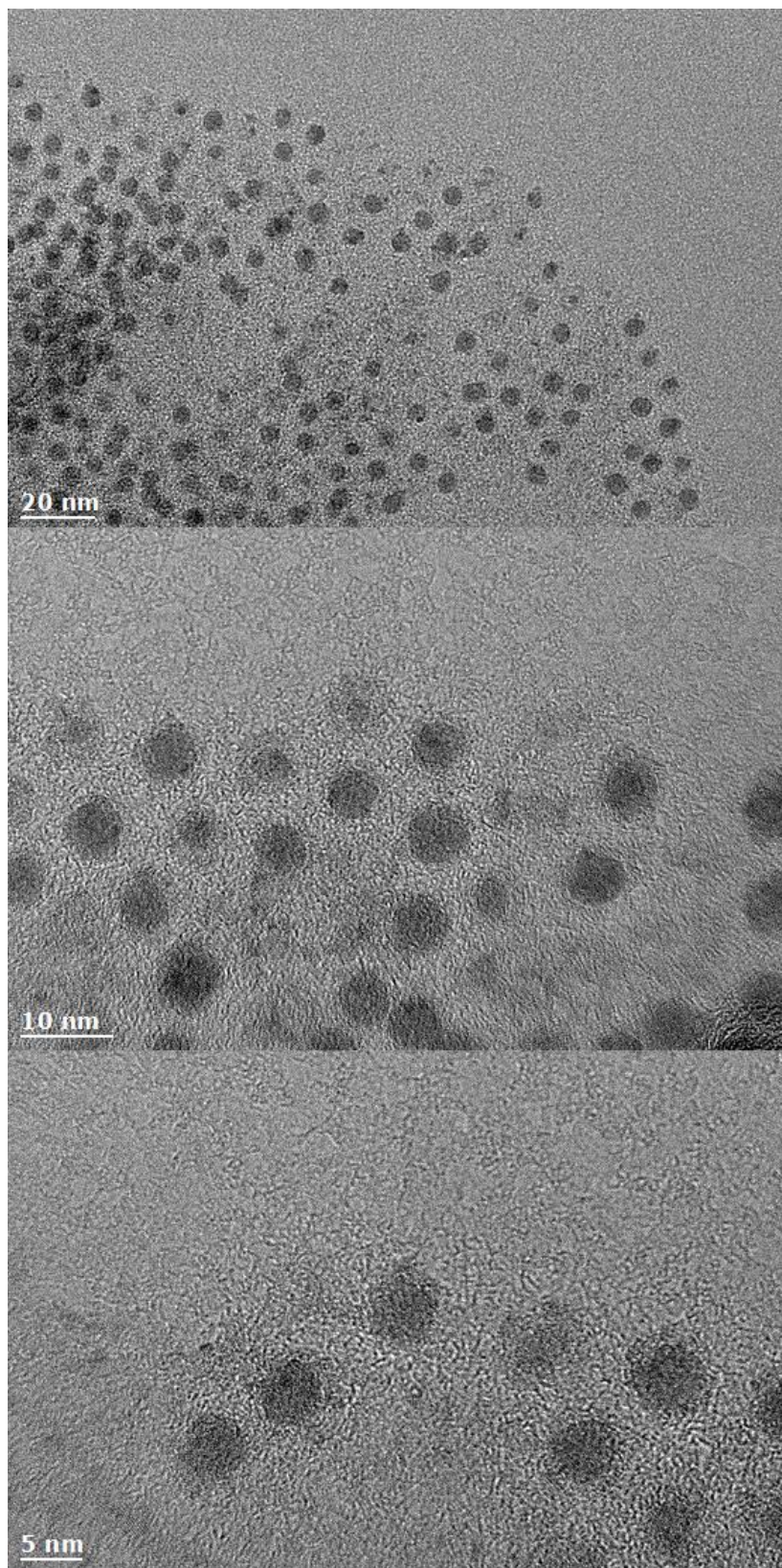


Figure 64 - TEM image at a) 20 nm zoom, b) 10 nm zoom and c) 5 nm zoom showing well dispersed Ni_2P nanoparticles.

The particles sizes were measured from numerous TEM images taken in different areas of the sample to ensure the particle sizes were consistent throughout the sample. The ImageJ automatic measurement technique could not be used as incorrect particle sizes were found, the contrast between the particles and the background was not high enough and particles, which are clear to the eye in the images, were not picked up by the software. Therefore, each particle was individually measured by the straight-line technique. This involves measuring the scale bar within the image with precision allowing pixel sizes to be given a real-world dimension; the particles could then be measured by creating straight lines within the software. This produced improved particle size measurements and showed the particle sizes to be 4 nm spheres.

6.10. EDX mapping

EDX as a quantitative technique is not 100% reliable due to differences in sample areas and overlapping signals from other elements. Therefore, a commercial sample of bulk Ni_2P particles were evaluated to allow a calibration and validate the results further as well as EDX spectra taken in over 10 completely different sample areas. Two of these areas are show in Figure 65 and Figure 66 indicating a correlation of higher Ni and P signal where there are more NPs present.

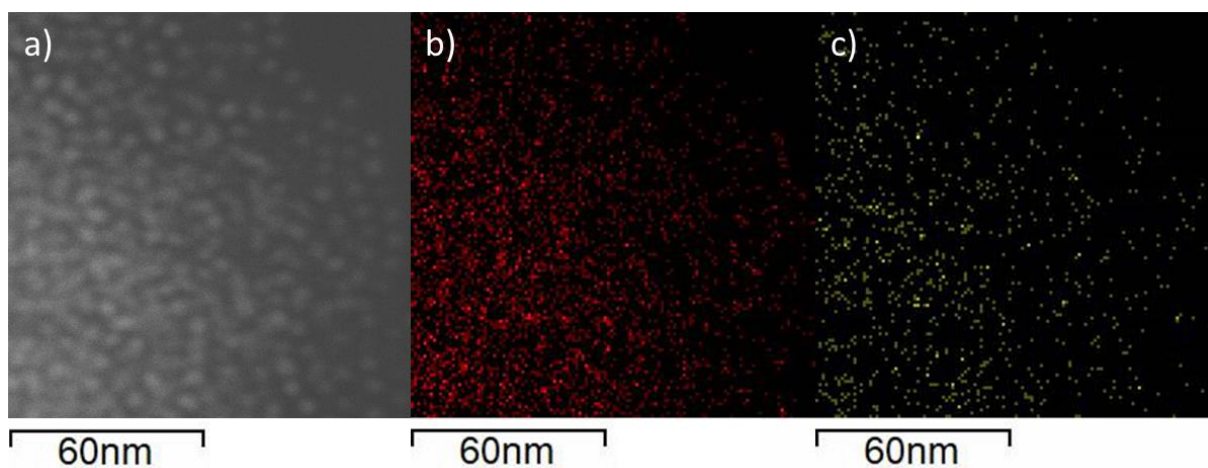


Figure 65 – Sample area with areas without NPs present a) HAADF image of nanoparticles b) EDX map showing red dots for Ni c) EDX map showing red dots for P.

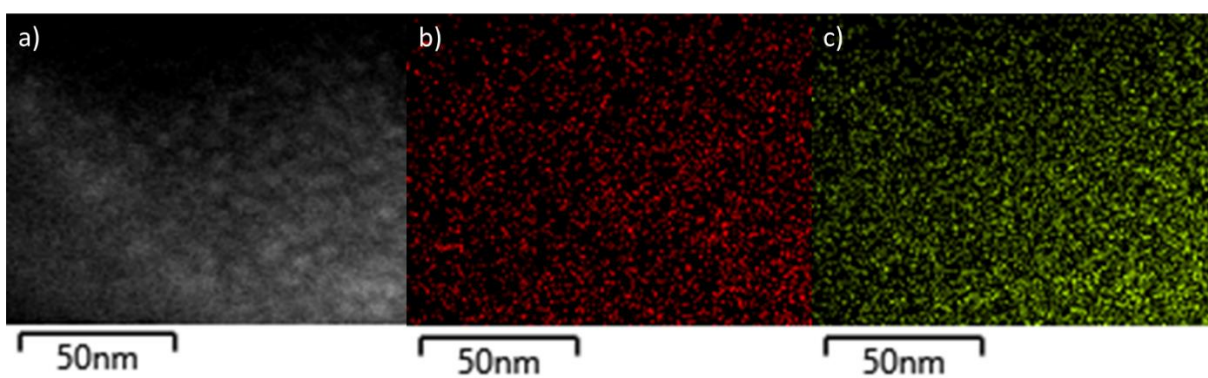


Figure 66 - Concentrated sample area of NPs a) HAADF image of nanoparticles b) EDX map showing red dots for Ni c) EDX map showing red dots for P.

Figure 65 has an atomic ratio P:N ratio of 29:71 and Figure 66 has a P:N ratio of 35:65, both of which are in the expected region of a 1:2 ratio indicating indeed Ni_2P particles were produced by the synthesis method.

6.11. ICP-MS

As well as degradation analysis, ICP-MS is commonly used for quantification of elements in a sample. If the sample is in powder form, it must first be digested by placing in a mixture of hydrochloric acid and nitric acid, which is then sonicated at 90 °C for 1 hour. This produces volatile species and so must be kept in a HPDE vial with

tight closing lid. Before analysis, this sample should be diluted to produce a 2% nitric acid solution. A calibration curve is created from standards to compare the sample to; these are in the ppm range 0–100ppm. As the results depend on this calibration curve it is vital that all elements under analysis are as close to the ppm limit as possible and should be repeated until an optimal calibration curve is obtained. Phosphorous is difficult to detect with ICP-MS due to the silicon matrix interfering with $^{31}\text{P}^+$ which is the only isotope of P. The prepared sample and calibration curve showed this interference was the case with the Ni_2P samples under study as all readings relating to P were incorrect as can be seen in Table 14.

Table 14 - ICP-MS calibration measurements of Ni and P

Sample No.	Aim (ppm)	Ni (ppm)	P (ppm)
1	0.1	0.076	-0.094
2	0.5	0.534	-0.042
3	1	0.862	-0.059
4	5	5.066	-0.354
5	10	10.321	-0.774
6	50	53.222	-6.247
7	100	98.314	98.450

Therefore, ICP-MS could not be used in the analysis of the Ni_2P particles and could not be used to confirm the EDX quantification.

6.12. XRD

Analysis of the Ni_2P particles provided large broad peaks in the Ni and P regions and were difficult to distinguish from the background, though the peaks were in the correct places, showing qualitatively that both Ni and P were present. Repeated experiments were not able to provide improved results and it was surmised that the very small size

(around 4 nm) of the unsupported particles meant that reliable results could not be obtained and a higher resolution XRD would be required to obtain better XRD analysis.

6.13. AFM

The nature of TEM images being 2D can result in mistakes when considering a 3D structure from them. When considering the (001) axes of a cubic crystal this may look square through the TEM image, but a (111) axes may show a hexagonal shape.²¹⁰ Therefore, it is important to validate the two-dimensional technique, though SEM, which would typically be applied here due to its scanning nature, cannot be used, as the nanoparticles are too small. Therefore, AFM was utilised to show the three-dimensional shape and confirm the spherical morphology.

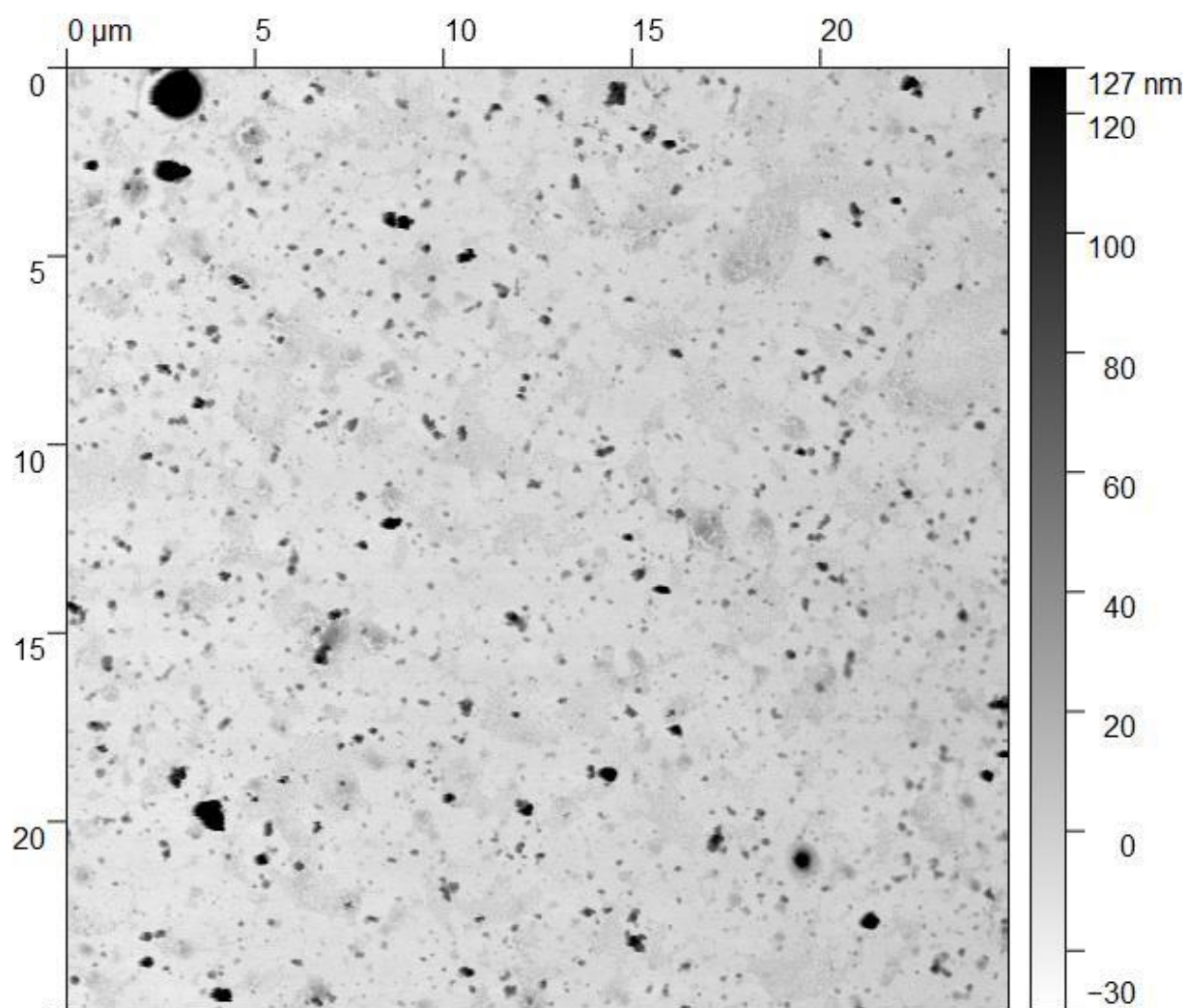


Figure 67 - AFM image of Ni₂P nanoparticles in 2D before further manipulation of the image in Gwyddion software.

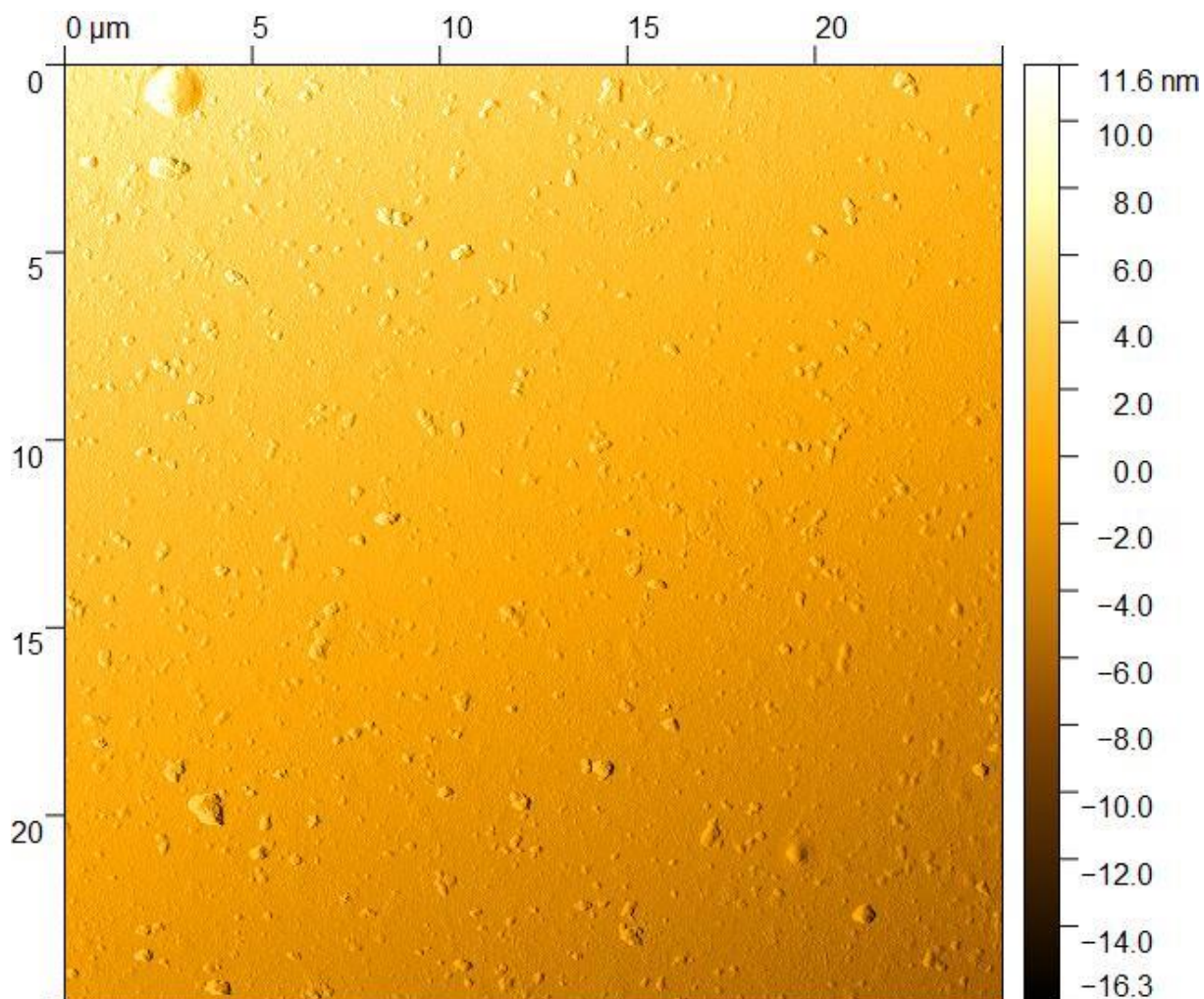


Figure 68 - AFM image showing the amplitude of particles in 3D, agglomeration of particles occurred in the sample production process for the AFM technique.

The image in Figure 68 confirms in three dimensions the spherical nature of the Ni_2P nanoparticles, which was suggested by the earlier TEM images. It also shows agglomeration of the NPs into much larger particles, though this is likely due to the sample preparation method of the AFM. The larger particles were not evident in TEM imaging and the measurement of the small Ni_2P particles in the Gwyddion software confirmed the particle sizes to be around 4 nm.

6.14. Conclusions and future work

After numerous changes to the synthesis method to adapt the equipment to that available and applicable for the lower temperature sought, Ni_2P particles were produced. TEM combined with EDX and AFM confirmed the synthesis of Ni_2P particles at a lower temperature than that applied in common synthesis methods.

Although this Chapter proved the creation of a new catalyst production technique in the Fuel Cell labs, further work is recommended to assess and further improve the newly implemented method. This work should be carried out on the catalyst described in this Chapter before it's application to other catalysts which also require specialist synthesis techniques. Future recommended work is required to assess the catalytic ability of the promising Ni_2P particles produced at a lower temperature than previously shown in literature. *Ex-situ* testing of the HER overpotential and the resulting Tafel plot can provide a measure of their catalytic ability toward the HOR. Their stability could also be measured by CV sweeps similar to those performed in the HOR catalyst testing but at lower potential values (+ 0.22 and -0.23 V). Improved XRD analysis would also be required to show the crystallinity of the particles. A thorough work plan to fully assess this catalysts ability and degradation is described in the next Chapter.

7. CONCLUSIONS AND FUTURE WORK

Electrochemical devices, such as PEM fuel cells and electrolyzers are a viable source to providing energy with reduced harmful emissions, paving the way to a cleaner energy future. High costs and durability remain a barrier to the technologies, and the electrocatalysts used in their production are a key area for development, to improve the overall technology, due to their high cost and vital role in producing a highly functioning system. This work aims to improve electrocatalysts in two key areas:

- Formation of PdIrAu as a novel anode catalyst in PEMFCs.
- Development of a safer synthesis method of Ni₂P nanoparticles for the cathode reaction in PEMECs.

Whilst continually aiming to produce and implement test methods directly applicable to the catalyst under investigation and its relevant end use.

Following the introduction and method descriptions discussed in Chapters 1 and 2 respectively an in-depth analysis of an updated test method is presented in Chapter 3. A comparative study was conducted to investigate the importance of the methods used to prepare MEAs for fuel cells. The current, widely reported procedure involves adding an extra layer of Nafion onto commercial GDE when producing MEAs to be tested *in-situ* within a fuel cell rig, it has been shown that comparable results are achieved without undergoing this step. The Chapter highlights the importance of updating methods along with material development, as in this case the commercial GDE no longer requires addition of this Nafion layer. X-ray CT showed this addition increased the smoothness of the electrode and reduced the surface area, *ex-situ* MEA testing

also showed there was no longer an improvement to the polarisation curve through the addition of the Nafion layer.

The methods described in the Chapter 2 which were used throughout the body of work went through development periods to ensure they were the most applicable to the catalyst they were testing. Chapter 3 highlights the importance of the thought processes and steps taken to ensure thorough examination of the catalysts produced, a further example can be found in the difficulties encountered whilst trying to produce a method, which accurately assessed the catalysts of interest's ECSA, before finally obtaining the ICP-MS method which accurately showed the stability of the catalyst.

Chapter 4 provides a comprehensive literature review on the benefits of palladium when used as a catalyst combined with other elements as a binary metal catalyst. Followed by a discussion around the decision of addition of Au into the PdIr catalyst.

The synthesis and analysis of the novel PdIrAu catalyst was presented in Chapter 5. Different annealing temperatures from literature were used to ascertain which provided the better catalyst. TEM showed that at annealing at 600 °C produced a catalyst with highly coarsened particles but at 400 °C the catalyst was not coarsened, only agglomerated and therefore this catalyst was used for further testing. PdIr/C was used as comparison throughout the Chapter and ICP-MS showed the addition of Au into the catalyst provided the desired increase in stability. The addition of Au reduced the loss of Pd by 7% and Ir by 51%. The *ex-situ* testing also showed that after 1000 AST cycles in a fuel cell environment the PdIrAu catalyst as a whole had 37% better polarisation curve than PdIr. Further work which would complement this Chapter would be to incorporate a high surface area carbon as a support which has seen success in

literature and is likely to produce a less agglomerated catalyst. Unfortunately, the prices of the metals used in the catalyst changed drastically during the course of the research.

Table 15 - Price fluctuation of key elements studied in HOR catalyst for this work, prices for Pt, Pd and Ir were taken from Johnson Matthey and converted from troy oz to oz, Au prices were taken from Statista.com.

Date	Platinum (\$ oz⁻¹)	Palladium (\$ oz⁻¹)	Iridium (\$ oz⁻¹)	Gold (\$ oz⁻¹)
September 2016	966	630	596	1326
January 2020	910	2072	1358	1560

The dates in the Table above were chosen to highlight the large fluctuation in cost from the beginning of the PhD studies to the end. In September 2016 the Amalyst business model for a PdIr catalyst provided a 36% cost reduction compared to Pt, whilst providing similar catalytic ability towards the HOR. The addition of Au into the PdIr catalyst would still have provided a 13% cost saving compared to pure Pt, again whilst providing similar HOR catalytic activity with the added benefit of improved stability. The initial aim of this process was to prove the theory and follow on with alternative elements to gold which could provide this stability improvement but at a lower cost compared with Au. The increase in price of Pd, Ir and Au compared with the reduction in price of Pt meant that both PdIr and PdIrAu catalysts no longer provide a cost reduction compared to Pt alone, reducing the viability of the catalysts in commercial settings. The fluctuation in costs of PGM metals over time highlights the difficulty in producing a catalyst based on price though there is still evident value in production of novel catalysts.

Chapter 6 discussed the background of PEMECs and the background of HER electrocatalysts. which highlighted the need for Ni_2P electrocatalysts as well as a safer method for their synthesis, with current methods using toxic reagents and typically a challenging synthesis. A lengthy method development was completed to produce an applicable synthesis method, including a constant oxygen free environment with high temperatures in the UoB lab which had not been successfully done before. Characterisation and imaging showed the method successfully produced the particles with the desired size and morphology (shown by TEM) as well as the expected Ni:P ratio (shown by EDX). Though further work is required to fully assess the synthesised particles ability and stability toward the HER, the following Table outlines these next steps and further discussion follows.

Table 16 - Suggested step by step work plan to further characterise and assess catalytic ability.

Steps toward successful catalyst production	Method	Details
Step 1 – Larger batch production	Synthesis method	Repeat synthesis method from last batch, to ensure consistency in synthesis while producing specimens for further testing.
Step 2 – Initial check for catalytic activity	Ex-situ electrochemical	Perform linear sweep voltammetry (LSV) on electrocatalyst deposited onto GC electrode within a three-electrode cell.
Step 3 – Ensure removal of capping agents	Heat treatment before further electrochemical testing	Heat treat the sample under reducing atmosphere by application to Ti foil, before ex-situ electrochemical testing.
Step 4 – Physical characterisation	X-ray photoelectron spectroscopy	Analysis of high-resolution spectra to confirm Ni:P in correct ratios as shown by EDX.
Step 4 – Particle size confirmation	XRD	Repeated XRD analysis to confirm ratios and particle sizes provided by EDX and TEM respectively.
Step 5 – Surface area determination	BET	Surface area and pore volume of catalyst should be determined by BET.
Step 6 – Degradation	Ex-situ electrochemical AST's	Initial assessment of appropriate electrochemical technique for catalyst type followed by ex-situ accelerated stress tests.

Further set up of *ex-situ* electrochemical testing would not be required, as the test set up discussed in the methods Chapter can be adapted to analyse the performance of the HER catalyst as shown previously in this laboratory by Escalera López *et al.* who produced Ni-MoS₂ electrocatalysts in the UoB School of Physics and Astronomy and tested in the Centre for Hydrogen and Fuel Cell Research.²¹¹

Ni₂P particles of spherical morphology as opposed to nanorod shape have previously shown to have higher HER activity.²¹² Therefore when considering results from *ex-situ*

experiments the TEM and AFM images showing this synthesis method produces spherical particles should be kept in mind.

To further prove the synthesis method is successfully providing the expected catalyst at lower synthesis temperatures, heat treatment analysis should be carried out. Electrochemical tests should be carried out on both a heat-treated catalyst and a non heat-treated catalyst to ensure the capping agents are not impacting the catalytic performance. Using a similar method to that previously published, Ti foil should be used as a working electrode onto which the electrocatalyst is drop cast onto, rather than a GC electrode, which cannot undergo heat treatment easily due to its size.²⁰⁸ The catalyst on Ti foil is then heated in a reducing atmosphere of 5 % H₂ in Ar for 1 h. After 1 h cooling in the same atmosphere, the sample should then be tested electrochemically with the same method above. A comparison sample should also be produced in the same way without heat treatment. This is to allow direct comparison between the heat-treated sample and the non heat-treated sample without any electrochemical measurement differences which are not attributed to the catalyst, as these may be produced by a change in working electrode.

X-ray photoelectron spectroscopy (XPS) can confirm the chemical states of the catalyst produced and show the Ni:P ratios are as expected from the TEM and EDX results already obtained as well as identify the presence of oxides and sulphides on the nickel particles.²¹³ XPS depth profiling with Ar⁺ etching should also be utilised to provide the distribution of Ni and P throughout the NPs.²¹³

XRD can be used to identify particle sizes, as shown in Chapter 6 XRD results can be difficult to obtain clear results from equipment to equipment. Quality results were

obtained for Chapter 5 on a different machine which was unavailable due to flooding for the Ni₂P catalyst and this experiment should be repeated once further catalyst has been produced in the larger batch synthesis in Step 1 in Table 16. The XRD should be measured between 20-90° 2θ with peaks to match with the hexagonal structure expected around 40.8°, 44.7°, 47.5°, 54.4°, 66.4°, 72.6°, 75.0°, 80.5° and 88.9° are attributed to the (111), (201), (210), (300), (310), (311), (400), (401) and (321) crystal phases, respectively.²¹³ Electrochemical surface area measurements are not typically performed on HER catalysts as they would be with HOR catalysts, due to the low potential range applied to these catalysts not being applicable to most commonly used techniques nitrogen adsorption-desorption can be used to measure the Brunauer-Emmett-Teller (BET) surface area and pore volume and size.²⁰⁴ This method has limitations and assumptions which increase the error in the measurement and so care must be taken when considering results and also has lengthy sample preparation times and actual experimental times. This method can be useful to compare different samples produced within a lab to show differences between them, or to confirm surface area calculated from XRD.²¹³

As in described throughout this body of work, test methods should be developed to ensure a catalyst is tested comparably to any benchmark catalysts and also to consider the end use environment of the catalyst. Long lifetimes of electrolyzers show that 1000's of hours of constant operation would be required to show any degradation in a catalyst and therefore accelerated stress tests are required. Degradation testing of HER catalysts varies commonly consisting of repeated CV cycles or chronoamperometry.^{214,215} Recently Bernt *et al.* produced an AST based on real world use of electrolyzers coupled with renewable energy sources which would provide an

intermittent power source.²¹⁶ This AST showed to have higher degrading effects on the catalysts than chronoamperometry ASTs. Both CV and chronoamperometry would be applicable for the Ni₂P particles and both of these AST types should be performed initially in short durations and compared to find the best results before performing long term ASTs which require long durations of experimental and equipment use. A further consideration which should be made when creating ASTs for the Ni₂P catalyst, is the Nafion which can be used as a binder in the electrocatalyst ink to ensure adherence to the working electrode. As shown in the supporting evidence in the paper of Popczun *et al.* Nafion can reduce the degradation effects on a HER catalyst when submitted to ASTs.²⁰⁴

The implementation of the above work would allow the comparison of the Ni₂P catalyst ability toward the HER to be compared to others in literature, as many published Ni₂P catalyst papers do not include *in-situ* testing and instead rely on *ex-situ* electrochemical experiments.²¹⁵ The characterisation of the Ni₂P catalyst in Chapter 6 showed the successful production of Ni₂P particles at a lower synthesis temperature than commonly used. The further analysis tests suggested in this Chapter will indicate the ability of these particles to catalyse the hydrogen evolution reaction.

In terms of future work combining the core themes of this work, there are a number of potential element combinations of those studied, which could provide novel catalysts applicable to numerous electrochemical reactions.

PdIrNi catalyst for the HOR in PEMFCs. Addition of Ni has been shown as a powerful tool in tailoring electrocatalytic properties, and that doping can optimise the H bond strength improving the hydrogen binding energy, which is a crucial part of producing

capable hydrogen electrocatalysts.²¹⁷ Furthermore the Pourbaix diagram for Ni, shown in Figure 69 shows similarly to Au, Ni is not expected to produce an oxide in the relevant pH and potential range for HOR at both room temperature and 100 °C which is around the operating temperature of a PEMFC. This could prevent surface oxides from forming which is a key element for catalyst degradation. Potentially providing an electrocatalyst with improved degradation from the PdIr binary catalyst but at a much lower cost as Ni is consistently around a tenth of the price of gold.

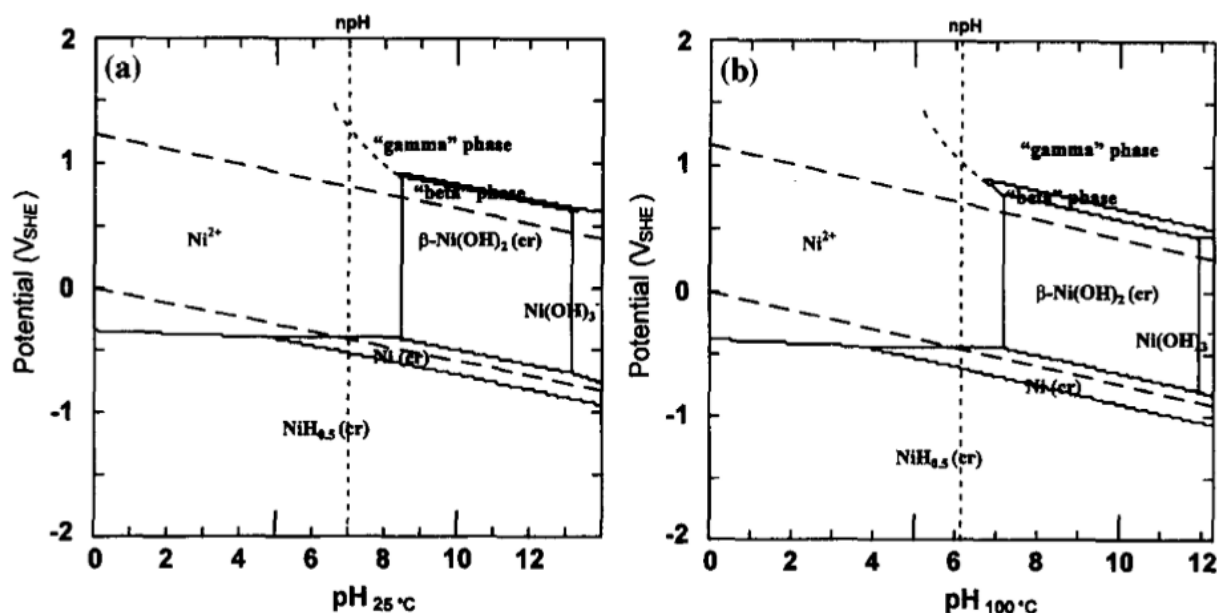


Figure 69 - Pourbaix diagram for nickel at 25 and 100 °C

PdIrP catalyst for the HOR and HER in PEMFCs and PEMECs. The production of metal phosphide from Pd/C has previously shown to have the ability to improve stability against electrochemical degradation testing through ASTs and chemical oxidation of the catalyst support.²¹⁸ Combining these successful palladium phosphide catalyst results with the PdIr/C catalyst reported here has the potential to provide a robust catalyst on many fronts. Due to the current high cost of Pd, alloying with the cheaper

Ir will reduce cost while continuing to provide a catalyst with strong HOR and HER capability. The Table below shows the key benefits of each component.

Table 17 - Benefits of individual components within suggested catalyst

Component	Benefits
Palladium	High catalytic ability toward the HOR and HER with many papers showing these can be improved by alterations of the d-band through alloying with other metals.
Iridium	Second highest catalytic ability towards the HOR and high on the volcano plot for the HER. ²¹⁹
Phosphide	Improve catalyst support degradation and electrochemical degradation. ²¹⁸

The lengthy development and testing times required to produce a catalyst such as those suggested above could be drastically reduced by implementing the synthesis and test methods created within this thesis, specifically aimed at the HOR and HER for PEMFCs and PEMECs

Overall, this thesis produced a successful PdIrAu catalyst toward the HOR with improved stability, as well as a new synthesis method for the HER catalyst Ni₂P, all of which has been underpinned by robust test methods which are now in place for future work.

List of Publications

1. Allerston L.K., Rees N.V. Nanoparticle impacts in innovative electrochemistry. *Curr Opin Electrochem.* 2018;10:31-36.
2. Albrecht T., Horswell S., Allerston L.K., Rees N.V., Rodriguez P., Electrochemical processes at the nanoscale, *Curr Opin Electrochem.* 2018;7:138-145.
3. Allerston L.K., Hodgson D., Gibbs C., Brett D.J.L., Rees N.V., Increased stability of palladium iridium gold electrocatalyst for the hydrogen oxidation reaction in PEM fuel cells, SUBMITTED to *Electroanalysis*.

8. References

1. Wipke K, Sprik S, Kurtz J, Ramsden T, Ainscough C, Saur G. All Composite Data Products: National FCEV Learning Demonstration With Updates Through Jan 18, 2012. 2011.
2. Salameh Z. Renewable Energy System Design. Academic Press; 2014. 201-298 p.
3. Behling NH. Fuel Cells - History of Phosphoric Acid Fuel Cells. In: Fuel Cells. Elsevier; 2013. p. 53–135.
4. Sudhakar YN, Selvakumar M, Bhat DK. Biopolymer Electrolytes for Fuel Cell Applications. In: Biopolymer Electrolytes. Elsevier; 2018. p. 151–66.
5. Srinivasan S, Manko DJ, Koch H, Enayetullah MA, Appleby AJ. Recent advances in solid polymer electrolyte fuel cell technology with low platinum loading electrodes. J Power Sources. 1990;29(3–4):367–87.
6. Campos-Roldán CA, Alonso-Vante N. The Hydrogen Oxidation Reaction in Alkaline Medium: An Overview. Electrochem Energy Rev. 2019;2(2):312–31.
7. Breeze P. Fuel Cells - The Alkaline Fuel Cell. In: Fuel Cells. Academic Press; 2017. p. 23–32.
8. Sørensen B, Spazzafumo G. Fuel Cells. In: Hydrogen and Fuel Cells. Academic Press; 2018. p. 107–220.
9. Merle G, Wessling M, Nijmeijer K. Anion exchange membranes for alkaline fuel cells: A review. J Memb Sci. 2011;377(1–2):1–35.

10. Farooque M, Ghezel-Ayagh H. System design. In: Handbook of Fuel Cells. Chichester, UK: John Wiley & Sons, Ltd; 2010.
11. Li Q, Jensen JO, Savinell RF, Bjerrum NJ. High temperature proton exchange membranes based on polybenzimidazoles for fuel cells. *Prog Polym Sci*. 2009;34(5):449–77.
12. Li X, Faghri A. Review and advances of direct methanol fuel cells (DMFCs) part I: Design, fabrication, and testing with high concentration methanol solutions. *J Power Sources*. 2013;226:223–40.
13. Ravikumar MK. Effect of Methanol Crossover in a Liquid-Feed Polymer-Electrolyte Direct Methanol Fuel Cell. *J Electrochem Soc*. 1996;143(8):2601.
14. Kyung-Won Park, Jong-Ho Choi, Boo-Kil Kwon, Seol-Ah Lee A, Sung Y-E, And H-YH, et al. Chemical and Electronic Effects of Ni in Pt/Ni and Pt/Ru/Ni Alloy Nanoparticles in Methanol Electrooxidation. *J Phys Chem B*. 2002;106(8):1869–77.
15. Song S, Tsiakaras P. Recent progress in direct ethanol proton exchange membrane fuel cells (DE-PEMFCs). *Appl Catal B Environ*. 2006;63(3–4):187–93.
16. Rees N V., Compton RG. Sustainable energy: a review of formic acid electrochemical fuel cells. *J Solid State Electrochem*. 2011;15(10):2095–100.
17. Yu X, Pickup PG. Recent advances in direct formic acid fuel cells (DFAFC). *J Power Sources*. 2008;182(1):124–32.

18. Barbir F. Fuel Cell Basic Chemistry and Thermodynamics. In: PEM Fuel Cells. Second. Academic Press; 2013. p. 17–32.
19. Barbir F. Fuel Cell Electrochemistry. In: PEM Fuel Cells. Second. Academic Press; 2013. p. 33–72.
20. Zhang J, Zhang H, Wu J, Zhang J. Chapter 1 - PEM Fuel Cell Fundamentals. In: Pem Fuel Cell Testing and Diagnosis. Elsevier; 2013. p. 1–42.
21. Shimpalee S, Lilavivat V, McCrabb H, Khunatorn Y, Lee HK, Lee WK, et al. Investigation of bipolar plate materials for proton exchange membrane fuel cells. *Int J Hydrogen Energy*. 2016 Aug 17;41(31):13688–96.
22. Ozden A, Alaefour IE, Shahgaldi S, Li X, Ozgur Colpan C, Hamdullahpur F. Gas Diffusion Layers for PEM Fuel Cells: Ex- and In-Situ Characterization. *Exergetic, Energ Environ Dimens*. 2018;695–727.
23. Van Nguyen T, Knobbe MW. A liquid water management strategy for PEM fuel cell stacks. *J Power Sources*. 2003;114(1):70–9.
24. Longo S, Cellura M, Guarino F, Ferraro M, Antonucci V, Squadrito G. Life Cycle Assessment of Solid Oxide Fuel Cells and Polymer Electrolyte Membrane Fuel Cells: A Review. *Hydrog Econ*. 2017;139–69.
25. Spohr E. Proton generation and transport in the fuel cell environment: atomistic computer simulations. *J Comput Mater Des*. 2007;14:253–8.
26. Zhang J, Zhang H, Wu J, Zhang J. Relative Humidity (RH) Effects on PEM Fuel Cells. In: Pem Fuel Cell Testing and Diagnosis. Elsevier; 2013. p. 201–23.

27. Branco CM. MULTILAYER MEMBRANES FOR INTERMEDIATE TEMPERATURE POLYMER ELECTROLYTE FUEL CELLS. University of Birmingham; 2017.
28. Nakao M, Yoshitake M. Composite perfluorinate membranes. In: Handbook of Fuel Cells. Chichester, UK: John Wiley & Sons, Ltd; 2010.
29. Macauley N, Papadimas DD, Fairweather J, Spornjak D, Langlois D, Ahluwalia R, et al. Carbon Corrosion in PEM Fuel Cells and the Development of Accelerated Stress Tests. *J Electrochem Soc.* 2018;165(6):F3148–60.
30. Antolini E. Carbon supports for low-temperature fuel cell catalysts. *Appl Catal B Environ.* 2009;88(1–2):1–24.
31. Cheng K, He D, Peng T, Lv H, Pan M, Mu S. Porous graphene supported Pt catalysts for proton exchange membrane fuel cells. *Electrochim Acta.* 2014;132:356–63.
32. Park S, Shao Y, Wan H, Rieke PC, Viswanathan V V., Towne SA, et al. Design of graphene sheets-supported Pt catalyst layer in PEM fuel cells. *Electrochem commun.* 2011;13(3):258–61.
33. Imran Jafri R, Rajalakshmi N, Ramaprabhu S. Nitrogen doped graphene nanoplatelets as catalyst support for oxygen reduction reaction in proton exchange membrane fuel cell. *J Mater Chem.* 2010;20(34):7114.
34. Lepró X, Terrés E, Vega-Cantú Y, Rodríguez-Macías FJ, Muramatsu H, Kim YA, et al. Efficient anchorage of Pt clusters on N-doped carbon nanotubes and their catalytic activity. *Chem Phys Lett.* 2008;463(1–3):124–9.

35. Subban C, Zhou Q, Leonard B, Ranjan C, Edverson HM, Disalvo FJ, et al. Catalyst supports for polymer electrolyte fuel cells. *Trans R Soc A*. 2010;368:3243–53.
36. Chen E. Chapter 2 - History. In: Hoogers G, editor. *Fuel Cell Technology Handbook*. CRC Press; 2003.
37. Curnick OJ, Pollet BG, Mendes PM. Nafion®-stabilised Pt/C electrocatalysts with efficient catalyst layer ionomer distribution for proton exchange membrane fuel cells. *RSC Adv*. 2012 Sep 28;2(22):8368–74.
38. Ohi JM, Vanderborgh N, Consultants GV, Ahmed S, Kumar R, Papadimitrakopoulos F, et al. Hydrogen Fuel Quality Specifications for Polymer Electrolyte Fuel Cells in Road Vehicles. 2016.
39. Gasteiger HA, Kocha SS, Sompalli B, Wagner FT. Activity benchmarks and requirements for Pt, Pt-alloy, and non-Pt oxygen reduction catalysts for PEMFCs. *Appl Catal B Environ*. 2005 Mar;56(1–2):9–35.
40. Fuel Cell Technologies Office USD of E. Multi-Year Research, Development and Demonstration Plan - Section 3.4 Fuel Cells. 2017.
41. Barbir F. Main Cell Components, Material Properties, and Processes. In: *PEM Fuel Cells*. Second. Academic Press; 2013. p. 73–117.
42. Peng Z, Yang H. Designer platinum nanoparticles: Control of shape, composition in alloy, nanostructure and electrocatalytic property. *Nano Today*. 2009;4(2):143–64.

43. Chong L, Wen J, Kubal J, Sen FG, Zou J, Greeley J, et al. Ultralow-loading platinum-cobalt fuel cell catalysts derived from imidazolate frameworks. *Science*. 2018;362(6420):1276–81.
44. Shen X, Zhang C, Zhang S, Dai S, Zhang G, Ge M, et al. Deconvolution of octahedral Pt₃Ni nanoparticle growth pathway from in situ characterizations. *Nat Commun*. 2018;9(1):4485.
45. Loukrakpam R, Luo J, He T, Chen Y, Xu Z, Njoki PN, et al. Nanoengineered PtCo and PtNi Catalysts for Oxygen Reduction Reaction: An Assessment of the Structural and Electrocatalytic Properties. *J Phys Chem C*. 2011;115:1682–94.
46. Yoshida T, Kojima K. Toyota MIRAI Fuel Cell Vehicle and Progress Toward a Future Hydrogen Society A New Concept in Flow Field Structure. *Electrochem Soc Interface*. 2015;24(2):45–9.
47. Mizutani N, Ishibashi K. Enhancing PtCo Electrode Catalyst Performance for Fuel Cell Vehicle Application. In: *SAE 2016 World Congress and Exhibition*. 2016.
48. Wang XX, Swihart MT, Wu G. Achievements, challenges and perspectives on cathode catalysts in proton exchange membrane fuel cells for transportation. *Nat Catal*. 2019;2(7):578–89.
49. Wanjala BN, Luo J, Loukrakpam R, Fang B, Mott D, Njoki PN, et al. Nanoscale Alloying, Phase-Segregation, and Core–Shell Evolution of Gold–Platinum Nanoparticles and Their Electrocatalytic Effect on Oxygen Reduction Reaction. *Chem Mater*. 2010;22(14):4282–94.

50. Zaleska-Medynska A, Marchelek M, Diak M, Grabowska E. Noble metal-based bimetallic nanoparticles: the effect of the structure on the optical, catalytic and photocatalytic properties. *Adv Colloid Interface Sci.* 2016;229:80–107.
51. Ferrando R, Jellinek J, Johnston RL. Nanoalloys: From Theory to Applications of Alloy Clusters and Nanoparticles. *Chem Rev.* 2008;108(3):845–910.
52. Okube M, Petrykin V, Mueller JE, Fantauzzi D, Krtil P, Jacob T. Topologically Sensitive Surface Segregations of Au-Pd Alloys in Electrocatalytic Hydrogen Evolution. *ChemElectroChem.* 2014;1(1):207–12.
53. Marković NM, Ross PN. Surface science studies of model fuel cell electrocatalysts. *Surf Sci Rep.* 2002;45(4–6):117–229.
54. Akita T, Taniguchi A, Maekawa J, Siroma Z, Tanaka K, Kohyama M, et al. Analytical TEM study of Pt particle deposition in the proton-exchange membrane of a membrane-electrode-assembly. *J Power Sources.* 2006;159(1):461–7.
55. Wu J, Yuan XZ, Martin JJ, Wang H, Zhang J, Shen J, et al. A review of PEM fuel cell durability: Degradation mechanisms and mitigation strategies. *J Power Sources.* 2008;184(1):104–19.
56. Ascarelli P, Contini V, Giorgi R. Formation process of nanocrystalline materials from x-ray diffraction profile analysis: Application to platinum catalysts. *J Appl Phys.* 2002;91(7):4556–61.
57. Mathias MF, Makharia R, Gasteiger HA, Conley JJ, Fuller TJ, Gittleman CJ, et al. Two Fuel Cell Cars In Every Garage? *Electrochem Soc Interface.* 2005;14(3):24–35.

58. Borup RL, Davey JR, Garzon FH, Wood DL, Inbody MA. PEM fuel cell electrocatalyst durability measurements. *J Power Sources*. 2006;163(1):76–81.
59. Pourbaix M. *Atlas of Electrochemical Equilibria in-Aqueous Solutions*. Second. 1974.
60. Topalov AA, Cherevko S, Zeradjanin AR, Meier JC, Katsounaros I, Mayrhofer KJJ. Towards a comprehensive understanding of platinum dissolution in acidic media. *Chem Sci*. 2014;5(2):631–8.
61. Jovanović P, Šelih VS, Šala M, Hodnik N. In situ electrochemical dissolution of platinum and gold in organic-based solvent. *npj Mater Degrad*. 2018;2:1–4.
62. Nørskov JK, Rossmeisl J, Logadottir A, Lindqvist L, Kitchin JR, Bligaard T, et al. Origin of the Overpotential for Oxygen Reduction at a Fuel-Cell Cathode. *J Phys Chem B*. 2004;108(46):17886–92.
63. Holton OT, Stevenson JW. The Role of Platinum in Proton Exchange Membrane Fuel Cells - Johnson Matthey Technology Review. *Platin Met Rev*. 2013;57(4):259.
64. J. K. Nørskov, J. Rossmeisl, Logadottir A, Lindqvist L, Kitchin JR, Bligaard T, et al. Origin of the Overpotential for Oxygen Reduction at a Fuel-Cell Cathode. *J Phys Chem B*. 2004;108(46):17886–92.
65. Sheng W, Gasteiger H, Shao-Horn Y. Hydrogen oxidation and evolution reaction kinetics on platinum: acid vs alkaline electrolytes. *J Electrochem Soc*. 2010;157(11):1529–36.

66. Shao M. Palladium-based electrocatalysts for hydrogen oxidation and oxygen reduction reactions. *J Power Sources*. 2011;196(5):2433–44.
67. Pronkin SN, Bonnefont A, Ruvinskiy PS, Savinova ER. Hydrogen oxidation kinetics on model Pd/C electrodes: Electrochemical impedance spectroscopy and rotating disk electrode study. *Electrochim Acta*. 2010;55(9):3312–23.
68. Chen S, Kucernak A. Electrocatalysis under Conditions of High Mass Transport: Investigation of Hydrogen Oxidation on Single Submicron Pt Particles Supported on Carbon. *J Phys Chem B*. 2004;108(37):13984–94.
69. Quaino PM, Gennero de Chialvo MR, Chialvo AC. Hydrogen electrode reaction: A complete kinetic description. *Electrochim Acta*. 2007;52(25):7396–403.
70. Kowalczyk P, Savard S, Lasia A. Determination of the adsorption energy distribution function of upd hydrogen on monocrystalline platinum. *J Electroanal Chem*. 2004;574(1):41–7.
71. Burheim OS. Chapter 6 - Electrochemical Energy Storage. In: *Engineering Energy Storage*. Academic Press; 2017. p. 75–110.
72. Bard AJ, Faulkner LR. *ELECTROCHEMICAL METHODS Fundamentals and Applications*. John Wiley & Sons, Ltd; 2001.
73. Garland N, Benjamin T, Kopasz J. DOE Fuel Cell Program: Durability Technical Targets and Testing Protocols. In: *ECS Transactions*. ECS; 2007. p. 923–31.
74. Tsotridis G, Pilenga A, De Marco G, Malkow T. EU HARMONISED TEST PROTOCOLS FOR PEMFC MEA TESTING IN SINGLE CELL

CONFIGURATION FOR AUTOMOTIVE APPLICATIONS; JRC Science for Policy Report. 2015.

75. Schoemaker M, Misz U, Beckhaus P, Heinzl A. Evaluation of Hydrogen Crossover through Fuel Cell Membranes. *Fuel Cell*. 2014 Jun 1;14(3):412–5.
76. Power P. Fuel Cells Move One Step Closer to Powering Airport Ground Support Equipment | FuelCellsWorks [Internet]. 2014 [cited 2015 Jan 29]. Available from: <http://fuelcellsworks.com/news/2014/07/01/fuel-cells-move-one-step-closer-to-powering-airport-ground-support-equipment/>
77. Qin Y, Du Q, Fan M, Chang Y, Yin Y. Study on the operating pressure effect on the performance of a proton exchange membrane fuel cell power system. *Energy Convers Manag*. 2017;142:357–65.
78. Barbir F. Fuel Cell System Design. In: PEM Fuel Cells. Second. Academic Press; 2013. p. 305–72.
79. Stephens I, Rossmeisl J, Chorkendorff I. Toward sustainable fuel cells. *Science* (80-). 2016;354(6318):1378–9.
80. Alazemi J, Andrews J. Automotive hydrogen fuelling stations: An international review. *Renew Sustain Energy Rev*. 2015;48:483–99.
81. Isenstadt A, Lutsey N. Developing hydrogen fueling infrastructure for fuel cell vehicles: A status update. 2017.
82. Staffell I, Scamman D, Velazquez Abad A, Balcombe P, Dodds PE, Ekins P, et al. The role of hydrogen and fuel cells in the global energy system. *Energy*

- Environ Sci. 2019;12(2):463–91.
83. Brandon NP, Kurban Z. Clean energy and the hydrogen economy. *Philos Trans R Soc A Math Phys Eng Sci.* 2017;375(2098):20160400.
 84. Cowley A. Johnson Matthey Pgm Market Report. 2019.
 85. Weller M, Overton T, Rourke J, Armstrong F. *Inorganic Chemistry.* OUP Oxford; 2014. 490 p.
 86. Antolini E. Palladium in fuel cell catalysis. *Energy Environ Sci.* 2009;2(9):915.
 87. Nørskov JK, T, Bligaard, A, Logadottir, Kitchin JR, et al. Trends in the exchange current for hydrogen evolution. *J Electrochem Soc.* 2019;152(2):23–6.
 88. Greeley J, Nørskov JK, Kibler LA, El-Aziz AM, Kolb DM. Hydrogen evolution over bimetallic systems: understanding the trends. *ChemPhysChem.* 2006;7(5):1032–5.
 89. Hammer B, Nørskov JK. Theoretical Surface Science and Catalysis - Calculations and Concepts. *Adv Catal.* 2000;45:71–129.
 90. Xin H, Vojvodic A, Voss J, Nørskov JK, Abild-Pedersen F. Effects of d-band shape on the surface reactivity of transition-metal alloys. *Phys Rev Lett.* 2014;89:115114.
 91. Cho Y-H, Cho Y-H, Lim JW, Park H-Y, Jung N, Ahn M, et al. Performance of membrane electrode assemblies using PdPt alloy as anode catalysts in polymer electrolyte membrane fuel cell. *Int J Hydrogen Energy.* 2012;37(7):5884–90.
 92. Hwang SJ, Yoo SJ, Shin J, Cho Y-H, Jang JH, Cho E, et al. Supported

- core@shell electrocatalysts for fuel cells: close encounter with reality. *Sci Rep*. 2013;3:1309.
93. Zhang G, Shao Z-G, Lu W, Xie F, Xiao H, Qin X, et al. Core–shell Pt modified Pd/C as an active and durable electrocatalyst for the oxygen reduction reaction in PEMFCs. *Appl Catal B Environ*. 2013;132–133:183–94.
94. Shao M, Liu P, Zhang J, Adzic R. Origin of enhanced activity in palladium alloy electrocatalysts for oxygen reduction reaction. *J Phys Chem B*. 2007;111(24):6772–5.
95. Wang JX, Inada H, Wu L, Zhu Y, Choi Y, Liu P, et al. Oxygen reduction on well-defined core-shell nanocatalysts: particle size, facet, and Pt shell thickness effects. *J Am Chem Soc*. 2009;131(47):17298–302.
96. Sasaki K, Naohara H, Cai Y, Choi YM, Liu P, Vukmirovic MB, et al. Core-Protected Platinum Monolayer Shell High-Stability Electrocatalysts for Fuel-Cell Cathodes. *Angew Chemie Int Ed*. 2010;49(46):8602–7.
97. Wang C-H, Hsu H-C, Wang K-C. Iridium-decorated Palladium–Platinum core–shell catalysts for oxygen reduction reaction in proton exchange membrane fuel cell. *J Colloid Interface Sci*. 2014;427:91–7.
98. Jervis R, Mansor N, Gibbs C, Murray CA, Tang CC, Brett DJL. Novel PdIr/C Catalysts for the Hydrogen Oxidation Reaction in Alkaline Media. *ECS Trans*. 2013;58(1):637–50.
99. Johnson Matthey. Price charts - PMM [Internet]. 2016 [cited 2016 Apr 29]. Available from: <http://www.platinum.matthey.com/prices/price-charts>

100. Sekol RC, Li X, Cohen P, Doubek G, Carmo M, Taylor AD. Silver palladium core–shell electrocatalyst supported on MWNTs for ORR in alkaline media. *Appl Catal B Environ.* 2013;138–139:285–93.
101. Singh RN. Palladium selenides as active methanol tolerant cathode materials for direct methanol fuel cell. *Int J Hydrogen Energy.* 2011;36(16):10006–12.
102. Bianchini C, Shen PK. Palladium-based electrocatalysts for alcohol oxidation in half cells and in direct alcohol fuel cells. *Chem Rev.* 2009;109(9):4183–206.
103. Liang ZX, Zhao TS, Xu JB, Zhu LD. Mechanism study of the ethanol oxidation reaction on palladium in alkaline media. *Electrochim Acta.* 2009;54(8):2203–8.
104. Cui G, Song S, Shen PK, Kowal A, Bianchini C. First-Principles Considerations on Catalytic Activity of Pd toward Ethanol Oxidation. *J Phys Chem C.* 2009;113(35):15639–42.
105. Xu JB, Zhao TS, Shen SY, Li YS. Stabilization of the palladium electrocatalyst with alloyed gold for ethanol oxidation. *Int J Hydrogen Energy.* 2010;35(13):6490–500.
106. Feng Y-Y, Liu Z-H, Xu Y, Wang P, Wang W-H, Kong D-S. Highly active PdAu alloy catalysts for ethanol electro-oxidation. *J Power Sources.* 2013;232:99–105.
107. Li G, Jiang L, Jiang Q, Wang S, Sun G. Preparation and characterization of Pd_xAg_y/C electrocatalysts for ethanol electrooxidation reaction in alkaline media. *Electrochim Acta.* 2011;56(22):7703–11.
108. Peng C, Hu Y, Liu M, Zheng Y. Hollow raspberry-like PdAg alloy nanospheres:

- High electrocatalytic activity for ethanol oxidation in alkaline media. *J Power Sources*. 2015;278:69–75.
109. Allen MJ, Tung VC, Kaner RB. Honeycomb carbon: a review of graphene. *Chem Rev*. 2010;110(1):132–45.
 110. Bhat SA, Rashid N, Rather MA, Pandit SA, Rather GM, Ingole PP, et al. PdAg Bimetallic Nanoalloy-Decorated Graphene: A Nanohybrid with Unprecedented Electrocatalytic, Catalytic, and Sensing Activities. *ACS Appl Mater Interfaces*. 2018;10(19):16376–89.
 111. Liu J, Zhou H, Wang Q, Zeng F, Kuang Y. Reduced graphene oxide supported palladium–silver bimetallic nanoparticles for ethanol electro-oxidation in alkaline media. *J Mater Sci*. 2011;47(5):2188–94.
 112. Kakaei K, Dorraji M. One-pot synthesis of Palladium Silver nanoparticles decorated reduced graphene oxide and their application for ethanol oxidation in alkaline media. *Electrochim Acta*. 2014;143:207–15.
 113. Uzunoglu A, Kose DA, Kose K, Gokmese E, Gokmese F. PdAg-decorated three-dimensional reduced graphene oxide-multi-walled carbon nanotube hierarchical nanostructures for high-performance hydrogen peroxide sensing. *MRS Commun*. 2018;8(3):680–6.
 114. Neto AO, da Silva SG, Buzzo GS, de Souza RFB, Assumpção MHMT, Spinacé E V., et al. Ethanol electrooxidation on PdIr/C electrocatalysts in alkaline media: electrochemical and fuel cell studies. *Ionics (Kiel)*. 2014;21(2):487–95.
 115. Casado-Rivera E, Volpe DJ, Alden L, Lind C, Downie C, Vázquez-Alvarez T, et

- al. Electrocatalytic activity of ordered intermetallic phases for fuel cell applications. *J Am Chem Soc.* 2004;126(12):4043–9.
116. Wang Y, Nguyen TS, Liu X, Wang X. Novel palladium–lead (Pd–Pb/C) bimetallic catalysts for electrooxidation of ethanol in alkaline media. *J Power Sources.* 2010;195(9):2619–22.
117. Larsen R, Ha S, Zakzeski J, Masel RI. Unusually active palladium-based catalysts for the electrooxidation of formic acid. *J Power Sources.* 2006;157(1):78–84.
118. Chen J, Li Y, Gao Z, Wang G, Tian J, Jiang C, et al. Ultrahigh activity of Pd decorated Ir/C catalyst for formic acid electro-oxidation. *Electrochem commun.* 2013 Dec;37:24–7.
119. Wang X, Tang Y, Gao Y, Lu T. Carbon-supported Pd–Ir catalyst as anodic catalyst in direct formic acid fuel cell. *J Power Sources.* 2008;175(2):784–8.
120. Chen J, Li Y, Liu S, Wang G, Tian J, Jiang C, et al. Remarkable activity of PdIr nanoparticles supported on the surface of carbon nanotubes pretreated via a sonochemical process for formic acid electro-oxidation. *Appl Surf Sci.* 2013;287:457–60.
121. Lu Y, Chen W. PdAg Alloy Nanowires: Facile One-Step Synthesis and High Electrocatalytic Activity for Formic Acid Oxidation. *ACS Catal.* 2012;2(1):84–90.
122. Feng Y-Y, Zhang G-R, Xu B-Q. Catalytic Pd-on-Au nanostructures with improved Pd activity for formic acid electro-oxidation. *RSC Adv.* 2013;3(6):1748.

123. Durst J, Siebel A, Simon C, Hasc F, Herranz J, Gasteiger HA. New insights into the electrochemical hydrogen oxidation and evolution reaction mechanism. *Energy Environ Sci.* 2014;7:2255–60.
124. Jervis R, Mansor N, Gibbs C, Murray CA, Tang CC, Shearing PR, et al. Hydrogen Oxidation on PdIr/C Catalysts in Alkaline Media. *J Electrochem Soc.* 2014;161(4):F458–63.
125. Yang T, Ma Y, Huang Q, Cao G, Wan S, Li N, et al. Palladium-iridium nanowires for enhancement of electro-catalytic activity towards oxygen reduction reaction. *Electrochem commun.* 2015;59:95–9.
126. You DJ, Jin S, Lee KH, Pak C, Choi KH, Chang H. Improvement of activity for oxygen reduction reaction by decoration of Ir on PdCu/C catalyst. *Catal Today.* 2012;185(1):138–42.
127. Song L, Liang Z, Vukmirovic MB, Adzic RR. Enhanced Oxygen Reduction Reaction Activity on Pt-Monolayer-Shell PdIr/Ni-Core Catalysts. *J Electrochem Soc.* 2018;165(15):J3288–94.
128. Bonarowska M, Karpiński Z, Kosydar R, Szumelda T, Drelinkiewicz A. Hydrodechlorination of CCl₄ over carbon-supported palladium–gold catalysts prepared by the reverse “water-in-oil” microemulsion method. *Comptes Rendus Chim.* 2015;18(10):1143–51.
129. Al-Odail FA, Anastasopoulos A, Hayden BE. The Hydrogen Evolution Reaction and Hydrogen Oxidation Reaction on thin film PdAu alloy surfaces. *Phys Chem Chem Phys.* 2010;12(37):11398–406.

130. Simonov AN, Plyusnin PE, Shubin Y V., Kvon RI, Korenev S V., Parmon VN. Hydrogen electrooxidation over palladium–gold alloy: Effect of pretreatment in ethylene on catalytic activity and CO tolerance. *Electrochim Acta*. 2012;76:344–53.
131. Simonov AN, Pyrjaev PA, Simonov PA, Moroz BL, Cherepanova S V., Zyuzin DA, et al. Enhanced catalytic activity for hydrogen electrooxidation and CO tolerance of carbon-supported non-stoichiometric palladium carbides. *J Mol Catal A Chem*. 2012;353–354:204–14.
132. Meku E, Du C, Sun Y, Du L, Wang Y, Kong F, et al. Composition optimization of ternary palladium–iridium–iron alloy catalysts for oxygen reduction reaction in acid medium. *RSC Adv*. 2016;6(27):22754–63.
133. Ham HC, Manogaran D, Lee KH, Kwon K, Jin S, You DJ, et al. Communication: Enhanced oxygen reduction reaction and its underlying mechanism in Pd-Ir-Co trimetallic alloys. *J Chem Phys*. 2013;139(20):201104.
134. Schmidt TJ, Jusys Z, Gasteiger HA, Behm RJ, Endruschat U, Boennemann H. On the CO tolerance of novel colloidal PdAu/carbon electrocatalysts. *J Electroanal Chem*. 2001;501(1):132–40.
135. Hammer B, Nørskov JK. Why gold is the noblest of all metals. *Nature*. 1995;376:238.
136. Chen M, Kumar D, Yi C-W, Goodman DW. The promotional effect of gold in catalysis by palladium-gold. *Science*. 2005;310(5746):291–3.
137. Hinds G, Brightman E. In situ mapping of electrode potential in a PEM fuel cell.

Electrochem commun. 2012;17:26–9.

138. Hutchings GJ, Kiely CJ. Strategies for the synthesis of supported gold palladium nanoparticles with controlled morphology and composition. *Acc Chem Res.* 2013;46(8):1759–72.
139. Compton RG, Banks CE. *Understanding Voltammetry.* World Scientific; 2007. 107 p.
140. Zittel HE, Miller FJ. A Glassy-Carbon Electrode for Voltammetry. *Anal Chem.* 1965;37(2):200–3.
141. Łukaszewski M, Soszko M, Czerwiński A. Electrochemical Methods of Real Surface Area Determination of Noble Metal Electrodes - an Overview. *Int J Electrochem Sci.* 2016;11:4442–69.
142. Nagai T, Jahn C, Jia H. Improved Accelerated Stress Tests for ORR Catalysts Using a Rotating Disk Electrode. *J Electrochem Soc.* 2019 Apr 2;166(7):F3111–5.
143. Vippola M, Valkonen M, Sarlin E, Honkanen M, Huttunen H. Insight to Nanoparticle Size Analysis—Novel and Convenient Image Analysis Method Versus Conventional Techniques. *Nanoscale Res Lett.* 2016 Dec 1;11(1):169.
144. Raichle M. Chapter 18 The origins of functional brain imaging in humans. In: *Handbook of Clinical Neurology.* Elsevier; 2009. p. 257–68.
145. Willmott P. Chapter 7 Imaging Techniques. In: *An Introduction to Synchrotron Radiation.* Chichester, UK: John Wiley & Sons, Ltd; 2011. p. 303–37.

146. El-Kharouf A. UNDERSTANDING GDL PROPERTIES AND PERFORMANCE IN POLYMER ELECTROLYTE FUEL CELLS. University of Birmingham; 2014.
147. El-kharouf A, Mason TJ, Brett DJL, Pollet BG. Ex-situ characterisation of gas diffusion layers for proton exchange membrane fuel cells. J Power Sources. 2012;218:393–404.
148. Squadrito G. Fuel Cells and Hydrogen: From Fundamentals to Applied Research - Chapter 6 Preparation of MEA. Elsevier; 2018. 126 p.
149. Meyer Q, Mansor N, Iacoviello F, Cullen PL, Jervis R, Finegan D, et al. Investigation of Hot Pressed Polymer Electrolyte Fuel Cell Assemblies via X-ray Computed Tomography. Electrochim Acta. 2017;242:125–36.
150. Bloom I, Basco JK, Walker LK, Malkow T, DeMarco G, Saturnio A, et al. Fuel Cell Testing Protocols: An International Perspective. 2013.
151. S. S. Penner. Assessment of research needs for advanced fuel cells by the DOE advanced fuel cell working group. 1985.
152. Ticianelli EA, Derouin CR, Redondo A, Srinivasan S. Methods to Advance Technology of Proton Exchange Membrane Fuel Cells. J Electrochem Soc. 1988;135(9):2209.
153. Murphy OJ, Hitchens GD, Manko DJ. High power density proton-exchange membrane fuel cells. Journal of Power Sources. 1994;47:353–68.
154. Wilson MS, Gottesfeld S. Thin-film catalyst layers for fuel cell electrodes polymer electrolyte. J Appl Electrochem. 1992;22:1–7.

155. Miller WG, Eckfeldt JH, Passarelli J, Rosner W, Young IS. Harmonization of test results: what are the challenges; how can we make it better? Clin Chem. 2014;60(7):923–7.
156. Millington B, Du S, Pollet BG. The effect of materials on proton exchange membrane fuel cell electrode performance. J Power Sources. 2011;196(21):9013–7.
157. Du S, Millington B, Pollet BG. The effect of Nafion ionomer loading coated on gas diffusion electrodes with in-situ grown Pt nanowires and their durability in proton exchange membrane fuel cells. Int J Hydrogen Energy. 2011;36(7):4386–93.
158. Meyer Q, Mansor N, Iacoviello F, Cullen PL, Jervis R, Finegan D, et al. Investigation of Hot Pressed Polymer Electrolyte Fuel Cell Assemblies via X-ray Computed Tomography. Electrochim Acta. 2017;242:125–36.
159. Shearing PR, Eastwood DS, Bradley RS, Gelb J, Cooper SJ, Tariq F, et al. Exploring electrochemical devices using X-ray microscopy: 3D micro-structure of batteries and fuel cells. Microscopy and Analysis. 2013;
160. White RT, Wu A, Najm M, Orfino FP, Dutta M, Kjeang E. 4D in situ visualization of electrode morphology changes during accelerated degradation in fuel cells by X-ray computed tomography. J Power Sources. 2017;350:94.
161. Yu W-Y, Zhang L, Mullen GM, Evans EJ, Henkelman G, Mullins CB. Effect of annealing in oxygen on alloy structures of Pd–Au bimetallic model catalysts. Phys Chem Chem Phys. 2015;17(32):20588–96.

162. Jirkovský JS, Halasa M, Schiffrin DJ. Kinetics of electrocatalytic reduction of oxygen and hydrogen peroxide on dispersed gold nanoparticles. *Phys Chem Chem Phys*. 2010;12(28):8042.
163. Pizzutilo E, Geiger S, Freakley SJ, Mingers A, Cherevko S, Hutchings GJ, et al. Palladium electrodisolution from model surfaces and nanoparticles. *Electrochim Acta*. 2017;229:467–77.
164. Zhang D, Jin C, Tian H, Xiong Y, Zhang H, Qiao P, et al. An In situ TEM study of the surface oxidation of palladium nanocrystals assisted by electron irradiation. *Nanoscale*. 2017;9(19):6327–33.
165. Jiang B, Guo Y, Kim J, Whitten AE, Wood K, Kani K, et al. Mesoporous Metallic Iridium Nanosheets. *J Am Chem Soc*. 2018;140(39):12434–41.
166. Dilshad N, Ansari MS, Beamson G, Schiffrin DJ. Amines as dual function ligands in the two-phase synthesis of stable $AuCu(1-x)$ binary nanoalloys. *J Mater Chem*. 2012;22(21):10514–24.
167. Daio T, Staykov A, Guo L, Liu J, Tanaka M, Matthew Lyth S, et al. Lattice Strain Mapping of Platinum Nanoparticles on Carbon and SnO_2 Supports. *Sci Rep*. 2015;5(1):13126.
168. Jovanović P, Hodnik N, Ruiz-Zepeda F, Arčon I, Jozinović B, Zorko M, et al. Electrochemical Dissolution of Iridium and Iridium Oxide Particles in Acidic Media: Transmission Electron Microscopy, Electrochemical Flow Cell Coupled to Inductively Coupled Plasma Mass Spectrometry, and X-ray Absorption Spectroscopy Study. *J Am Chem Soc*. 2017;139(36):12837–46.

169. Feng Y-Y, Liu Z-H, Kong W-Q, Yin Q-Y, Du L-X. Promotion of palladium catalysis by silver for ethanol electro-oxidation in alkaline electrolyte. *Int J Hydrogen Energy*. 2014;39(6):2497–504.
170. W. B. Pearson. *Crystal Chemistry and Physics of Metals and Alloys*. Wiley; 1972.
171. Kuttiyiel KA, Sasaki K, Su D, Vukmirovic MB, Marinkovic NS, Adzic RR. Pt monolayer on Au-stabilized PdNi core–shell nanoparticles for oxygen reduction reaction. *Electrochim Acta*. 2013;110:267–72.
172. Alia SM, Hurst KE, Kocha SS, Pivovar BS. Mercury Underpotential Deposition to Determine Iridium and Iridium Oxide Electrochemical Surface Areas. *J Electrochem Soc*. 2016;163(11):3051–6.
173. Jervis R. *Development of Novel Alloy Electrocatalysts for the Hydrogen Oxidation Reaction in Alkaline Media and their Application to Low Temperature Fuel Cells*. University College London; 2015.
174. Geiger S, Kasian O, Shrestha BR, Mingers AM, Mayrhofer KJJ, Cherevko S. Activity and Stability of Electrochemically and Thermally Treated Iridium for the Oxygen Evolution Reaction. *J Electrochem Soc*. 2016;163(11):F3132–8.
175. LaPrade M, Allard KD, Lynch JF, Flanagan TB. Absorption of hydrogen by iridium/palladium substitutional alloys. *J Chem Soc, Faraday Trans 1*. 1974;70:1615–30.
176. Zlotea C, Morfin F, Nguyen TS, Nguyen NT, Nelayah J, Ricolleau C, et al. Nanoalloying bulk-immiscible iridium and palladium inhibits hydride formation and promotes catalytic performances. *Nanoscale*. 2014;6(17):9955–9.

177. Cherevko S, Reier T, Zeradjanin AR, Pawolek Z, Strasser P, Mayrhofer KJJ. Stability of nanostructured iridium oxide electrocatalysts during oxygen evolution reaction in acidic environment. *Electrochem commun.* 2014;48:81–5.
178. Pizzutilo E, Freakley SJ, Geiger S, Baldizzone C, Mingers A, Hutchings GJ, et al. Addressing stability challenges of using bimetallic electrocatalysts: the case of gold–palladium nanoalloys. *Catal Sci Technol.* 2017;7(9):1848–56.
179. Jirkovský JS, Panas I, Ahlberg E, Halasa M, Romani S, Schiffrin DJ. Single Atom Hot-Spots at Au–Pd Nanoalloys for Electrocatalytic H₂ O₂ Production. *J Am Chem Soc.* 2011;133(48):19432–41.
180. Bertuccioli L, Chan A, Hart D, Lehner F, Madden B, Standen E. Development of Water Electrolysis in the European Union Final Report Fuel cells and hydrogen. 2014.
181. Babic U, Suermann M, Büchi FN, Gubler L, Schmidt TJ. Critical Review—Identifying Critical Gaps for Polymer Electrolyte Water Electrolysis Development. *J Electrochem Soc.* 2017;164(4):F387–99.
182. Millet P, Grigoriev S. Chapter 2 - Water Electrolysis Technologies. In: *Renewable Hydrogen Technologies*. Elsevier; 2013. p. 19–41.
183. Vesborg PCK, Seger B, Chorkendorff I. Recent development in hydrogen evolution reaction catalysts and their practical implementation. *J Phys Chem Lett.* 2015;6(6):951–7.
184. Schmidt O, Gambhir A, Staffell I, Hawkes A, Nelson J, Few S. Future cost and performance of water electrolysis: An expert elicitation study. *Int J Hydrogen*

Energy. 2017;42(52):30470–92.

185. Coutanceau C, Baranton S, Audichon T. Chapter 3 - Hydrogen Production From Water Electrolysis. In: Hydrogen Electrochemical Production. Academic Press; 2018. p. 17–62.
186. Rashid M, Al Mesfer MK, Naseem H, Danish M. Hydrogen Production by Water Electrolysis: A Review of Alkaline Water Electrolysis, PEM Water Electrolysis and High Temperature Water Electrolysis. *Int J Eng Adv Technol*. 2015;4(3):2329–42.
187. Ulleberg Ø. Modeling of advanced alkaline electrolyzers: a system simulation approach. *Int J Hydrogen Energy*. 2003;28(1):21–33.
188. Carmo M, Fritz DL, Mergel J, Stolten D. A comprehensive review on PEM water electrolysis. *Int J Hydrogen Energy*. 2013;38(12):4901–34.
189. Harrison KW, Remick R, Martin GD, Hoskin A. Hydrogen Production: Fundamentals and Case Study Summaries e Preprint. In: 18th World Hydrogen Energy Conference. Essen, Germany; 2010.
190. Zhang X, Chan SH, Ho HK, Tan S-C, Li M, Li G, et al. Towards a smart energy network: The roles of fuel/electrolysis cells and technological perspectives. *Int J Hydrogen Energy*. 2015;40(21):6866–919.
191. Marshall A, Børresen B, Hagen G, Tsyppkin M, Tunold R. Hydrogen production by advanced proton exchange membrane (PEM) water electrolyzers—Reduced energy consumption by improved electrocatalysis. *Energy*. 2007;32(4):431–6.

192. Song S, Zhang H, Liu B, Zhao P, Zhang Y, Yi B. An Improved Catalyst-Coated Membrane Structure for PEM Water Electrolyzer. *Electrochem Solid-State Lett.* 2007;10(8):B122.
193. Andolfatto F, Durand R, Michas A, Millet P, Stevens P. Solid polymer electrolyte water electrolysis: electrocatalysis and long-term stability. *Int J Hydrogen Energy.* 1994;19(5):421–7.
194. Reier T, Nong HN, Teschner D, Schlögl R, Strasser P. Electrocatalytic Oxygen Evolution Reaction in Acidic Environments - Reaction Mechanisms and Catalysts. *Adv Energy Mater.* 2017;7(1):1601275.
195. Bockris JO. Kinetics of Activation Controlled Consecutive Electrochemical Reactions: Anodic Evolution of Oxygen. *J Chem Phys.* 1956;24(4):817–27.
196. Shi Y, Zhang B. Recent advances in transition metal phosphide nanomaterials: synthesis and applications in hydrogen evolution reaction. *Chem Soc Rev.* 2016;45(6):1529–41.
197. Shinagawa T, Garcia-Esparza AT, Takanabe K. Insight on Tafel slopes from a microkinetic analysis of aqueous electrocatalysis for energy conversion. *Sci Rep.* 2015;5(1):13801.
198. Zhang Y, Gao L, Hensen EJM, Hofmann JP. Evaluating the Stability of Co₂P Electrocatalysts in the Hydrogen Evolution Reaction for Both Acidic and Alkaline Electrolytes. *ACS Energy Lett.* 2018;3(6):1360.
199. Parsons R. The rate of electrolytic hydrogen evolution and the heat of adsorption of hydrogen. *Trans Faraday Soc.* 1958;54(0):1053.

200. Berit Hinnemann, Poul Georg Moses, Jacob Bonde, Kristina P. Jørgensen, Jane H. Nielsen, Sebastian Horch, et al. Biomimetic Hydrogen Evolution: MoS₂ Nanoparticles as Catalyst for Hydrogen Evolution. 2005;
201. Chen W-F, Wang C-H, Sasaki K, Marinkovic N, Xu W, Muckerman JT, et al. Highly active and durable nanostructured molybdenum carbide electrocatalysts for hydrogen production. *Energy Environ Sci.* 2013;6(3):943.
202. Liu P, Rodriguez JA. Catalysts for Hydrogen Evolution from the [NiFe] Hydrogenase to the Ni₂P(001) Surface: The Importance of Ensemble Effect. *J Am Chem Soc.* 2005;127(42):14871–8.
203. Kucernak ARJ, Sundaram VNN. Nickel phosphide: the effect of phosphorus content on hydrogen evolution activity and corrosion resistance in acidic medium. *J Mater Chem A.* 2014;2(41):17435–45.
204. Popczun EJ, McKone JR, Read CG, Biacchi AJ, Wiltrout AM, Lewis NS, et al. Nanostructured Nickel Phosphide as an Electrocatalyst for the Hydrogen Evolution Reaction. *J Am Chem Soc.* 2013;135(25):9267–70.
205. McEnaney JM, Chance Crompton J, Callejas JF, Popczun EJ, Read CG, Lewis NS, et al. Electrocatalytic hydrogen evolution using amorphous tungsten phosphide nanoparticles. *Chem Commun.* 2014;50(75):11026.
206. McEnaney JM, Crompton JC, Callejas JF, Popczun EJ, Biacchi AJ, Lewis NS, et al. Amorphous Molybdenum Phosphide Nanoparticles for Electrocatalytic Hydrogen Evolution. *Chem Mater.* 2014;26(16):4826–31.
207. Saadi FH, Carim AI, Verlage E, Hemminger JC, Lewis NS, Soriaga MP. CoP as

- an Acid-Stable Active Electrocatalyst for the Hydrogen-Evolution Reaction: Electrochemical Synthesis, Interfacial Characterization and Performance Evaluation. *J Phys Chem C*. 2014;118(50):29294–300.
208. Callejas JF, Read CG, Popczun EJ, McEnaney JM, Schaak RE. Nanostructured Co₂P Electrocatalyst for the Hydrogen Evolution Reaction and Direct Comparison with Morphologically Equivalent CoP. *Chem Mater*. 2015;27(10):3769–74.
 209. Carencu S, Liu Z, Salmeron M. The Birth of Nickel Phosphide Catalysts: Monitoring Phosphorus Insertion into Nickel. *ChemCatChem*. 2017;9(12):2318–23.
 210. Zhou W, Greer HF. What Can Electron Microscopy Tell Us Beyond Crystal Structures? *Eur J Inorg Chem*. 2016;2016(7):941–50.
 211. Escalera-López D, Niu Y, Yin J, Cooke K, Rees N V., Palmer RE. Enhancement of the Hydrogen Evolution Reaction from Ni-MoS₂ Hybrid Nanoclusters. *ACS Catal*. 2016 Sep 2;6(9):6008–17.
 212. Seo B, Baek DS, Sa YJ, Joo SH. Shape effects of nickel phosphide nanocrystals on hydrogen evolution reaction. *CrystEngComm*. 2016 Aug 10;18(32):6083–9.
 213. Pan Y, Liu Y, Zhao J, Yang K, Liang J, Liu D, et al. Monodispersed nickel phosphide nanocrystals with different phases: synthesis, characterization and electrocatalytic properties for hydrogen evolution. *J Mater Chem A*. 2015;3(4):1656–65.
 214. Hong W, Lv C, Sun S, Chen G. Fabrication and study of the synergistic effect of

- Janus Ni₂P/Ni₅P₄ embedded in N-doped carbon as efficient electrocatalysts for hydrogen evolution reaction. *Catal Sci Technol*. 2020 Feb 21;10(4):1023–9.
215. Mabayoje O, Dunning SG, Kawashima K, Wygant BR, Ciufo RA, Humphrey SM, et al. Hydrogen Evolution by Ni₂P Catalysts Derived from Phosphine MOFs. *ACS Appl Energy Mater*. 2020 Jan 27;3(1):176–83.
 216. Bernt M, Hartig-Weiß A, Tovini MF, El-Sayed HA, Schramm C, Schröter J, et al. Current Challenges in Catalyst Development for PEM Water Electrolyzers. *Chemie Ing Tech*. 2020 Jan 1;92(1–2):31–9.
 217. Kristinsdóttir L, Skúlason E. A systematic DFT study of hydrogen diffusion on transition metal surfaces. *Surf Sci*. 2012 Sep 1;606(17–18):1400–4.
 218. Kucernak ARJ, Fahy KF, Sundaram VNN. Facile synthesis of palladium phosphide electrocatalysts and their activity for the hydrogen oxidation, hydrogen evolutions, oxygen reduction and formic acid oxidation reactions. *Catal Today*. 2016;262:48–56.
 219. Seh ZW, Kibsgaard J, Dickens CF, Chorkendorff I, Nørskov JK, Jaramillo TF. Combining theory and experiment in electrocatalysis: Insights into materials design. *Citation*. 2017;355(6321).